Committee

Prof. Véronique Dehant (Supervisor)	UCLouvain & ROB
Dr. Santiago Andrés Triana (Supervisor)	ROB
Prof. Qiuzhen Yin (President)	UCLouvain
Prof. Hugues Goosse (Secretary)	UCLouvain
Dr. Jérõme André Roland Noir	ETH Zürich
Prof. Tim Van Hoolst	KU Leuven & ROB

Abstract

Precise measurements of the Earth's rotation have led to estimates of energy dissipation near the core-mantle boundary, revealing a mismatch between the observed and theoretical values. This discrepancy suggests that studying the Earth's rotational motion can offer insights into its internal physical processes. Turbulence and surface roughness in the boundary layer have been proposed as potential mechanisms to explain the discrepancy. However, there is still room for improvement in quantifying these effects due to the lack of appropriate experimental or numerical results. To address this, we employ a local box model to numerically investigate the boundary layer. This approach, compared to a global spherical model, allows for the exploration of more extreme parameter regimes, providing insights into the influence of turbulence. Additionally, surface roughness is modeled by introducing undulations on the boundary to assess its impact on viscous dissipation.

In this thesis, I present numerical simulations of oscillatory Ekman layers, which are used to approximate the boundary layer, in both the laminar and the turbulent regimes, with Reynolds numbers Re (based on boundary layer thickness) up to 700. The total viscous dissipation in the boundary layer is calculated by summing local contributions. The result shows a transition to turbulence at about $Re = 290$ and an increase in the dissipation by a factor of 1.86 at $Re = 500$. The increase is equivalent to an effective viscosity increased by a factor of 3.46. This effect is too small to explain the dissipation inferred from the nutation observation, thus suggesting that other dissipation mechanisms must be at play. In addition, I derived a turbulence model and then calibrated it using our numerical result. The turbulence model can be extended to more extreme parameters, such as those corresponding to the lunar core. The result is consistent with the values inferred from the analysis of lunar laser ranging data. The effect of turbulent torque on the solution of precession-driven flow is also discussed.

To study the effect of surface roughness, we implement a sinusoidal profile on the boundary. Given that the boundary oscillates in time in our formulation, we use a deforming mesh to capture the movement of the surface roughness. This method allows our numerical model to reproduce the steady streaming patterns observed in certain oscillatory flows over wavy surfaces. When applied to the oscillatory Ekman layer, the introduction of roughness generates pressure drag on the surface, with the drag amplitude increasing as the roughness height grows.

Acknowledgment

Writing this thesis has been a journey of self-reflection, not only on the academic knowledge related to the topic but also on the person I aspire to become. While the academic insights are documented in this work, the question of who I want to become remains open. I do know, however, that I am deeply grateful to everyone who has crossed my path in any capacity, as their presence has shaped this journey.

First and foremost, I would like to express my gratitude to Véronique. Without her support in the proposal phase, I would not have embarked on this PhD journey in Belgium. It has been a privilege to be part of the GRACEFUL project, which has provided me with the opportunity to connect with a diverse group of individuals and learn so much from them. I am particularly grateful to Andrés for always being available for discussions. His suggestion to explore turbulence shaped my research, and it was through our conversations that the issue with topography implementation was identified. Thanks Jérémy for being more than just a yellow duck; problems seemed to resolve themselves after talking them through with you. I would also like to thank everyone I met at the observatory for creating so many wonderful memories with me, from the BBQ event and the table tennis tournament to the writing group, the laser-tag game, and the azaleas.

My gratitude goes to Benjamin Favier for providing an example code, and Philipp Schlatter for the insightful discussions during the early stages of my work with Nek5000. Special thanks to Qiuzhen for chairing my defenses, Hugues for his invaluable advice on thesis writing, Tim for his thoughtful comments and suggestions on the thesis, and Jérõme for the fruitful discussions on topics related to precession-driven flow and the oscillatory Ekman layer.

A heartfelt thanks to Solange for providing me with a place to stay during the pandemic, which became more than just shelter, but a home filled with warmth and a beautiful garden that became my favorite retreat. Thanks to my friends at Forza Uccle for the wonderful times spent playing volleyball together. I am grateful for the unconditional support from my family. Finally, my deepest gratitude goes to Chih-Chin for her unwavering companionship and support throughout this journey.

Contents

List of Figures

List of Tables

Chapter 1

Introduction

1.1 Precession and Nutation of the Earth

Earth's rotation axis is not fixed in space. The Greek astronomer Hipparchus (c. 190 - c. 120 BC) is credited with discovering the secular variation of the axis and measuring its rate of change. He observed that the position of certain fixed stars was not truly fixed but slowly varied over time (Toomer, 1996). According to a review by Ekman (1993), Hipparchus noted that the zodiacal longitude of the star Spica was 2° ahead of its position compared to observations made 148 years before. Together with other observations, he accounted the observational uncertainty and suggested a rate of variation of at least 1° per 100 years, implying a period of $\leq 36,500$ years. By the 17th century, astronomical observations had determined the precession rate to be 50 arcseconds per year, corresponding to a period of $25,920$ years. This value, documented in Isaac Newton's *Principia* (first published in 1687), is remarkably close to the modern estimation of $25,770$ years.

In 1747, James Bradley reported a "new Phenomenon, viz. an annual change of declination in some of the fixed Stars" (Bradley, 1747). He discovered that for some stars nearly opposite in right ascension, their declination changed by nearly the same amount but in opposite directions, a phenomenon that could not be explained by precession alone. This observation led to the discovery of the Earth's rotation axis moving around its mean position, a motion now known as the principal nutation or Bradley nutation, with a period of about 18.6 years.

Figure 1.1 illustrates the variations in Earth's rotation axis. The circular cone with an angle of 23.5° represents the precessional path, while the small oscillation superimposed on it represents the principal nutation. The number of cycles of the oscillation is not to scale relative to the precession cycle. In reality, for one cycle of precession, there are about 10^3 cycles of nutation, equating to approximately three oscillations within one degree of arc on the precessional path.

The physical origin of the precession and the nutation is mainly related to the gravitational interaction between the Earth and the two celestial objects: the Sun and the Moon. Given that the Earth can be approximated as a spheroid

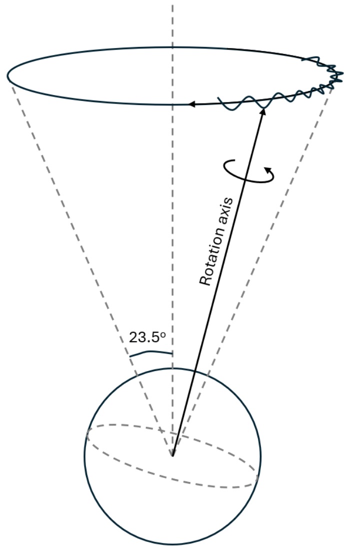

Figure 1.1: Precession and nutation of the Earth. The circular cone with an angle of 23.5° represents the precessional path, while the small oscillation superimposed on it represents the principal nutation. Figure adapted from Dehant and Mathews (2015).

bulging at the equator (oblate), this bulge acts like a handle that the Sun and Moon use to exert torques on the Earth. The torques behave as if attempting to align the equatorial bulge with the ecliptic plane. Note that although the orbital plane of the Moon is not aligned with the ecliptic plane, the small inclination angle, of about five degrees, does not affect the aforementioned description. These torques change over time, depending on the positions of the Sun and the Moon. For example, the torque exerted by the Sun reaches a maximum at the solstices and becomes zero at the equinoxes. Despite the time variability, the cumulative effect results in a net torque that causes the Earth's rotation axis to precess in the retrograde direction (i.e. the direction opposite to the primary rotation; see Figure 1.2). On the other hand, the time-dependent components of the torques are responsible for the periodic motions of the axis, known as the nutations. The principal nutation is related to the precession of the pole of the lunar orbit, which has a period of 18.6 years. Other nutations have periods of approximately one-year, half-year, half-month, etc.

The torque-induced precession can be illustrated with a spinning top, which exhibits similarities to the Earth's precession. Consider an axially symmetric spinning top placed on the Earth's surface, with gravity acting downward. If the rotation axis of the top is not parallel to the gravity, a torque will be exerted on it. This torque behaves as if it is attempting to drag the top toward the surface. Due to the top's spinning motion, the axis ultimately precesses in the prograde direction (i.e. in the same direction as the primary rotation). In Figure 1.2, the spinning top can be represented by the rotating spheroid,

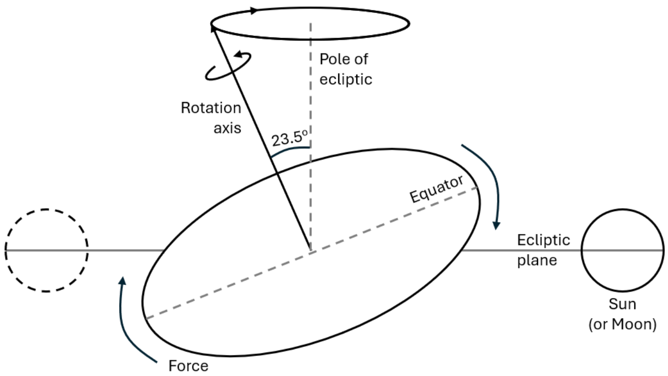

Figure 1.2: Torque causing the Earth's precession. The gravitational attraction from the Sun (or the Moon) on the equatorial bulge results in a torque which behaves as if attempting to align the equatorial bulge with the ecliptic plane. Although the orbital plane of the Moon is not aligned with the ecliptic plane, the small inclination angle, of about five degrees, does not affect the aforementioned description. Figure adapted from Stacey and Davis (2008).

with the distinction that the net torque exerted on the top is in the opposite direction, causing the precession to be in the opposite direction as well. This example demonstrates that the direction of precession depends on the direction of the exerted torque.

Let's consider a hypothetical scenario where the Earth bulges at the poles and the rotation axis aligns with this elongated axis. In this case, the cumulative effect of the torques from the Sun (or the Moon) would act as if attempting to pull the axis toward the pole of the ecliptic. Consequently, the precession would occur in the prograde direction, opposite to the direction when the Earth has an equatorial bulge. That means, by observing the direction of precession, we can infer the location of the bulges. A similar argument is found in Newton's *Principia*: "if ... the motion (of the nodes) be in antecedentia, there is a redundance of the matter near the equator; but if in consequentia, a deficiency" (Newton & Chittenden, 1850)[1]. Since the Earth's rotation axis precesses in the retrograde direction, that is the equinoxes (the nodes) go backwards (in antecedentia)[2], therefore the Earth bulges at the equator. This demonstrates how we can learn about Earth's interior structure by measuring variations in the rotation axis.

Very long baseline interferometry (VLBI) is a technique that has been used for more than 40 years to determine the Earth's orientation, including the rotation axis. The principle is to measure the differences in arrival time at various Earth-based antennas of signals from radio sources. The measurement allows the determination of the positions of both the radio sources and the

[1]This is the English edition translated by Andrew Motte, with a life of the author by N. W. Chittenden.

[2]antĕcēdo means to proceed or to go before in Latin.

antennas. The chosen radio sources are so distant that their positions can be considered fixed in space, providing a stable reference for defining an inertial frame. By defining an inertial frame based on the positions of the radio sources, the relative positions of the antennas, which are located on Earth, then infer the orientation of the Earth in the inertial frame.

As an example, Herring et al. (1986) analyzed data from the VLBI observing sessions carried out between 1980 and 1984 to determine the Earth's nutations. By comparing their result to the prevailing theoretical model for nutations, they estimated corrections to several nutations with periods ≤ 1 year. The largest correction is related to the retrograde annual nutation, which is one of the many tidal forcing components, and the correction was interpreted as a deficiency in the core-mantle coupling mechanism as included in the model (see below).

1.2 Core-mantle coupling

Nutation observation, specifically the retrograde annual nutation, provides a way to estimate the core-mantle coupling. The reason that the retrograde annual nutation is sensitive to the core-mantle coupling is related to the existence of a resonance at the free core nutation (FCN) of the Earth and the proximity of the retrograde annual frequency to the FCN frequency. In theory, FCN is a rotational normal mode that already appears in a simplified two-layered planet, where the inner layer consisting of inviscid fluid (core) is covered by a rigid ellipsoidal mantle (Sasao et al., 1980; Dehant & Mathews, 2015; Rekier et al., 2020). The pressure coupling due to pressure acting on the ellipsoidal core-mantle boundary (CMB) couples the rotations of the mantle and the core, thus giving rise to FCN when one excites an angle between the rotation axis of the core and that of the mantle. The two-layered planet should be understood as a minimal model that includes the necessary ingredients for FCN to exist and as a demonstration of the importance of the core-mantle coupling. Pressure coupling mainly controls the period of FCN, while dissipative mechanisms control the damping.

Based on the prevailing theory in 1980's by Wahr (1981), which was adopted by the International Astronomical Union, the period of the Earth's FCN is about 460 days in the retrograde direction. The period is close to that of the retrograde annual nutation (365.3 days) so the forced nutation is amplified due to a resonance effect. The amplification depends on how close the forced nutation period is to the period of the FCN thus on the coupling at the CMB. According to Herring et al. (1986), the study based on the nutation observation suggested a period of about 430 days for the Earth's FCN. The discrepancy was then interpreted as a deviation from the hydrostatic equilibrium figure, with the peak-to-peak deviation of about 490 m (Gwinn et al., 1986).

Gwinn et al. (1986) also estimated an upper bound for the fluid core viscosity, based on the observation of the out-of-phase part of the retrograde annual mutation. The observation was interpreted as an indication of a highly conductive lowermost mantle and a strong magnetic field in the core (Buffett, 1992; Buffett et al., 2002). This interpretation was motivated by experiments on mineral physics which implied the possibility of material with high conductivity at CMB conditions (e.g. Knittle & Jeanloz, 1989). Later, attempts to combine viscous and electromagnetic effects were carried out by Mathews and Guo (2005) and Deleplace and Cardin (2006) with the goal of estimating the viscosity and the magnetic field strength. Issues related to the magnetic field, such as the contribution from the short wavelength components were studied by Buffett and Christensen (2007) and the field morphology by Koot and Dumberry (2013).

Nevertheless, according to the analysis by Koot et al. (2010), the upper bound for the kinematic viscosity ν of the fluid is at the order of $10^{-2}\,\mathrm{m}^2\,\mathrm{s}^{-1}$. In comparison, theoretical calculations suggest a much lower value for the liquid iron at the core condition: $\nu = 10^{-6}\,\mathrm{m}^2\,\mathrm{s}^{-1}$, based on the density functional theory (Pozzo et al., 2013) or an ab initio molecular dynamics simulation (Ichikawa & Tsuchiya, 2015). The discrepancy has long been attributed to turbulence effects, but a quantitative study is missing. Therefore, one of the purposes of this thesis is to quantify the effect of turbulence and check if it can explain the discrepancy.

1.3 Boundary layer turbulence

Based on nutation observations, Gwinn et al. (1986) showed that the estimated upper bound of the viscosity is a few orders larger than the theoretical value. Similar results were obtained in the following studies, where the excess of viscosity was argued as the evidence for turbulence in the boundary layer (Deleplace & Cardin, 2006). However, the dimensional analysis made by Buffett and Christensen (2007) and Koot et al. (2010) does not support this argument: the corresponding eddy size is much larger than the boundary layer thickness. It was proposed by Triana et al. (2021) that the boundary layer generated by precession might be turbulent and that could explain (part of) the eddy viscosity. Buffett (2021) used a local Cartesian model to study the turbulence condition for the boundary layer at CMB and found a hint of turbulence. This motivates our exploration of the boundary layer of precession-driven flow in the turbulent regime, hoping to gain some insight into the core-mantle coupling mechanisms.

1.4 Roughness on core-mantle boundary

The Earth's CMB might have rich topography on various length scales. At the largest length scale, the CMB is oblate along the rotation axis, as the centrifugal force pulls materials toward the equator. The dynamic ellipticity of the Earth's core $e_f = (I_{3,f} - I_{1,f})/I_{1,f}$, where $I_{1,f}$ is the equatorial moment of inertia of the core and $I_{3,f}$ is its polar moment of inertia, has been determined from nutation observations (e.g. Gwinn et al., 1986; Mathews et al., 2002; Koot et al., 2010). Although there is variation in the estimated dynamic ellipticity depending on the model, they all show a deviation from the hydrostatic value by about 6% or less. Throughout this thesis, we adopt the value $e_f = 2.6 \times 10^{-3}$. From a seismological viewpoint, there are studies suggesting undulations with horizontal scales from tens to hundreds of kilometers or even more (see the

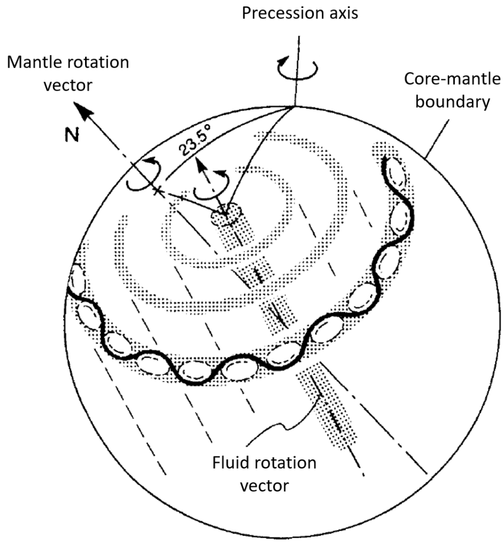

Figure 1.3: Sketch for the precession-driven flow observed in the experiment simulating the flow in the Earth's core due to precession. Figure adapted from Vanyo et al. (1995).

review of Koelemeijer, 2021). In terms of geodynamics, there are numerical simulations showing that mantle convection could result in CMB topography (e.g. Forte & Peltier, 1989, 1991; Soldati et al., 2012; Deschamps et al., 2018).

To study the small-scale roughness, Narteau et al. (2001) used a simple model to simulate the physical-chemical interaction on CMB and their model shows roughness developed during the simulation. The effect of roughness on the dissipation related to nutation-driven flow has been discussed by Le Mouël et al. (2006) and Buffett and Christensen (2007). The relation to gravity and magnetic field was discussed by Mandea et al. (2015) and Dumberry and Mandea (2022).

1.5 Precession-driven flow

Precession drives fluid motion within the Earth's core. Experiments by Vanyo et al. (1995) showed that, to a leading-order approximation, the core behaves like a rigid body rotation, with its rotation axis lagging behind that of the mantle in precession. In addition to this primary rotation, secondary flows arise, such as cylindrical structures coaxial with the fluid rotation vector and columnar wave patterns forming between the cylinders (see Figure 1.3). An analytical solution for fluid rotation with a spheroidal CMB was first provided by Busse (1968). The solution that Busses found is stationary in the precessing frame. However, numerical simulations by Noir and Cébron (2013) showed that for a non-axisymmetric ellipsoid, the resulting flow is unsteady and periodic.

The theory of precession forms the foundation for the subsequent discussion on turbulence and surface roughness effects. It describes how the liquid core behaves when the mantle undergoes precession, influenced by the coupling mechanisms at the CMB. The motion of the liquid core is referred to as precession-driven flow. In this thesis, we focus on the leading-order approximation, where the core exhibits solid body rotation. A clear understanding of these overall flow dynamics is essential for investigating the two key effects of turbulence and roughness explored here.

To begin with, let's consider a simplified two-layered planet with an incompressible and viscous fluid core and a mantle rotating with angular velocity $\boldsymbol{\Omega}_m$ and precessing with angular velocity $\boldsymbol{\Omega}_p$. The CMB is assumed to be spheroidal. The angle between $\boldsymbol{\Omega}_m$ and $\boldsymbol{\Omega}_p$ is denoted as α, the precession angle. In the case of weak precession ($\Omega_p \ll \Omega_m$), the leading order solution for the flow may be expressed as a solid body rotation $\boldsymbol{\Omega}_f$, which represents the mean rotation vector of the fluid. Since the dominant forcing in the system is solely related to precession and the fluid viscosity ν, the orientation of $\boldsymbol{\Omega}_f$ depends on their relative amplitudes. If the viscosity is large enough, then $\boldsymbol{\Omega}_f$ will tend to be aligned with $\boldsymbol{\Omega}_m$; otherwise, it will be aligned with $\boldsymbol{\Omega}_p$.

To better comprehend the physics behind the flow, we choose to sit in the precessing frame. The advantage is two-fold: (1) the Poincaré term is absent given constant $\boldsymbol{\Omega}_p$ and (2) a stationary solution can be found in this frame (e.g. Busse, 1968). By considering the flow stationary, the Navier-Stokes equation becomes

$$2\boldsymbol{\Omega}_p \times \boldsymbol{u} + \boldsymbol{u} \cdot \nabla \boldsymbol{u} = -\frac{1}{\rho}\nabla P + \nu \nabla^2 \boldsymbol{u} \tag{1.1}$$

Notice that precession comes into play through the Coriolis term. After applying $\boldsymbol{r}\times$ to the equation and integrating over the volume V, we arrive at the torque balance equation[3]. Except for the Coriolis term, other terms can be converted into surface integral form. We arrive

$$\begin{aligned} \int_V \boldsymbol{r} \times (2\boldsymbol{\Omega}_p \times \boldsymbol{u})\, dV + \oint_{\partial V} (\boldsymbol{r} \times \boldsymbol{u})(\boldsymbol{u} \cdot \hat{\boldsymbol{n}}) dS = \\ -\frac{1}{\rho} \oint_{\partial V} (\boldsymbol{r} \times \hat{\boldsymbol{n}}) P dS + \nu \oint_{\partial V} \left[\boldsymbol{r} \times (\hat{\boldsymbol{n}} \cdot \nabla)\boldsymbol{u} - \boldsymbol{u} \times \hat{\boldsymbol{n}}\right] dS \end{aligned} \tag{1.2}$$

With the no-penetration condition, the second term on the left-hand side becomes zero. With a spherical boundary, the pressure term becomes zero. In the end, the torque related to precession is balanced by the viscous torque. These are the two competing mechanisms, pressure and viscous coupling, that determine the flow field $\boldsymbol{u}$. Noir et al. (2003) showed that the torque balance equation can be used to solve for the fluid rotation $\boldsymbol{\Omega}_f$, which is given in the precessing frame where a Cartesian coordinate system $(\hat{\boldsymbol{X}}_p', \hat{\boldsymbol{Y}}_p', \hat{\boldsymbol{Z}}_p')$ is defined such that the $\hat{\boldsymbol{Z}}_p'$-axis and $\boldsymbol{\Omega}_m$ are aligned and $\boldsymbol{\Omega}_p$ is tilted toward the $\hat{\boldsymbol{X}}_p'$-axis.

For demonstration purposes, let's consider a case with spherical CMB. The precession angle is $\alpha = 30°$ and the Poincaré number $Po = \Omega_p/\Omega_m = 10^{-3}$. Figure 1.4 is a polar plot showing the angular coordinates of $\boldsymbol{\Omega}_f$. The concentric

[3] Specifically, it is *unit density* torque balance equation. The dimension is torque per density.

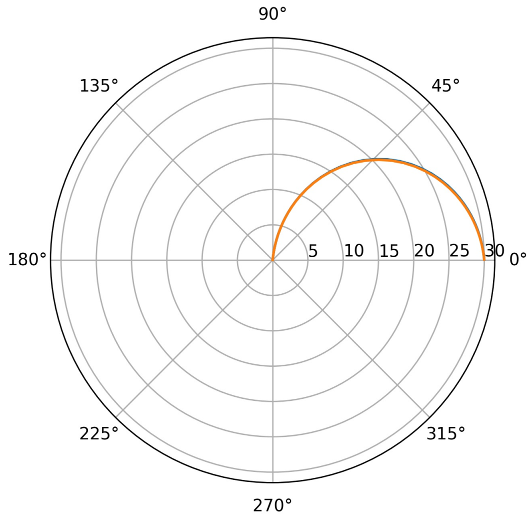

Figure 1.4: Polar plot showing the angular coordinates θ_f and ϕ_f of $\mathbf{\Omega}_f$. The pole aligns with $\mathbf{\Omega}_m$ while $\mathbf{\Omega}_p$ is at $\theta = 30°$. The curve shows the path of $\mathbf{\Omega}_f$ when E is decreasing from 10^{-1} to 10^{-12}, with the direction from $\mathbf{\Omega}_m$ toward $\mathbf{\Omega}_p$.

line indicates the co-latitude θ measured from $\hat{\boldsymbol{Z}}'_p$. There are two facts regarding the solution: First, the fluid rotation vector is closer to $\mathbf{\Omega}_m$ when viscosity is larger (i.e. E large), while closer to $\mathbf{\Omega}_p$ when viscosity is small. Second, the path of $\mathbf{\Omega}_f$ between the two end members is not a straight line, but a curve.

Relevant parameters for the Earth's and the Moon's core precession are summarized in Table 1.1. First of all, it is necessary to address the fluid viscosity ν of liquid iron, the major composition in the cores of the Earth and the Moon. In the following, the value $\nu = 10^{-6}\,\mathrm{m^2\,s^{-1}}$ is adopted if not mentioned otherwise. The parameters (mostly for Earth), if not specified, are referred to in the textbook by Stacey and Davis (2008). For example, one sidereal day has 86164 seconds, corresponding to $\Omega_m = 7.292 \times 10^{-5}\,\mathrm{rad\,s^{-1}}$ and the precession period is 25770 years. Thus, the Poincaré number for Earth is $Po = 10^{-6}$. The precession angle is $\alpha = 23.45°$. The CMB radius is 3480 km, leading to $E = 10^{-15}$. The flattening of CMB derived from the nutation theory is $\epsilon_f = 2.6 \times 10^{-3}$, about 4% larger than the hydrostatic equilibrium value (Mathews et al., 2002). For the Moon, the rotation rate is $2.662 \times 10^{-6}\,\mathrm{rad\,s^{-1}}$ and the precession period is 18.6 years. The Poincaré number for the Moon is $Po = 4 \times 10^{-3}$. The precession angle is $\alpha = 1.54°$. According to the review by Breuer et al. (2022), the estimate for the Moon's core radius ranges from 200 to 380 km, which means $E \leq 3 \times 10^{-12}$. This extreme value is taken in the following discussion. For the flattening of the lunar core, I take the core oblateness $(2.2 \pm 0.6) \times 10^{-4}$ estimated from lunar laser ranging data by Viswanathan et al. (2019).

Let's begin with the Moon. By considering only the viscous torque, Gol-

Table 1.1: Parameters of the Earth and the Moon relevant for core precession.

	Earth	Moon
Rate of rotation Ω_m (rad s^{-1})	7.292×10^{-5}	2.662×10^{-6}
Rate of precession Ω_p (rad s^{-1})	7.726×10^{-12}	1.070×10^{-8}
Obliquity α (deg)	23.45	1.54
Viscosity ν (m^2 s^{-1})	10^{-6}	10^{-6}
Radius R (km)	3480	200 - 380
Thickness L_ν (m)	0.1	0.6
Velocity U (m s^{-1})	4.1×10^{-3}	2.6×10^{-2}
Poincaré number Po	1×10^{-7}	4×10^{-3}
Ekman number E	1×10^{-15}	2.6×10^{-12}
Reynolds number Re	481	1.58×10^4

dreich (1967) showed that the minimum viscosity to precess the lunar core at 18.6 years is given $\nu = 20r^2\,\mathrm{m^2\,s^{-1}}$, where r is the core radius in the units of lunar surface radius. Given the lunar surface radius 1738 km, the minimum viscosity is around 0.3 to 1.0 m^2 s^{-1}, at least five orders larger than the conventional value. It suggests that the core is barely participating in the precession. Figure 1.5 shows the angle between $\boldsymbol{\Omega}_f$ and $\boldsymbol{\Omega}_m$, denoted as θ_f. Two cases are presented: spherical and spheroidal boundaries. For the Moon, we found $\theta_f = 1.47°$ and $\phi_f = 5.72 \times 10^{-2}$ (deg). At low E, we see that the effect of flattening is to bring $\boldsymbol{\Omega}_f$ closer to $\boldsymbol{\Omega}_m$. We could imagine it in a physical way. The flattening of the boundary acts like a handle. The torque exerted on it will tend to align $\boldsymbol{\Omega}_f$ and the symmetry axis of the mantle, which is close to $\boldsymbol{\Omega}_m$. This tenancy is similar to the one affected by viscosity as the friction tends to reduce the differential motion across the boundary. That is to say, we may treat both flattening and viscosity as competing mechanisms and see which one is dominant at a given viscosity (i.e. E for other parameters remains unchanged). At high E, the two solutions are almost identical, implying that the flattening effect is negligible, while at low E the solutions begin to deviate, suggesting the other way around. For the Moon, the expected Ekman number is in the order of 10^{-12}. The difference between the two solutions is 0.07°, about 5%. In conclusion, the picture of a barely precessing lunar core remains as the boundary flattening is too small to alter the result.

For Earth, the effect of flattening is much larger. Figure 1.6 shows the angle θ_f as a function of E. At $E = 10^{-15}$, we have $\theta_f = 9.29 \times 10^{-4}$ (deg) and $\phi_f = 1.93 \times 10^{-3}$ (deg). The angle θ_f is smaller than 10^{-3} degrees, meaning the Earth's core is almost aligned with $\boldsymbol{\Omega}_m$. Besides, we also see the two features regarding the flattening, compared to the case of the Moon. First, the flattening is large enough so that the angle θ_f is significantly reduced. Second,

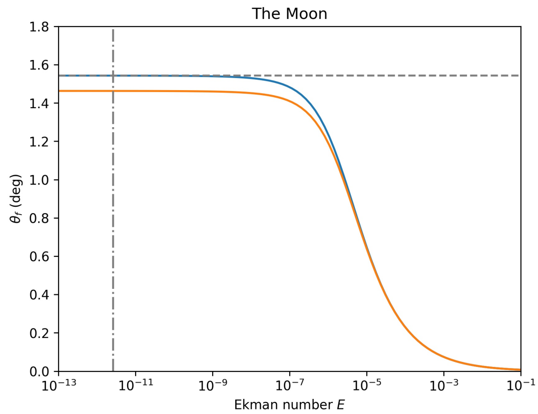

Figure 1.5: The solution of θ_f as a function of E for the Moon. The solution is obtained from the implicit equation of Busse (1968), with the flattening $\epsilon_f = 2.2 \times 10^{-4}$ (orange curve). The case with spherical boundary (i.e. $\epsilon_f = 0$) is presented for comparison (blue curve). The horizontal dash line is the obliquity $\alpha = 1.54°$. The vertical dash-dot line is the Ekman number of the Moon $E = 2.6 \times 10^{-12}$. For the Moon, the solution gives $\theta_f = 1.47°$ and $\phi_f = 5.72 \times 10^{-2}$ (deg).

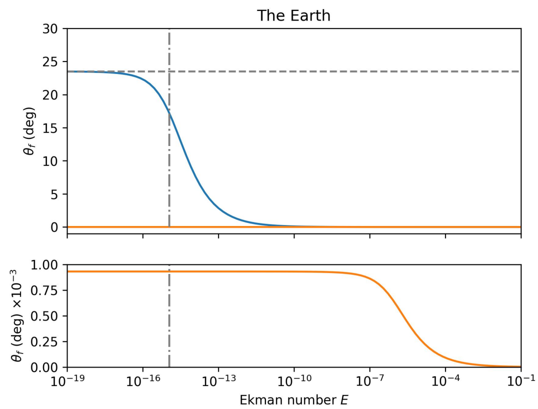

Figure 1.6: The solution of θ_f as a function of E for the Earth. The solution is obtained from the implicit equation of Busse (1968), with the flattening $\epsilon_f = 2.6 \times 10^{-3}$ (orange curve). The case with spherical boundary (i.e. $\epsilon_f = 0$) is presented for comparison (blue curve). The horizontal dash line is the obliquity $\alpha = 23.45°$. The vertical dash-dot line is the Ekman number of the Earth $E = 10^{-15}$. For the Earth, the solution gives $\theta_f = 9.29 \times 10^{-4}$ (deg) and $\phi_f = 1.93 \times 10^{-3}$ (deg). The lower panel is presented to specifically demonstrate the variation of the orange curve.

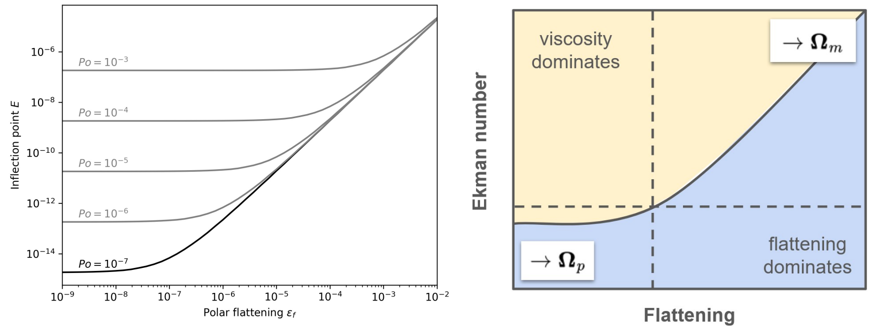

Figure 1.7: The inflection point E as a function of flattening ϵ_f with various Poincaré number Po. The inflection point E is obtained by taking the second derivative of θ_f with respect to E for each given pair of ϵ_f and Po. The black curve with $Po = 10^{-7}$ can be related to the result for the Earth presented in Figure 1.6. For example, the inflection point E is about 10^{-15} when $\epsilon_f = 0$ (blue cure), while 10^{-6} when $\epsilon_f = 2.6 \times 10^{-3}$ (orange curve). The figure on the right hand side is a schematic diagram, showing the two domains separated by the curve and the four quadrants originated at the turning point (see the text for the discussion).

the transition of θ_f depends on ϵ_f. From the lower panel of Figure 1.6 we see that the transition occurs at $E \approx 10^{-5}$, rather than the spherical case at $E \approx 10^{-14}$. It becomes clear if we slowly vary ϵ_f and use the inflection point (where the second derivative equals zero) to represent the transition (see Figure 1.7). The black curve has $Po = 10^{-7}$, representing the Earth with varying ϵ_f, while the gray curves have larger Po, values indicated in the figure. For all cases, the E's of the inflection points become insensitive to ϵ_f when ϵ_f is smaller than some critical value. These critical values are equal qualitatively to their corresponding Poincaré numbers. If we can divide the whole area in the RHS part of Figure 1.7 into four quadrants with the critical point as the origin, then the solution of $\mathbf{\Omega}_f$ in the top-right quadrant will be closer to $\mathbf{\Omega}_m$ as the viscosity and the flattening are large. On the other hand, in the bottom-left quadrant, the solution of $\mathbf{\Omega}_f$ will be closer to $\mathbf{\Omega}_p$. The curve itself distinguishes two regions: the upper region is dominated by viscosity while the lower one is by flattening. For example, in the upper region, for a given E, the variation in ϵ_f will not significantly alter the solution, and vice versa.

1.6 Scope of the present study

The major focus of this thesis is on the boundary layer generated by precession-driven flow. The boundary layer is simulated numerically using a local box model, which is capable of exploring the turbulent regime and the effect of surface roughness. The effect of turbulence is examined in the context of planetary applications for the Earth and the Moon, as well as in laboratory experiments. The roughness effect is studied by imposing a surface profile on the boundary.

The work will be mainly concentrated on the numerical implementation and the perspective

The effect of turbulence on the boundary layer dissipation is discussed in Chapter 2, where the central scientific question is: what is the upper bound for turbulent dissipation in the boundary layer? While this upper bound has been inferred from Earth's rotation observations, it has not yet been established through numerical simulations. I will first present the theory for precession, discuss the nature of the precession-driven flow, and then derive the governing equation for the boundary layer flow, together with the corresponding analytical solutions for the flow and the shear stress. The relation to the solution of precession-driven flow is further discussed by considering the viscous torque and the dissipation. I address the numerical implementation of the box model which is used to study the boundary layer flow. Friction velocity and kinetic energy serve as the proxies for individual simulation. Mean velocity profiles are presented to check if the boundary layer becomes turbulent and the result is suitable for the similarity theory, which is used for extrapolation for the more extreme parameter regime. Viscous dissipation is computed for their direct implications for the Earth and the Moon.

Since the solution for precession-driven flow obtained in literature is generally based on laminar viscous torque, it is important to understand how the solution changes when turbulent torque is considered. In Chapter 3, I demonstrate the derivation for the torques to be expressed in terms of surface integral. Then I focus on the viscous torque and estimate the torque when the boundary layer becomes turbulent. Finally, I use the turbulent torque to recalculate the solution for $\boldsymbol{\Omega}_f$ and discuss the implications for the Earth and the Moon as well as for laboratory experiment setup.

Chapter 4 addresses the effect of surface roughness, which has been proposed to enhance dissipation in the boundary layer. The aim is to determine how introducing surface roughness impacts our findings on turbulent dissipation. After reviewing the problem formulation for the boundary layer in precession-driven flow, the chapter moves to the numerical implementation with a focus on the surface roughness. A simple laminar case is presented to demonstrate the validity of the method, followed by results in the turbulent regime.

Chapter 2

Turbulent dissipation in the boundary layer of precession-driven flow in a sphere

This chapter is reproduced and modified from the following publication: Sheng-An Shih, Santiago Andrés Triana, Jérémy Rekier, Véronique Dehant; Turbulent dissipation in the boundary layer of precession-driven flow in a sphere. AIP Advances 1 July 2023; 13 (7): 075025. https://doi.org/10.1063/5.0146932, with the permission of AIP Publishing. Minor modifications, including rearrangements and revisions, have been made to enhance the clarity and readability of the text.

2.1 Introduction

The free core nutation (FCN) is a rotational normal mode of the Earth. Since its frequency is close to a forced nutation, the retrograde annual nutation, some properties of the FCN can be determined by measuring the resonant amplitude and the phase lag of the forced nutation (e.g., Herring et al., 1986). Inversions based on the observed phase lag placed an upper bound for the fluid core kinematic viscosity of $0.54\,\mathrm{m^2\,s^{-1}}$ (Gwinn et al., 1986), about six orders larger than the value inferred from studies of liquid metal (see the review of Lums & Aldridge, 1991); a low viscosity around $\nu = 10^{-6}\,\mathrm{m^2\,s^{-1}}$ is still favoured by recent studies based on ab inito calculations (e.g., Pozzo et al., 2013; Ichikawa & Tsuchiya, 2015). Turbulence in the core's boundary layers can lead in principle to an enhanced eddy viscosity. Ohmic dissipation in the core and mantle can also explain the discrepancy in viscosity (e.g., Buffett, 1992; Mathews & Guo, 2005; Deleplace & Cardin, 2006; Buffett & Christensen, 2007). However, accounting for the observed phase lag requires either a strong magnetic field at the core-mantle boundary (CMB) or a highly conductive layer at the base of the mantle (Buffett et al., 2002; Mathews et al., 2002). Although the flow near the CMB associated with the FCN motion is too weak to be turbulent, the flow associated with precession might be strong enough to be turbulent (Buffett, 2021; Triana et al., 2021). Thus it is important to properly quantify the turbulent contribution to the energy dissipation from precessional motion to obtain tighter bounds on the Ohmic dissipation.

Instabilities in the boundary layer of a precession-driven flow have been previously identified in numerical simulations (Lorenzani & Tilgner, 2001); however the thinness of the boundary layer makes it difficult to study experimentally (see the review by Tilgner, 2015). That same reason, combined with current computational constraints, preclude numerical studies from reaching parameter regimes appropriate for planetary interiors where the Coriolis force plays a central role. This limitation is reflected in the smallness of the *Ekman number* E, representing the ratio of viscous to Coriolis forces and controlling the thickness of the boundary layer (also known as the Ekman layer). It is well-known that the thickness L_ν of the Ekman layer scales as $E^{1/2}$ (e.g. see P. 188 in Tilgner, 2015). We can define a local Reynolds number Re to quantify the condition for turbulence in the boundary layer as $Re = UL_\nu/\nu$ where ν is the viscosity and U is the velocity. For the nominal value of the Earth's precession-driven flow, the Reynolds number is about $Re = 500$, higher than the critical value of $Re \sim 150$ for the onset of turbulence proposed by Sous et al. (2013). With a global spherical model, Cébron et al. (2019) show that the total viscous dissipation increases by a factor of 1.17 compared to the laminar solution when Re is around 230. Buffett (2021) restricts the modeling domain to the boundary layer and breaks it into pieces according to the co-latitude θ. Using a local Cartesian model, similar to ours, he studies two representative cases at $\theta = 0$ and $60°$ and shows that the *friction velocity* u_*, a quantity proportional to the square root of the surface shear stress (see the definition below), increases by a factor of 1.2 at $Re = 500$ compared to the laminar value. Buffett (2021) demonstrates a promising way to study turbulent effects in the boundary layer from a local point of view. However, the connection to the global picture is still missing. Dissipation depends not only on the surface shear stress but also on *veering angle* β, the angle between the stress and the fluid velocity on the boundary. In the present work, we investigate numerically the local flow at different co-latitudes, integrating the results to obtain global estimates of the possibly turbulent energy dissipation.

Energy dissipation in the lunar core due to precession is a key parameter to understand the possible dynamo action in the past (Stys & Dumberry, 2020; Zhang & Dumberry, 2021). The Re for the boundary layer flow is about 10^4, much larger than Earth's. Therefore, it has been believed that the boundary layer is turbulent (e.g., Yoder, 1981). The model by Buffett (2021) is in principle not applicable to the moon not only because of the much higher Reynolds number, but also because the flattening in their model must be much larger than the ratio of precession to rotation (i.e. the Poincaré number Po). However, in the lunar case, the latter condition is not met as the CMB flattening of 10^{-4} (Viswanathan et al., 2019) is smaller than the Poincaré number, $Po = 4 \times 10^{-3}$. In order to extend the result of Buffett (2021), we investigate the problem by considering the case where the flattening is zero, i.e., a precessing fluid in a spherical cavity.

The scaling of quantities in the boundary layer can be used to estimate the dissipation at large Re. The theory for the scaling of u_* and β in the Ekman layer was proposed by Csanady (1967). It was later improved by Spalart (1989) to include higher order terms. The scaling has been studied via laboratory experiments (Caldwell et al., 1972; Sous et al., 2013) and numerical simulations (Coleman et al., 1990; Coleman, 1999; Shingai & Kawamura, 2004; Deusebio et al., 2014; Braun et al., 2020). However, the Ekman layer in those studies is steady, i.e., it remains constant in time, contrary to the one from precession-driven flow which oscillates with diurnal frequency. The study of a Stokes boundary layer, i.e. an oscillating boundary layer but without Coriolis force, reveals complex behavior during the transition to turbulence: an instability growing in one oscillation cycle may eventually decay at intermediate Re (Ozdemir et al., 2014). Besides, analytical solutions show that the u_* associated with an oscillatory Ekman layer is smaller than that of a steady Ekman layer by a factor of $2^{1/4}$ (Buffett, 2021). Therefore, we want to know if the scaling is applicable to the oscillatory Ekman layer typical in precession-driven flow and establish the difference with those previous studies.

To investigate the turbulent dissipation in the boundary layer of precession-driven flow, we conducted numerical simulations of an oscillatory flow under rotation, also known as the oscillatory Ekman layer, within a local Cartesian domain. Viscous dissipation was estimated for each simulation. Assuming that these simulations approximate the local boundary layer of precession-driven flow, we derived the total viscous dissipation across the entire boundary layer. The results are compared with existing literature in the laminar regime, and we discuss their implications for the Earth and the Moon in the turbulent regime.

2.2 Problem formulation

2.2.1 Precession-driven flow

We consider a spherical cavity with radius R filled with an incompressible and viscous fluid, rotating with angular velocity $\mathbf{\Omega}_m$, and precessing with angular velocity $\mathbf{\Omega}_p$. The angle between $\mathbf{\Omega}_m$ and $\mathbf{\Omega}_p$ is denoted as α, the precession angle. In the case of weak precession ($\Omega_p \ll \Omega_m$), the leading order solution for the flow in the cavity may be expressed as a solid body rotation $\mathbf{\Omega}_f$, which represents the mean rotation vector of the fluid. According to Busse's theory (Busse, 1968), $\mathbf{\Omega}_f$ can be determined given the Poincaré number $Po = \Omega_p/\Omega_m$, the Ekman number $E = \nu/(\Omega_m R^2)$, and the precession angle α. We choose our reference frame as the one rotating with the fluid's mean angular velocity, and we refer to it as the *fluid frame*. In such frame the bulk of the fluid remains at rest, and the cavity rotates with an angular velocity $\Delta\mathbf{\Omega} = (\mathbf{\Omega}_m - \mathbf{\Omega}_f)$. A boundary layer exists, the main focus of our study, with a nominal thickness $L_\nu = \sqrt{\nu/\Omega_f}$.

To determine $\mathbf{\Omega}_f$ we use the reduced model of Cébron et al. (2019) (i.e., their Eqs. 5-7), which yields results consistent with the steady-state solution derived by Busse (1968) for the cases considered in this study. Their solutions are obtained in the precessing frame where a Cartesian coordinate system$(\hat{\boldsymbol{X}}_p^{'}, \hat{\boldsymbol{Y}}_p^{'}, \hat{\boldsymbol{Z}}_p^{'})$ is defined such that $\hat{\boldsymbol{Z}}_p^{'}$-axis and $\boldsymbol{\Omega}_m$ are aligned. The spherical coordinates of $\boldsymbol{\Omega}_f$ are denoted as the co-latitude θ_f and the longitude ϕ_f. The coordinates are transformed to the local system by three steps: (1) rotation of the coordinate system to align the $\hat{\boldsymbol{Z}}_p^{'}$-axis with $\boldsymbol{\Omega}_f$, (2) transformation from the precessing frame to the fluid frame, and (3) transformation from the global system to the local system. Details about the transformation are given in Appendix 2.A.

2.2.2 Governing equations

In the fluid frame, we define two Cartesian coordinate systems: one global $(\hat{\boldsymbol{X}}, \hat{\boldsymbol{Y}}, \hat{\boldsymbol{Z}})$ and one local $(\hat{\boldsymbol{x}}, \hat{\boldsymbol{y}}, \hat{\boldsymbol{z}})$ (Figure 2.1). For the global coordinate system, $\hat{\boldsymbol{Z}}$ is aligned with $\boldsymbol{\Omega}_f$ and the coordinate system co-rotates with the fluid. For the local coordinate system, the x-axis is eastward, the y-axis is northward, and the z-axis is in radial outward direction. The fluid domain extends from $z = 0$ toward the negative z-axis. In the fluid frame, the flow velocity $\boldsymbol{u}$ satisfies the Navier-Stokes equation:

$$\frac{\partial \boldsymbol{u}}{\partial t} + \boldsymbol{u} \cdot \nabla \boldsymbol{u} + 2\left(\boldsymbol{\Omega}_f + \boldsymbol{\Omega}_p\right) \times \boldsymbol{u} = -\frac{\nabla P}{\rho} + \nu \nabla^2 \boldsymbol{u} + \boldsymbol{r}' \times \left(\boldsymbol{\Omega}_p \times \boldsymbol{\Omega}_f\right) \qquad (2.1)$$

where P is the reduced pressure including the centrifugal force and $\boldsymbol{r}'$ is the position vector referring to any point inside the cavity. The last term, $\boldsymbol{r}' \times (\boldsymbol{\Omega}_p \times \boldsymbol{\Omega}_f)$, is known as the Poincaré term (coined by Malkus, 1968) or the Euler term, which is associated with the fictitious force appearing in such a non-uniformly rotating reference frame. Since the flow is mainly confined to the viscous boundary layer, we take L_ν as the length scale to analyze Equation 2.1. We further assume L_ν is much smaller than the cavity radius R, so the cavity curvature is neglected in the local model. Together with the differential velocity $U = R|\Delta\boldsymbol{\Omega}|$ as the velocity scale, Equation 2.1 can be written in dimensionless form:

$$\begin{aligned} \frac{\partial \boldsymbol{u}^*}{\partial t^*} + \boldsymbol{u}^* \cdot \nabla^* \boldsymbol{u}^* + \frac{2}{Re}\left[\hat{\boldsymbol{k}}_f + Po\left(\frac{\Omega_m}{\Omega_f}\right)\hat{\boldsymbol{k}}_p\right] \times \boldsymbol{u}^* &= -\nabla^* P^* + \frac{1}{Re}\nabla^{*2}\boldsymbol{u}^* \\ + \left(\frac{L_\nu}{R}\right)\left(\frac{\Omega_m}{\Delta\Omega}\right)^2 Po\left(\frac{\Omega_f}{\Omega_m}\right)&\left[\left(\frac{L_\nu}{R}\right)\boldsymbol{r}^* + \hat{\boldsymbol{R}}\right] \times \left(\hat{\boldsymbol{k}}_p \times \hat{\boldsymbol{k}}_f\right) \end{aligned} \qquad (2.2)$$

where $Re = UL_\nu/\nu$ is the Reynolds number and $\hat{\boldsymbol{R}} = \boldsymbol{R}/R$ is a unit vector. A superscript $(^*)$ denotes dimensionless variables (the variable $\boldsymbol{u}^*$ is not to be confused with the friction velocity u_* introduced later below). In the local coordinate system, the vector $\hat{\boldsymbol{k}}_f$ is given by $\cos\theta\,\hat{\boldsymbol{z}} + \sin\theta\,\hat{\boldsymbol{y}}$, where θ is the co-latitude.

Before moving on to the boundary conditions, it is necessary to specify the orientations of $\boldsymbol{\Omega}_m$ and $\boldsymbol{\Omega}_f$ in a coordinate system defined in the precessing frame, which is rotating with $\boldsymbol{\Omega}_p$. The coordinate system, denoted as $(\hat{\boldsymbol{X}}_p, \hat{\boldsymbol{Y}}_p, \hat{\boldsymbol{Z}}_p)$, is defined such that it coincides with $(\hat{\boldsymbol{X}}, \hat{\boldsymbol{Y}}, \hat{\boldsymbol{Z}})$ at $t = 0$.

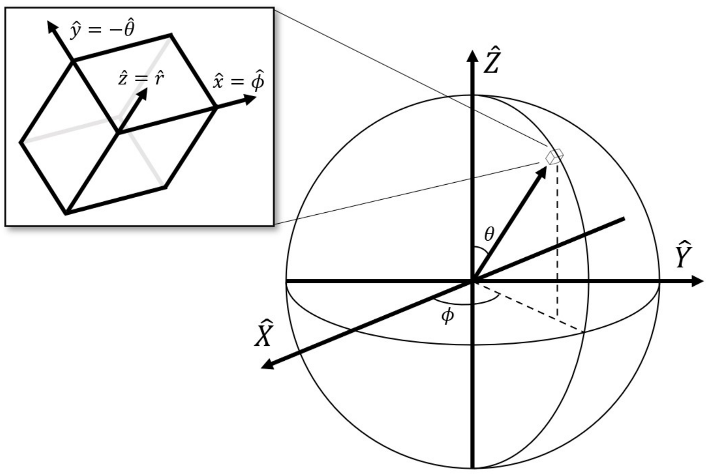

Figure 2.1: The sketch of a spherical cavity with a local box. Two coordinate systems are shown: global $(\hat{\boldsymbol{X}}, \hat{\boldsymbol{Y}}, \hat{\boldsymbol{Z}})$ and local $(\hat{\boldsymbol{x}}, \hat{\boldsymbol{y}}, \hat{\boldsymbol{z}})$. The two vectors $\hat{\boldsymbol{x}}$ and $\hat{\boldsymbol{y}}$ denote the unit vectors along the directions of longitude ϕ and (negative) co-latitude θ, while $\hat{\boldsymbol{z}}$ is along the radially outward direction.

Moreover, $\boldsymbol{\Omega}_m$ is tilted toward negative $\hat{\boldsymbol{X}}_p$, forming an angle θ_f relative to $\boldsymbol{\Omega}_f$ (see below for the definition of θ_f). Under the no spin-up condition (i.e., $\Omega_f = \Omega_m \sin\theta_f$), the differential rotation vector will be lying on the equatorial plane: $\Delta\boldsymbol{\Omega} = -\Delta\Omega\hat{\boldsymbol{X}}_p$. The coordinate is then transformed to $(\hat{\boldsymbol{X}}, \hat{\boldsymbol{Y}}, \hat{\boldsymbol{Z}})$ in the fluid frame and further to $(\hat{\boldsymbol{x}}, \hat{\boldsymbol{y}}, \hat{\boldsymbol{z}})$ for the computation of boundary velocity, which is $\Delta\boldsymbol{\Omega} \times \boldsymbol{R}$. In the local coordinate system, the boundary condition at the lower end ($z^* \to -\infty$) is $\boldsymbol{u}^* = 0$ (i.e., the bulk of the fluid sufficiently away from the boundary is at rest). Note that, in the numerical implementation discussed below, the lower end is set at $z^* = -30$. On the fluid surface ($z^* = 0$, corresponding to the CMB), the components of the velocity are given by

$$u_x^* = \cos\theta\cos(\Omega_f t + \phi) \tag{2.3a}$$

$$u_y^* = -\sin(\Omega_f t + \phi) \tag{2.3b}$$

$$u_z^* = 0 \tag{2.3c}$$

where ϕ is the longitude. Thanks to the azimuthal $m = 1$ symmetry of the flow, it is anticipated that the local flow field at a given ϕ_0 is equivalent to the flow at the prime meridian ($\phi = 0$) with a lag time ϕ_0/Ω_f. For the numerical implementation, we set $\phi = 0$ and then the azimuthal dependence is retrieved directly from $\Omega_f t$ for post-processing analysis. That is, a time-average can be treated as an azimuthal average.

We use the lunar parameters listed in Table 2.1 as an end-member case to estimate the amplitude of the Poincaré term, where $|\hat{\boldsymbol{k}}_p \times \hat{\boldsymbol{k}}_f| = \sin\gamma$. The ratio of the amplitudes of the Poincaré term to the viscous term is 4×10^{-6}, the value obtained in the turbulent regime where $Re = 1.67 \times 10^4$. In the

Table 2.1: Lunar parameters used in this study. R is the radius of lunar core-mantle boundary (Viswanathan et al., 2019). α is the angle between the symmetry axis and the ecliptic normal. We use Eqs. (5-7) of Cébron et al. (2019) to compute $\boldsymbol{\Omega}_f$; the orientation (θ_f, ϕ_f) is given the coordinate system $(\hat{\boldsymbol{X}}'_p, \hat{\boldsymbol{Y}}'_p, \hat{\boldsymbol{Z}}'_p)$ whose $\hat{\boldsymbol{Z}}'_p$ is aligned with $\boldsymbol{\Omega}_m$. The angle between $\boldsymbol{\Omega}_f$ and $\boldsymbol{\Omega}_p$ is denoted by γ.

Parameter	Definition	Units	Value
ν		$\mathrm{m^2\,s^{-1}}$	10^{-6}
Ω_m		$\mathrm{rad\,s^{-1}}$	2.66×10^{-6}
Ω_f	$\Omega_m \cos\theta_f$	$\mathrm{rad\,s^{-1}}$	2.659×10^{-6}
Ω_p		$\mathrm{rad\,s^{-1}}$	1.07×10^{-8}
R		km	380
L_ν	$\sqrt{\nu/\Omega_f}$	m	0.61
α		degree	1.543
θ_f		degree	1.543
ϕ_f		degree	0.060
γ		degree	0.002
U	$R\,\Omega_m \sin\theta_f$	$\mathrm{m\,s^{-1}}$	2.72×10^{-2}
Po	Ω_p/Ω_m		4×10^{-3}
E	$\nu/(R^2\Omega_m)$		3×10^{-12}
Re	UL_ν/ν		1.67×10^4

laminar regime, say $Re = 5$, we find the ratio is 7×10^{-3}, thus allowing us to drop the Poincaré term in the Re range discussed in the present study. Second, we consider the magnitude of (Ω_m/Ω_f), which is equal to $\cos^{-1}\theta_f$ under the no spin-up condition. Given $\theta_f = 1.543°$ at $Re = 1.67 \times 10^4$, the magnitude is very close to unity with a difference of 0.04%. With lower Re (high ν), the angle θ_f will be even smaller, thus making (Ω_f/Ω_m) closer to unity. Third, the condition of weak precession ($Po \ll 1$) allows us to drop the precession vector in the Coriolis term. With these approximations, we arrive at the reduced form of Equation 2.2:

$$\frac{\partial \boldsymbol{u}^*}{\partial t^*} + \boldsymbol{u}^* \cdot \nabla^* \boldsymbol{u}^* + \frac{1}{Re}\left(2\hat{\boldsymbol{k}}_f \times \boldsymbol{u}^*\right) = -\nabla^* P^* + \frac{1}{Re}\nabla^{*2}\boldsymbol{u}^* \tag{2.4}$$

For comparison, we solve numerically both Equations 2.2 and 2.4 at $Re = 500$ and find no significant difference between the two solutions. In other words, neglecting the precessional terms makes no difference in our case. In the following all the discussion will be based on Equation 2.4. We note that Equation 2.4 is generally identical to the one derived for a precessing spheroidal cavity (see the Appendix of Buffett, 2021), even though the reasons to drop the Poincaré term are different. In a precessing spheroid, the Poincaré term is balanced by the terms associated with the flattening. Nevertheless, both formulations make the governing equation resemble a simple rotating fluid. The appearance of Equation 2.4 may seem counter-intuitive indeed, but it is important to remember the initial assumption that the container is precessing and that the flow is mostly a uniform vorticity flow. The local model aims to examine the flow in a small rectangular box near the boundary. Precession comes into play when we determine $\boldsymbol{\Omega}_f$. The only difference to Buffett (2021) lies in the selection of the rotation vector, where we employ $\boldsymbol{\Omega}_f$ in contrast to $\boldsymbol{\Omega}_m$. Considering the aforementioned assumption, that is, $\Omega_f/\Omega_m \approx 1$, the discrepancy between the two vectors becomes negligible. Nevertheless, we think that adopting $\boldsymbol{\Omega}_f$ is more appropriate and self-consistent as the local model requires the bulk fluid to be at rest, a condition that may not hold when employing $\boldsymbol{\Omega}_m$ in the mantle frame. In Appendix 2.B, we derive the analytical solution in the laminar regime where Re is small and the non-linear term can be neglected, which matches the numerical result as expected.

2.2.3 Viscous dissipation

We are interested in quantifying the energy dissipation in the boundary layer. In the local system, the input (output) power from the surface shear stress $\boldsymbol{\tau}$ is equal to the increase (decrease) of internal and kinetic energies (see e.g. Section 16 in Landau & Lifshitz, 1987):

$$S\,(\boldsymbol{u}\cdot\boldsymbol{\tau})_{z=0} = \dot{E}_{\mathrm{int}} + \dot{E}_{\mathrm{kin}} \tag{2.5}$$

where S is the surface area. The increase in internal energy is further linked to the energy dissipated in the system. Therefore, for an equilibrium system where the change of kinetic energy reaches zero, the viscous power can be used to infer the dissipation. Suppose that the area S correspond to a small patch on the cavity surface $dS = \sin\theta\, R^2\, d\theta\, d\phi$. We compute the total dissipation via $\mathcal{D}_\nu = -\int(\boldsymbol{\tau}\cdot\boldsymbol{u})dS$. The local viscous power per unit area is defined as $\mathcal{P}^{\mathrm{visc}} = \boldsymbol{\tau}\cdot\boldsymbol{u}$ for later use. We can integrate the laminar analytical solutions to obtain the global laminar dissipation as (e.g. Cébron et al., 2019)

$$\mathcal{D}_\nu^{\mathrm{lam}} = -2.62\, I\Delta\Omega^2\sqrt{\nu\Omega}/R \tag{2.6}$$

where $I = (8\pi/15)\rho R^5$ is the moment of inertia of the fluid. This result is consistent with the torque approach, which is given Appendix 2.B.

In the turbulent regime, the surface shear stress no longer follows the analytical solution, so we prescribe the turbulent stress as $k\rho|\boldsymbol{u}|\boldsymbol{u}$ (e.g. Williams et al., 2001), where k is a dimensionless parameter which depends on the viscosity. The total turbulent dissipation $-(45\pi/32)kI\Delta\Omega^3$ is obtained by integrating the negative viscous power over the spherical surface. Since the dissipation is independent of the orientation of $\Delta\boldsymbol{\Omega}$, one can take $\Delta\boldsymbol{\Omega} = \Delta\Omega\hat{\boldsymbol{Z}}$ to simplify the computation, as done by Yoder (1981). For an arbitrary orientation, we obtain the same coefficient, $-(45\pi/32)$, by approximating the integral as a Riemann sum. Note that the stress prescription assumes that the stress is aligned with the velocity, which is not true for most cases (see Figure 2.20 for the veering angle at different θ), so the turbulent torque derived from this definition should be thus treated with extra care. In order to determine the parameter k, we adopt the approach by Cébron et al. (2019) and require $\mathcal{P}^{\mathrm{visc}}$, computed from turbulent and laminar stresses (Equations 2.34-2.35), to match at $\theta = 0$; it gives $k = (u_*/U)^2\cos\beta$. We notice that, when we substitute the laminar solutions for u_* and β into k and compute the total turbulent dissipation, the obtained

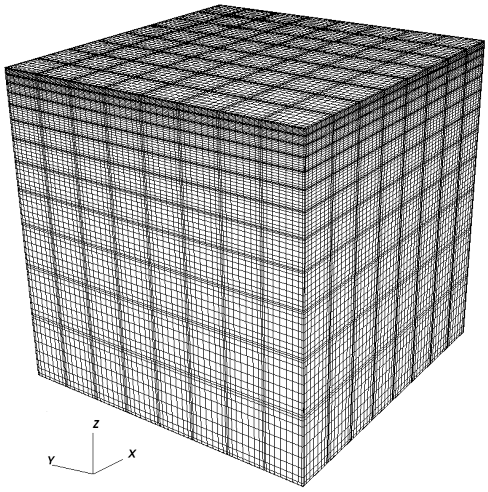

Figure 2.2: Box model with Cartesian coordinates. The typical resolution is $\mathcal{E} = 768$ and $N = 9$. The dimension of the box is $30 \times 30 \times 30$ in the unit of L_ν. Element density is higher near the top boundary to resolve the boundary flow.

dissipation disagrees with the laminar expectation given in Equation 2.6. To reconcile the inconsistency, we define the turbulent dissipation as

$$\mathcal{D}_\nu^{\mathrm{turb}} = -2.62\sqrt{2}kI\Delta\Omega^3 \tag{2.7}$$

In principle, one can match $\mathcal{P}^{\mathrm{visc}}$ at any θ. We choose $\theta = 0$ because the asymptotic similarity theory is used to estimate the friction velocity and veering angle in this special case, where the presence of a logarithmic layer supports the use of the theory. The purpose of this modification is to provide a way to compute k and relate it to the total dissipation, which can be compared to our numerical results.

2.3 Numerical implementation

We use the spectral element code Nek5000 (Fischer et al., 2007) to solve Equation 2.4 for an incompressible fluid in a Cartesian box. The domain is divided into $\mathcal{E}$ elements, where solutions are represented by N-th order Lagrange interpolation polynomials (see Figure 2.2). The typical resolution in the present study is $\mathcal{E} = 768$ and $N = 9$. The temporal discretization is based on a third-order backward-difference scheme for implicit terms and on an extrapolation scheme for explicit terms.

The domain is extended downward from $z = 0$. The non-dimensional size is $30 \times 30 \times 30$. The top boundary is a wall (representing the CMB), where the velocity is specified to mimic the precessing container (mantle) as seen from the fluid frame (recall Equation 2.3). The four lateral boundaries are

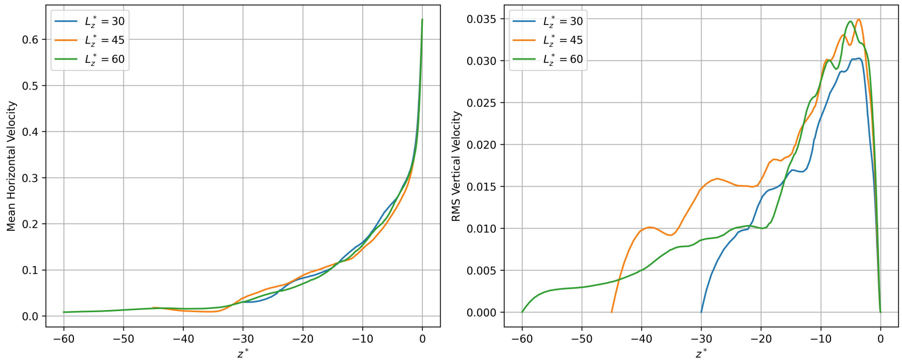

Figure 2.3: Velocity profiles for the case $Re = 500$ and $\theta = 50°$. (Left) The profiles of mean horizontal velocity $\sqrt{(u_x^*)^2 + (u_y^*)^2}$. (Right) The profiles of the root-mean-square of the vertical velocity u_z^* .

periodic. The bottom boundary is stress-free (i.e., no tangential stress) and the normal velocity is zero. We have performed a height test to make sure that the domain height of $30L_\nu$ is large enough to accommodate the boundary layer flow (Figure 2.3). The profiles of mean horizontal velocity $\sqrt{[(u_x^*)^2 + (u_y^*)^2]}$ show no significant difference with larger domain height and the profiles of the root-mean-square of the vertical velocity u_z^* show that the energy is mainly localized in the top region $z^* > -20$. To resolve the boundary layer flow, we use a higher element density near the top boundary. We will explore the parameter space: $Re = [5, 500]$ and $\theta = [0, 90°]$. Simulations for $Re = 700$ are added to extend the Re range. We also simulate the case with $Re = 600$ at $\theta = 0$. The range of Re covers both the laminar and turbulent regimes of the oscillatory Ekman layer.

The simulation always starts from the fluid at rest, where a random perturbation in velocity with a root-mean-square amplitude of about 10^{-2} is imposed. In most cases, the flow will go through a transient state for a certain period and reach a *statistically steady state* (we shall refer to it as a steady state for the sake of brevity in the following sections), which means time-averaged quantities over oscillation period(s) remain constant. The mean values presented below are obtained by taking time averages over oscillation periods. Due to the homogeneity on x- and y-direction, all the values are also averaged on the horizontal plane. The unit of time $t_\oplus$ presented below is $2\pi/\Omega_f$, indicating the period of the oscillating boundary. In what follows, the superscript $(+)$ denotes the quantities non-dimensionalized by the viscous wall scales, velocity u_* and length ν/u_*. The notation is chosen to describe the flow near the boundary.

Table 2.2: Time-averaged quantities obtained from the box model with $Re \leq 700$ and $\theta = 0$, including friction velocity u_* and veering angle β. The time-averaged quantities are obtained from the range $1 \leq t_\oplus \leq 5$, except for the case $Re = 300$ where the range used is $3 \leq t_\oplus \leq 5$.

Re	$\langle u_* \rangle / u_*^{\mathrm{lam}}$	$\langle u_* \rangle / U$	$\langle \beta \rangle$ (degree)
5	1.00 ± 0.00	0.4471 ± 0.0004	45.0 ± 0.1
100	1.00 ± 0.00	0.1000 ± 0.0002	45.0 ± 0.2
200	1.00 ± 0.00	0.0707 ± 0.0002	45.0 ± 0.2
300	1.13 ± 0.02	0.0650 ± 0.0012	29.4 ± 1.5
400	1.21 ± 0.02	0.0606 ± 0.0012	25.6 ± 1.3
500	1.29 ± 0.03	0.0579 ± 0.0011	23.0 ± 1.1
600	1.37 ± 0.03	0.0558 ± 0.0011	21.0 ± 1.3
700	1.43 ± 0.03	0.0541 ± 0.0011	20.1 ± 1.4

2.4 Results

2.4.1 Surface shear stress

The friction velocity u_* is a quantity commonly used to monitor the amplitude of surface shear stress $|\boldsymbol{\tau}|$: $u_* = \sqrt{|\boldsymbol{\tau}|/\rho}$ (e.g. Tennekes et al., 1972). At $\theta = 0$, the laminar solution is $u_*^{\mathrm{lam}} = Re^{-1/2}U$, which serves as the benchmark for low Reynolds number cases. Figure 2.4 shows the ratio u_*/u_*^{lam} as a function of time at $\theta = 0$ for different Re. We see that the friction velocity deviates from its laminar solution when $Re \geq 300$ and the deviation is larger for higher Re. Concerning the case of $Re = 300$, it appears that the deviation from the laminar solution by about 10% can be attributed to turbulence, as supported by the presence of a logarithmic region presented later in this study. We observe that the transient period happens before $t_\oplus = 3$ (before $t_\oplus = 1$ for $Re = 400$ and higher) and the friction velocity reaches a steady value. The result is consistent with the one from Buffett (2021) where the solution at $Re = 500$ is about 20% larger than the laminar value after the onset of turbulence. To obtain the mean value, we take a time average over the interval $1 \leq t_\oplus \leq 5$, except for $Re = 300$ where we use the $3 < t_\oplus < 5$ interval (see Table 2.2). We also calculate the mean values of the veering angle β, which is defined as the argument difference between the boundary velocity vector $u_{\mathrm{B},x} + iu_{\mathrm{B},y}$ and surface shear stress vector $\tau_x + i\tau_y$.

To refine the estimation of the critical Re, we conducted additional simulations for values between $Re = 200$ and 300. Figure 2.5 shows again the time evolution of u_*/u_*^{lam} for the case with $\theta = 0$. On top of the transient oscillations due to the initial conditions, small fluctuations are observed for most cases. The amplitudes of these fluctuations increase with higher Re. At $Re = 290$, u_*/u_*^{lam} does not return to unity but instead reaches a new steady state, indicating that the flow likely becomes turbulent.

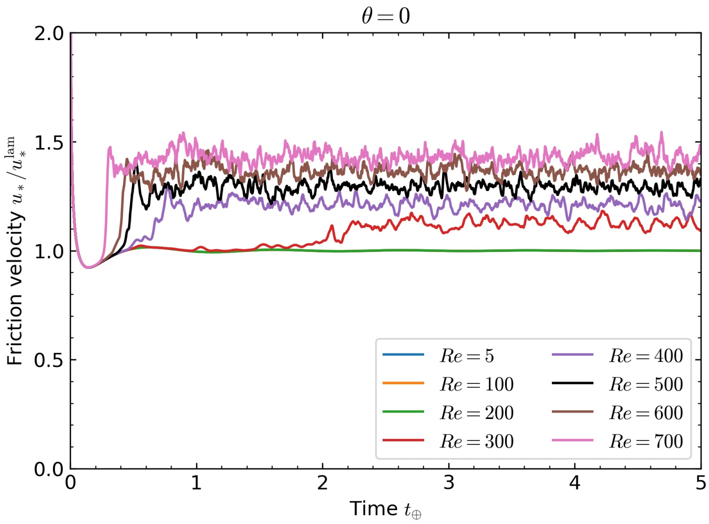

Figure 2.4: Friction velocity ratio u_*/u_*^{lam} as a function of time with different Re at $\theta = 0$. The means deviate appreciably from unity when $Re \geq 300$ and it almost reaches 1.3 when $Re = 500$. The $Re = 5, 100, 200$ curves overlap nearly completely.

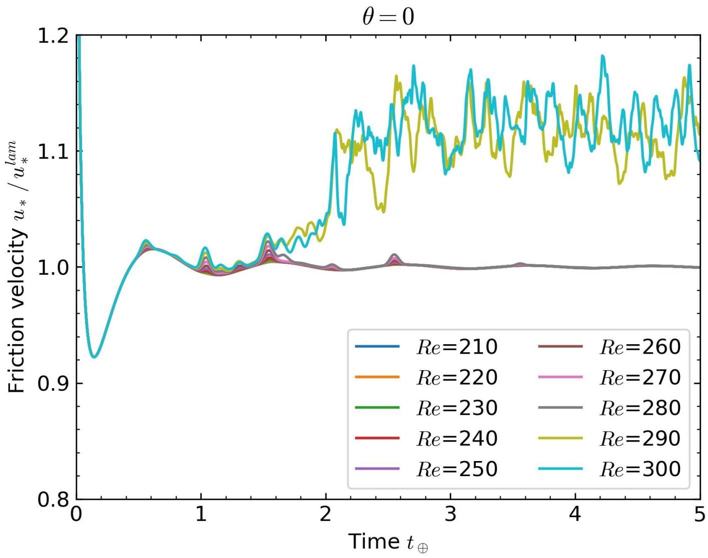

Figure 2.5: Friction velocity ratio u_*/u_*^{lam} as a function of time for the case with $\theta = 0$ and Re between 200 and 300.

2.4.2 Extrapolation to extreme parameters

Scaling laws for turbulent flow have been extensively studied in the literature (Tennekes et al., 1972). The primary goal of these scaling laws is to predict key quantities in extreme parameter regimes that are currently inaccessible through experiments or numerical simulations. Using dimensional analysis, the scaling law for wall-bounded turbulent flow can be derived by separating the flow into two regions. These regions are referred to in the literature as a *surface* layer and an *outer* layer. The surface layer refers to the flow immediately below the bounding surface while the outer layer refers to the region where the flow can be considered as free-streaming. Csanady (1967) applied this approach to derive a scaling law for the turbulent Ekman layer, which was later refined by Spalart (1989) at intermediate Reynolds numbers. In this study, we employ the scaling law—referred to here as the similarity theory—to extrapolate our results to higher Reynolds number regimes. A notable implication of the similarity theory is the emergence of a logarithmic velocity profile in a region between the surface and the outer layers. Consequently, we also examine the velocity profiles to determine whether a logarithmic profile is present.

The similarity theory (Csanady, 1967; Spalart, 1989) establishes a relationship between (u_*, β) and Re of the following form:

$$\frac{U}{u_*}\cos\vartheta + \frac{2}{0.41}\ln\frac{U}{u_*} = \frac{2}{0.41}\ln Re - \frac{1}{0.41}\ln 2 + B \tag{2.8}$$

$$\sin\vartheta = \frac{A}{U/u_*} \tag{2.9}$$

$$\vartheta = \beta + \frac{2C_5}{Re^2}\left(\frac{U}{u_*}\right)^2 \tag{2.10}$$

where 0.41 is known as the von Kármán constant. The constants A, B, and C_5 are to be determined by fitting with either experimental or numerical results. We use our numerical solution from $Re = 300, 400, 500, 600$, and 700 to find the best fit parameters $A = 5.74$ and $B = 1.55$ with $C_5 = -25$ (solid lines in Figures 2.6 and 2.7). The parameters are obtained by performing a least-squares fit. Dashed lines show analytical solutions derived in the laminar regime for comparison. The fitting is good for the friction velocity u_*, but rather inaccurate at $Re \approx 200$ for the veering angle β, indicating that the interpretation of the result at low Reynolds number should be treated with caution.

The dynamics of a steady Ekman layer is a well-studied problem in the literature, and its results have been referenced to provide insights into the oscillatory Ekman layer and, by extension, the boundary layer of precession-driven flow (e.g. Cébron et al., 2019; Buffett, 2021). For comparison, numerical results from the steady Ekman layer studies in the literature are plotted in gray in Figures 2.6 and 2.7. The friction velocity u_* is about 8% larger in the steady case, while the veering angle β appears to reach an asymptotic limit at $Re \geq 10^3$. The experimental result ($\tilde{A} = 3.3, \tilde{B} = 3.0$) presented in Sous et al. (2013) is plotted in blue. Note that the similarity theory used by Sous et al. is equivalent to the reduced version of Equations 2.8 to 2.10 with $C_5 = 0$. The relations to the present convention are given by

$$B = -\frac{\tilde{A}}{0.41} + 5.38 \tag{2.11}$$

and

$$A = \frac{\tilde{B}}{0.41} \tag{2.12}$$

leading to ($A = 7.32, B = -2.67$).

Figure 2.8 shows the horizontal velocity $Q^+ = \sqrt{\overline{u'_x}^2 + \overline{u'_y}^2}/u_*$ at different Reynolds numbers with $\theta = 0$ and $t_\oplus = 5$. The overbar indicates the spatial average on the horizontal plane, and the prime symbol denotes the difference with respect to the boundary velocity, i.e. $u'_i = u_i - u_i(z = 0)$. We adopt this notation in order to compare our results to the law of wall formalism (see Tennekes et al., 1972). According to the formalism, the velocity profile is divided into three parts: a viscous sublayer $Q^+ = |z^+|$, a buffer layer, and an inertial sublayer $Q^+ = (1/0.41)\log|z^+| + 5$. The inertial sublayer is also known as the logarithmic region. The region beyond, where the velocity reaches a constant value, is in the bulk of the fluid. As Figure 2.8 shows, the velocity profiles approach the one predicted by the law of the wall when $Re \geq 300$. A constant slope reveals the presence of a logarithmic region. The inset of Figure 2.8 shows the Kármán measure $\Xi = (|z^+|dQ^+/d|z^+|)^{-1}$ (i.e. reciprocal of the slope) for $Re \geq 300$. A clear logarithmic region develops after $Re \approx 300$. In Figure 2.9, we show the velocity profiles at different time instants for the case $Re = 300$ and find that the appearance of a logarithmic layer coincides with an appreciable deviation of the dissipation from its laminar value, as expected from the presence of turbulence. Besides, the velocity profiles show a maximum above the logarithmic region, which is usually referred to as a *low-level jet* and is also observed for a steady Ekman layer (Deusebio et al., 2014). The fact that the maximum is not well represented in the case of $Re = 700$ implies that the domain height should be increased accordingly if we want to extend the Re range.

2.4.3 Viscous dissipation

Figure 2.10 shows the total kinetic energy, E_{kin}, for $Re = 500$ at different θ. We observe that the total kinetic energies reach a steady state in *most* cases. It implies that the time-averaged change of kinetic energy is zero and the system is in an equilibrium state. According to the energy balance equation (Equation 2.5), we can use the viscous power to approximate the dissipation. Although we can compute the dissipation directly from our model, the reason to use $\mathcal{P}^{\text{visc}}$ is two-fold: (1) it is consistent with the conventional torque approach to compute the dissipation, and (2) we want to apply the turbulence model which is associated with the surface shear stress (i.e. u_*). Figure 2.11 shows the time evolution of the three quantities ($\dot{E}_{\text{int}}$, $\dot{E}_{\text{kin}}$, and $\mathcal{P}^{\text{visc}}$) for the case at $Re = 500$ and $\theta = 0$, verifying the energy balance equation. In Figure 2.10, a longer transient period is observed at $\theta = 50°$, but the flow eventually reaches a steady state. At $\theta = 60°$, we see the E_{kin} increases without reaching saturation

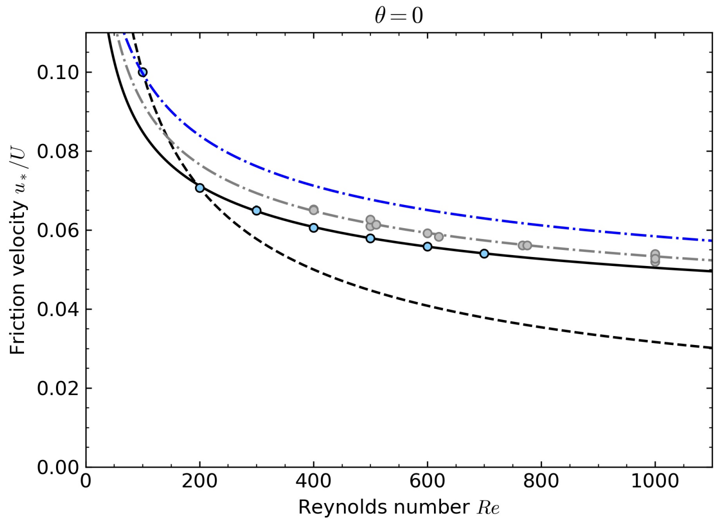

Figure 2.6: Friction velocity u_*/U as a function of Reynolds number Re. Light blue circles: numerical solution; black line: best fit with $A = 5.74$, $B = 1.55$, and $C_5 = -25$; dashed line: laminar solution; blue dash-dotted line: $A = 7.32$ and $B = -2.68$ (Sous et al., 2013). Grey circles are numerical results for the steady Ekman layer (Spalart, 1989; Coleman et al., 1990; Coleman, 1999; Shingai & Kawamura, 2004; Marlatt et al., 2012; Braun et al., 2020); grey dash-dotted line is the corresponding best fit with $A = 5.40$, $B = 0.26$, and $C_5 = -52$.

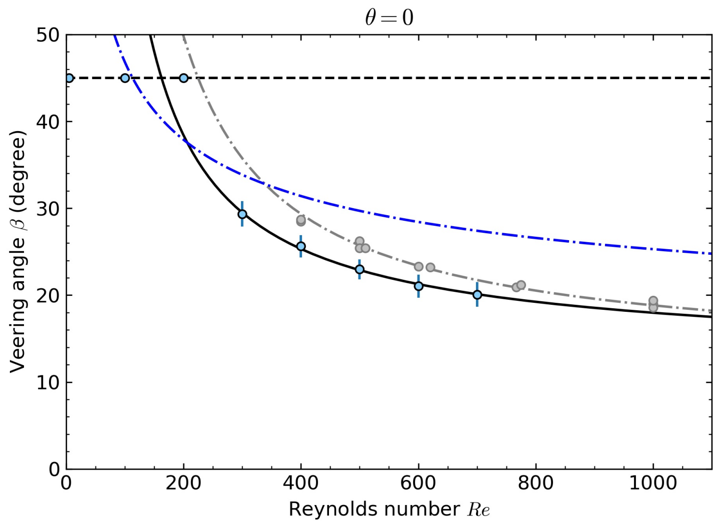

Figure 2.7: Following Figure 2.6. The veering angle β between surface shear stress and boundary velocity seems to reach an asymptotic limit when $Re \geq 10^3$.

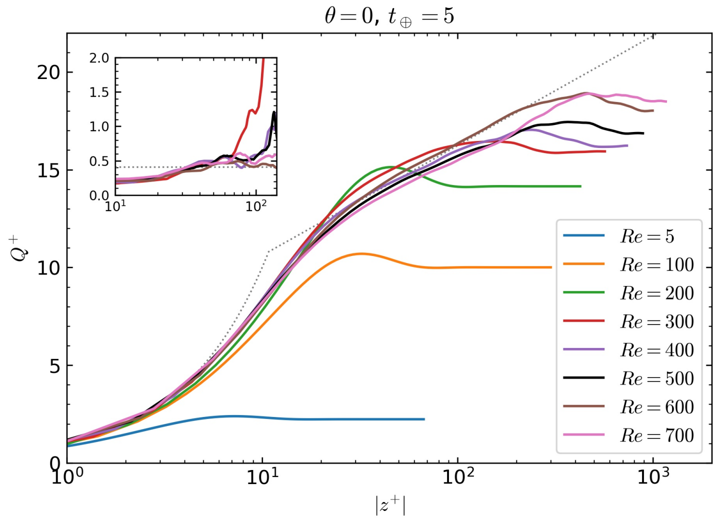

Figure 2.8: Mean horizontal velocity $Q^+ = \sqrt{\overline{u_x'}^2 + \overline{u_y'}^2}/u_*$ at different Reynolds numbers with $\theta = 0$ and $t_\oplus = 5$. Dotted line: $Q^+ = |z^+|$ for $|z^+| \leq 10$ and $Q^+ = (1/0.41)\log|z^+| + 5$ for $|z^+| > 10$. (Inset) Kármán measure $\Xi = (|z^+|dQ^+/d|z^+|)^{-1}$ for $Re \geq 300$. Dashed line: $\Xi = 0.41$. X-axis is $|z^+|$ and y-axis is Ξ.

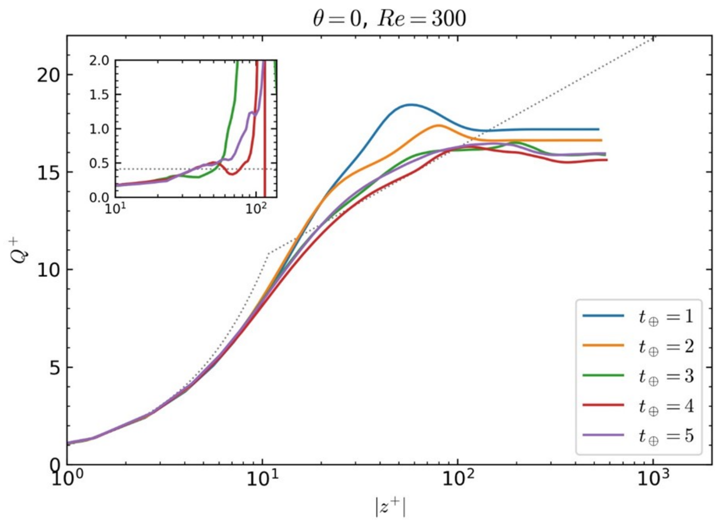

Figure 2.9: Mean horizontal velocity Q^+ at different times $t_\oplus$ with $\theta = 0$ and $Re = 300$. The profile at $t_\oplus = 4$ shows a closer resemblance to the law of the wall, compared to the profiles at $t_\oplus = 3$ and 5.

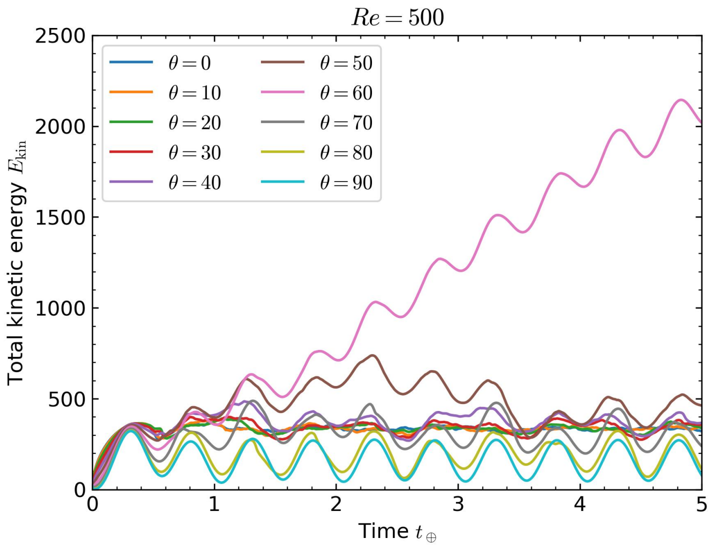

Figure 2.10: Total kinetic energy $E_{\rm kin}$ with different θ at $Re = 500$. Most cases reach a steady state within $t_\oplus = 5$, while a long-period modulation is observed for $\theta = 50°$ and an indefinite increase for $\theta = 60°$.

within the default simulation time $t_\oplus = 5$. This phenomenon is directly related to the well-known anomalous behaviour of the Ekman boundary layer thickness at the so-called *critical latitude*, which is in our case at $\theta = 60°$ (e.g. see Section 8.07.1.4 in Tilgner, 2015). This is also observed in a laboratory experiment where a large circular rotating tank with angular velocity Ω_0 is subjected to a period forcing by an oscillating plate, constituting the evidence of Ekman layer resonance, i.e. the forcing frequency matches the inertial wave frequency given by Ω_0 (Vincze et al., 2019).

Figure 2.12 and Figure 2.13 show the viscous power per unit area $\mathcal{P}^{\rm visc}$ for the cases $\theta = 50°$ and $60°$ with longer simulation time. Time-averaged values over 4 oscillation periods are plotted in dots. The orange dot indicates the value obtained in the default range, $1 \leq t_\oplus \leq 5$. As can be seen, for $\theta = 50°$, the power reaches a steady value within $t_\oplus \leq 5$, suggesting that $t_\oplus = 5$ is sufficient for most cases. On the other hand, $\theta = 60°$ requires a longer transient before reaching a steady value which approximates the laminar solution. This finding suggests that we should replace the value obtained in the default range with its laminar solution when computing the total dissipation.

Figure 2.14 shows the viscous power per unit area $\left\langle \mathcal{P}^{\rm visc^*} \right\rangle$ at each co-latitude θ, which we compute by taking a time-average in default range, $1 \leq t_\oplus \leq 5$, except for the case $Re = 300$. Note that we multiply the power by Re to remove the viscosity dependence and to see the effect of turbulence. As it can be seen, when $Re \geq 300$, the power increases at almost every θ compared to the laminar solution, while the models with $Re \leq 200$ remain close to the laminar solution. Given $Re \geq 300$, the increments are not the

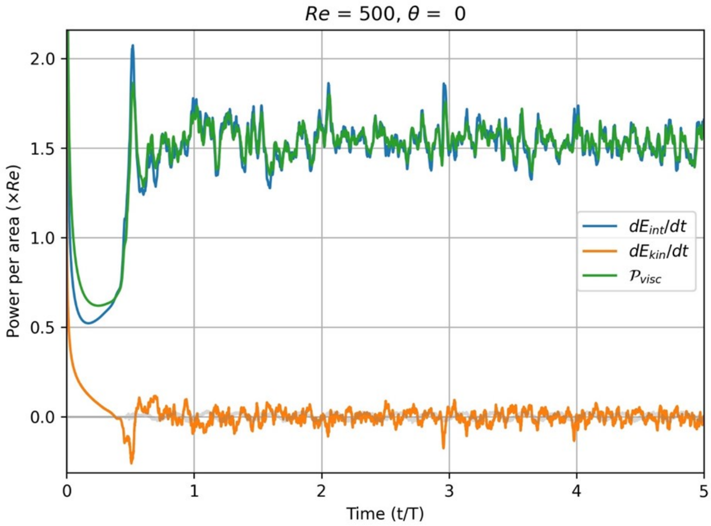

Figure 2.11: Temporal evolution of the energy-related terms at $Re = 500$ and $\theta = 0$: change rate of internal energy dE_{int}/dt (blue), change rate of kinetic energy dE_{kin}/dt (orange), and viscous power $\mathcal{P}^{visc}$ (green). The change rate of the kinetic energy is close to zero and the rest two almost overlap. The time-averaged values over the interval $1 < t_{\oplus} < 5$ are 1.540 for dE_{int}/dt, -0.002 for dE_{kin}/dt, and 1.542 for $\mathcal{P}^{visc}$.

same across θ. No increment is observed at the equator and barely present near the critical latitude. The small increment at the critical latitude is the consequence of insufficient simulation time; the power will eventually reach the laminar solution, given a long enough simulation time. This latitude variation can be attributed to the orientation of the rotation vector of the fluid, which goes from perpendicular to the flow at the pole to parallel at the equator. When parallel, there is no Coriolis force and the Ekman boundary layer flow will reduce to the well-studied Stokes type, whose critical Reynolds number for fully turbulent regime $Re = 2500$ (see e.g. Ozdemir et al., 2014) is higher than the present setting.

Figure 2.15 shows the total global dissipation $\mathcal{D}_\nu$ in the boundary layer at different Re. We obtain a global value by integrating the contributions from each numerical simulation at different θ, using the trapezoidal rule. Since the dissipation is symmetrical along the azimuthal direction and with respect to the equator, we only need to integrate over the range $0 \leq \theta \leq 90°$. Since E_{kin} remains steady for most cases, the viscous power from surface shear stress will be equal but with the opposite sign to the internal dissipation. Concerning the diverging case at the critical latitude, we replace the value with its laminar solution to avoid overestimation[1]. Therefore, we integrate $-\mathcal{P}^{\mathrm{visc}}$ over the spherical surface to obtain $\mathcal{D}_\nu$. To see the effect of turbulence, we normalize

[1]If we manually assign the analytical value to the viscous power at $\theta = 60°$, then the dissipation will reduce up to 6%, depending on Re.

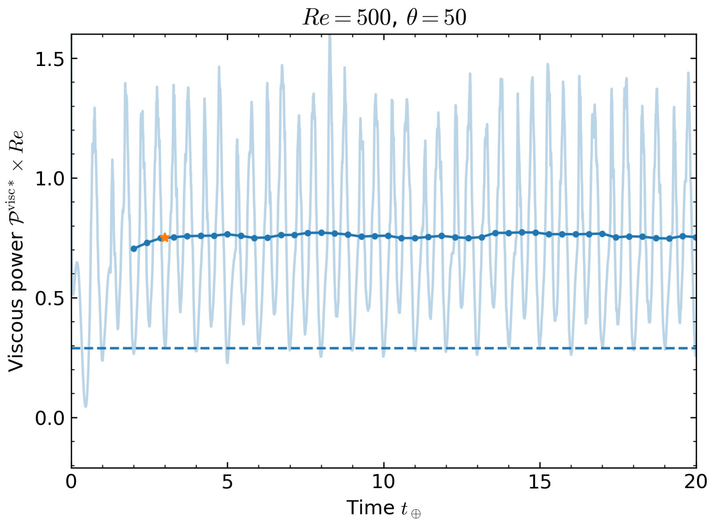

Figure 2.12: Viscous power per unit area $\mathcal{P}^{\mathrm{visc}}$ (light blue curve) for the cases $\theta = 50°$ with longer simulation time. Blue dot: time-averaged value over 4 oscillation periods. Orange dot: value obtained in the default range $1 \leq t_\oplus \leq 5$. The default range is sufficient to obtain a steady value. The dashed line shows the laminar solution.

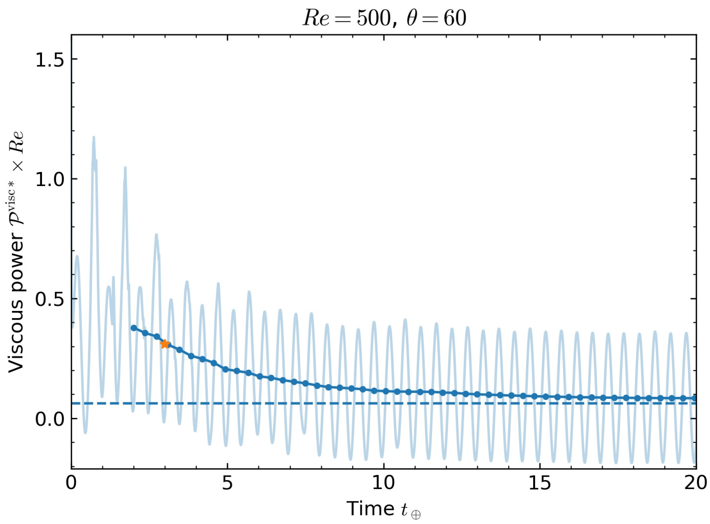

Figure 2.13: Same as Figure 2.12 but for $\theta = 60°$. Simulation runs longer than the default range are required for the viscous power to reach a steady value, which seems to approach the laminar solution.

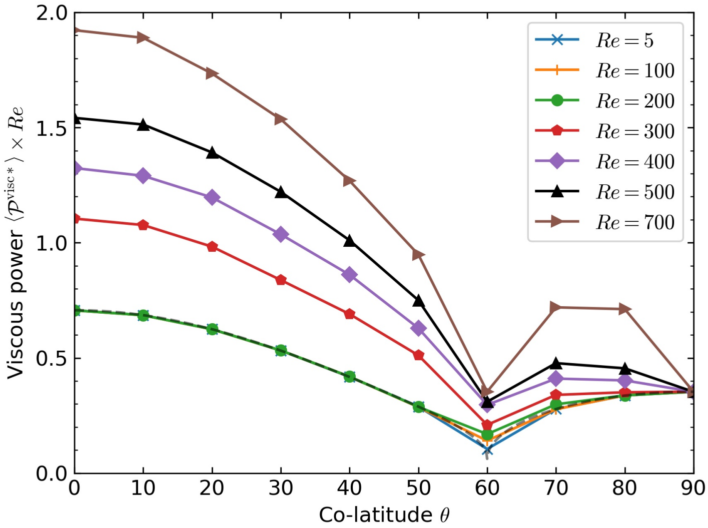

Figure 2.14: Time-averaged viscous power per unit area $\left\langle \mathcal{P}^{\mathrm{visc}^*} \right\rangle$ multiplied by Re at different co-latitudes θ (degree). The gray dash line is computed via $\mathcal{P}^{\mathrm{visc}} = \boldsymbol{\tau} \cdot \boldsymbol{u}$, where $\boldsymbol{\tau}$ and $\boldsymbol{u}$ are given by the solutions obtained in the laminar regime where the non-linear term is neglected – corresponding to the cases of small Re .

the numerical solution with the laminar solution $\mathcal{D}_\nu^{lam}$, so it should be very close to unity in the laminar regime if our numerical approach is valid. The values of $\mathcal{D}_\nu / \mathcal{D}_\nu^{lam}$ are listed in Table 2.3. As can be seen at $Re = 5$, the difference to the laminar solution due to limited co-latitudes is about -4%, which is associated with the limited number of co-latitudes used[2]. The dissipation deviates from the laminar solution when $Re \geq 300$. A similar behaviour was also observed in the global model by Cébron et al. (2019), where dissipation is found to be mainly confined to the boundary layer.

Next, we plot the dissipation predicted by the turbulence model $\mathcal{D}_\nu^{\mathrm{turb}}$ (Equation 2.7) in a dashed line (Figure 2.15). It can be seen that the prediction overestimates the dissipation when $Re \geq 300$. Since the turbulence model assumes the parameter k at different θ's are the same as the one at the pole, this overestimation is possibly related to the fact that the actual dissipation has latitudinal dependence, as shown in Figure 2.14. Even from the limited Re range given in this study, latitudinal variation in the turbulence effect is evident, thus raising the concern for the reliability of the turbulence model based on k which is typically treated as a constant in the literature. To accommodate the discrepancy, we introduce a new parameter χ and rewrite the turbulent dissipation as

$$\mathcal{D}_\nu^{\mathrm{turb}} = -2.62\sqrt{2}\chi k I \Delta\Omega^3. \tag{2.13}$$

[2]The downward concavity of the $\mathcal{P}^{\mathrm{visc}}$ implies that the integration, based on trapezoidal rule, will underestimate the dissipation.

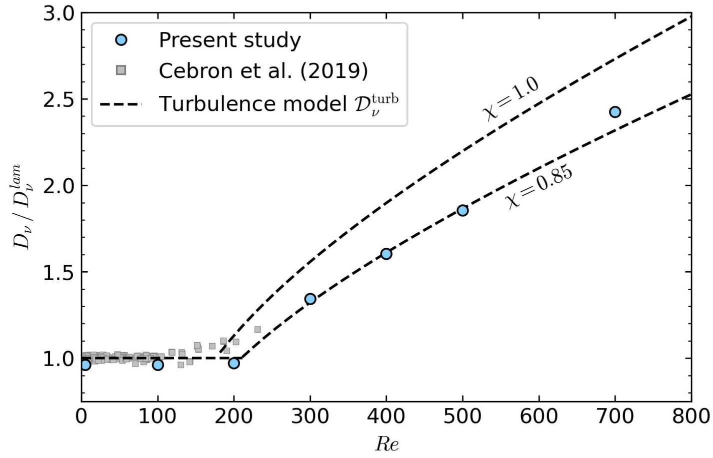

Figure 2.15: Boundary layer dissipation $\mathcal{D}_\nu$ as a function of Re. The dissipation is normalized by its laminar solution $\mathcal{D}_\nu^{\rm lam}$. Blue circle: present study; gray square: Cébron et al. (2019). Dashed line: turbulence model $\mathcal{D}_\nu^{\rm turb}$ with $\chi = 1.0$ and $\chi = 0.85$.

Table 2.3: Normalized viscous dissipation $\mathcal{D}_\nu/\mathcal{D}_\nu^{\rm lam}$ obtained from the box model.

Re	$\mathcal{D}_\nu/\mathcal{D}_\nu^{\rm lam}$
5	0.96
100	0.96
200	0.97
300	1.34
400	1.61
500	1.86
700	2.42

We find that $\chi = 0.85$ marks the lower bound for the results obtained in this study. The dissipation obtained at $Re = 300, 400, 500$ falls on the curve of $\chi = 0.85$. The excess dissipation at $Re = 700$ shows a hint of increasing dissipation when Re is even larger.

2.5 Discussion and conclusions

We have derived the governing equation for the boundary layer generated by the precession-driven flow in a spherical cavity, using a local Cartesian coordinate system. Both the order of magnitude estimation and the numerical solution suggest that the Poincaré term is negligible in the boundary layer if precession is weak. In order to solve the governing equation numerically, we constructed a local Cartesian box model to simulate the boundary layer flow. In the laminar regime, we found that the total energy dissipation, which is computed from the local contributions obtained from the individual box models, is consistent with the laminar value from previous studies based on a global model (e.g. Cébron et al., 2019). In the turbulent regime, we have found that (1) the flow at certain latitudes (i.e. $\theta = 60°$ and $90°$) may remain laminar, and (2) the total energy dissipation deviates appreciably from the laminar value, by a factor of 1.86. For the flow at the pole, $\theta = 0$, the energy dissipation begins to deviate from the analytical laminar expectation when $Re \geq 300$, and the flow exhibits turbulent characteristics, such as a logarithmic layer region, allowing us to use an asymptotic similarity formalism. Using this, we have computed the asymptotic curves for both u_* and β as a function of Re, which can be used to compute the total energy dissipation in the turbulent regime via turbulence models.

In the conventional turbulence model, the total turbulent dissipation is given as $-(45\pi/32)kI\Delta\Omega^3$, where the parameter k is supposed to quantify the asymptotic behavior of the local dissipation in the turbulent regime at high Re. Note that the derivation of the model implicitly assumes that k is independent of latitude. Following the same approach as Cébron et al. (2019) to estimate k via $k = (u_*/U)^2 \cos\beta$, we have found that both (u_*/U) and β at high Re can be computed from the best fit asymptotic curve obtained at $\theta = 0$. In order to recover the laminar solution (Equation 2.6) when Re goes into the laminar regime, we propose a turbulence model by writing the total dissipation as Equation 2.7. The overestimation of the turbulence model, compared to the value obtained from the numerical solution, suggests that the assumption on k may be inappropriate. At least for the case $Re = 500$, our numerical solution shows that the flow is not even turbulent at certain latitudes, such as the critical latitude or the equator. A thorough investigation of the latitudinal variation on k combined with an investigation of the flow asymptotic behaviour at each latitude would help establish a more reliable turbulence model. That aside, the uncertainty of the turbulence model given by Equation 2.7 is about 15% in the $Re \leq 700$ range.

The previous study by Deusebio et al. (2014) shows that the asymptotic theory applied to the intermediate Re range ($400 < Re < 775$), where a logarithmic layer is observed, is sufficient to get a good prediction of u_* and β at high Re ($= 1600$). We adopt the theory for an oscillatory Ekman layer at $\theta = 0$ not only because we see the logarithmic layer in the flow but also because the theory should be generally unaffected by imposing a time-varying boundary velocity. The theory developed by Csanady (1967) and Spalart (1989) is based on the assumption that there exists an overlapping region where the velocity profiles in both the inner layer (i.e. the viscous sublayer) and the outer layer (i.e. the free-stream region) match, a fact unaffected by imposing time dependence.

Application of our results to the Earth's core is possible in principle since they are based on the reduced form of the governing equation (Equation 2.4), which is identical to the one derived for a spheroidal cavity like Earth by Buffett (2021). We are able to reach the Earth's parameter regime with the local Cartesian box model, so we don't need to make extrapolations using a turbulence model. Our numerical result shows that the total energy dissipation in the turbulent regime at $Re = 500$ is 1.86 times of the laminar value. If the damping of FCN shares the same increasing factor, then the effective viscosity will increase by a factor of 3.5, which is still far below the required amount (six orders of magnitude higher) inferred from the observation. It implies that the electromagnetic coupling may play a significant role in closing the gap.

An accurate calculation of the energy dissipation at the CMB in the Moon is unfeasible since we lack a proper turbulence model, but also because interior models obtained from seismic and gravity measurements are poorly constrained. There are three relevant parameters: (1) the angle between the rotation axes of the core and the mantle, (2) the lunar core radius, and (3) the moment of inertia of the fluid core. There is no direct measurement for the orientation of the core rotation axis. According to the dynamic argument that the lunar CMB flattening is smaller than its Poincaré number, the core is unlikely to share the precession of the mantle (Goldreich, 1967); the core rotation axis should be thus closely aligned with the ecliptic normal. We use the reduced model of Cébron et al. (2019) to compute the orientation of $\boldsymbol{\Omega}_f$. The plausible range of core radius obtained from gravity measurements is $200 - 380\,\mathrm{km}$ (Williams et al., 2014; Viswanathan et al., 2019). If we take the core radius as 380 km, then the relative velocity at CMB will be around $2.72 \times 10^{-2}\,\mathrm{m\,s^{-1}}$ and the Reynolds number will be 1.67×10^4. We obtain the moment of inertia of the fluid core by taking the moment ratio $C_f/C = 7 \times 10^{-4}$ (Williams et al., 2014). With our best fit parameters (A, B, C_5) and the reduced turbulence model (Equation 2.13), we obtain $D_\nu^{\mathrm{turb}} = 72$ or 84 MW for $\chi = 0.85$ or 1.0, respectively. For a smaller core, say $Re = 200\,\mathrm{km}$ with the same moment ratio, the Reynolds number reduces to 8.79×10^3 while the dissipation increases by about 10%. For comparison, we also compute the dissipation with the parameters $(A = 7.32, B = -2.67)$ (Sous et al., 2013) and the conventional turbulence model, $-(45\pi/32)kI\Delta\Omega^3$; the obtained value is 126 MW, about 60% larger than our result. According to the analysis of lunar laser ranging (LLR) data, the dissipation at CMB is about 58 MW (Williams et al., 2001), 84 MW (Williams et al., 2014), and 73 MW (Williams & Boggs, 2015), respectively. Concerning the uncertainty of the interior model, it is still insufficient to say if our model matches the observation or not, but at least we provide a set of parameters with numerical support, which can be used for the turbulence model. A sensitivity test on the parameters (A, B, C_5) shows that (1) β is sensitive to A and also sensitive to C_5 when $Re < 10^3$, and (2) the sensitivity of u_*/U to both A and B decreases as Re increases (see Figures 2.16 to 2.18).

The implication for planetary cores with turbulent boundary layers should be interpreted with care. In this study, the quoted Re for the Earth and the Moon is obtained based on the laminar solution (e.g. Busse, 1968; Cébron et al., 2019), where the boundary layer is treated in the laminar regime. However, the obtained Re exceeds the critical value, suggesting that the boundary layer is no longer laminar. For the Earth, the conclusion that the turbulence effect is unlikely to account for the observed FCN damping remains as the Earth is at the margin of turbulence. For the Moon, our purpose is to demonstrate a way to forward compute the dissipation, and a more comprehensive model is needed for future exploration.

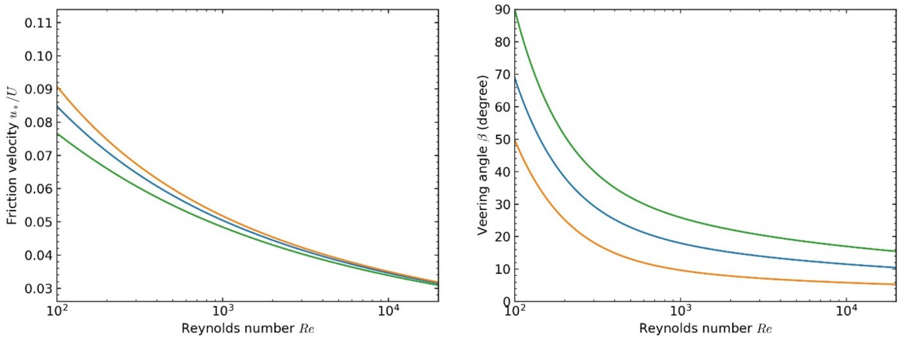

Figure 2.16: Sensitivity test on A. The reference parameters are ($A = 5.74, B = 1.55, C_5 = -25$). Blue: $A = 5.74$; orange: $A = 2.87\,(-50\%)$; green: $A = 8.61\,(+50\%)$.

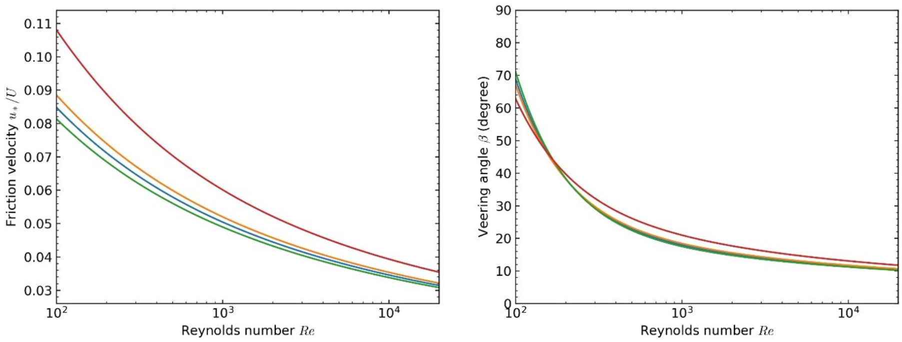

Figure 2.17: Sensitivity test on B. The reference parameters are ($A = 5.74, B = 1.55, C_5 = -25$). Blue: $B = 1.55$; orange: $B = 0.78\,(-50\%)$; green: $B = 2.33\,(+50\%)$; red: $B = -2.67$.

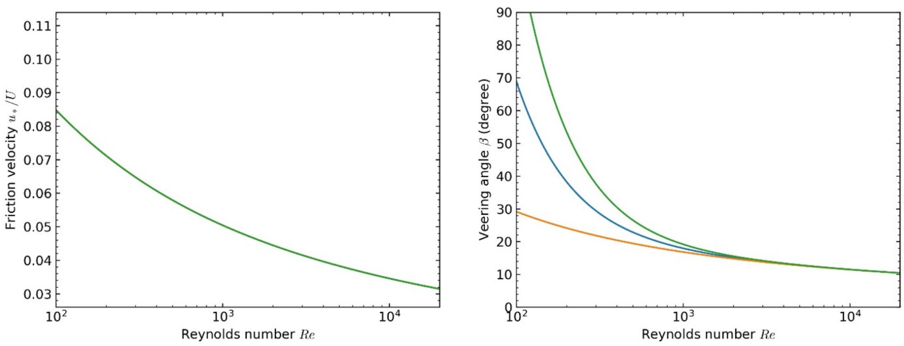

Figure 2.18: Sensitivity test on C_5. The reference parameters are ($A = 5.74, B = 1.55, C_5 = -25$). Blue: $C_5 = -25$; orange: $C_5 = 0$; green: $C_5 = -52$.

We aim to demonstrate that through appropriate formulation, it is feasible to complement the results from global models. By narrowing our focus to the boundary layer exclusively, we can expand the parameter range and explore the turbulent regime. Potential applications of this approach include spin-up, libration, and precessing cylinders (Pizzi et al., 2021).

Appendix 2.A: Transformation between reference frames and coordinate systems

The solution of $\boldsymbol{\Omega}_f$ from Cébron et al. (2019) is given in precessing frame where the coordinate system $(\hat{\boldsymbol{X}}_p^{'}, \hat{\boldsymbol{Y}}_p^{'}, \hat{\boldsymbol{Z}}_p^{'})$ is defined such that $\hat{\boldsymbol{Z}}_p^{'}$ is aligned with $\boldsymbol{\Omega}_m$ and $\boldsymbol{\Omega}_p$ is on the $\hat{\boldsymbol{X}}_p^{'}$-$\hat{\boldsymbol{Z}}_p^{'}$ plane with the co-latitude α (Figure 2.19). We use (θ_f, ϕ_f) to denote the orientation of the fluid rotation vector. Since the global coordinate system $(\hat{\boldsymbol{X}}, \hat{\boldsymbol{Y}}, \hat{\boldsymbol{Z}})$ defined in the present study has two features: $\hat{\boldsymbol{Z}}$ is aligned with $\boldsymbol{\Omega}_f$ and it is defined in the fluid frame, we need a series of transformation to adopt the solution in the present study. First, we implement a two-step rotation: (1) rotation about $\hat{\boldsymbol{Z}}_p^{'}$ in counterclockwise direction by ϕ_f, and (2) rotation about the intermediate axis $\hat{\boldsymbol{Y}}_p^{''}$ in counterclockwise direction by θ_f (see e.g. Thornton & Marion, 2003). The transformation matrices are

$$\lambda_1 = \begin{pmatrix} \cos\phi_f & \sin\phi_f & 0 \\ -\sin\phi_f & \cos\phi_f & 0 \\ 0 & 0 & 1 \end{pmatrix} \tag{2.14}$$

and

$$\lambda_2 = \begin{pmatrix} \cos\theta_f & 0 & -\sin\theta_f \\ 0 & 1 & 0 \\ \sin\theta_f & 0 & \cos\theta_f \end{pmatrix} \tag{2.15}$$

Coordinate of a vector $\boldsymbol{x}$ in the new coordinate system $(\hat{\boldsymbol{X}}_p, \hat{\boldsymbol{Y}}_p, \hat{\boldsymbol{Z}}_p)$ is given by $[\boldsymbol{x}]_p = \lambda_2\lambda_1[\boldsymbol{x}]_p'$. The rotations are chosen so that $\boldsymbol{\Omega}_m$ is on the $\hat{\boldsymbol{X}}_p$-$\hat{\boldsymbol{Z}}_p$ plane and leaning toward negative $\hat{\boldsymbol{X}}_p$ with co-latitude θ_f, which gives the boundary conditions consistent with the ones mentioned in the main text. Second, a transformation from the precessing frame to the fluid frame is given by (e.g. Noir & Cébron, 2013)

$$\lambda_3 = \begin{pmatrix} \cos\Omega_f t & \sin\Omega_f t & 0 \\ -\sin\Omega_f t & \cos\Omega_f t & 0 \\ 0 & 0 & 1 \end{pmatrix} \tag{2.16}$$

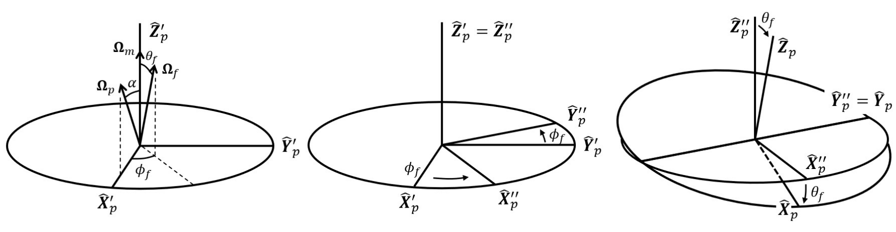

Figure 2.19: Schematic diagram for the associated vectors and transformations. (Left) The angle between $\boldsymbol{\Omega}_m$ and $\boldsymbol{\Omega}_p$ is α. The co-latitude and longitude of $\boldsymbol{\Omega}_f$ are θ_f and ϕ_f, respectively. Note that the magnitudes and orientations of $\boldsymbol{\Omega}_m$, $\boldsymbol{\Omega}_p$, and $\boldsymbol{\Omega}_f$ are not to scale. (Middle) Counterclockwise rotation through ϕ_f about $\hat{\boldsymbol{Z}}_p^{'}$. (Right) Counterclockwise rotation through θ_f about $\hat{\boldsymbol{Y}}_p^{''}$.

Finally, in order to solve the governing equations in local coordinate system, one further transformation is needed, which is given by

$$\begin{cases} \hat{\boldsymbol{X}} = \sin\theta\cos\phi\,\hat{\boldsymbol{r}} + \cos\theta\cos\phi\,\hat{\boldsymbol{\theta}} - \sin\phi\,\hat{\boldsymbol{\phi}} \\ \hat{\boldsymbol{Y}} = \sin\theta\sin\phi\,\hat{\boldsymbol{r}} + \cos\theta\sin\phi\,\hat{\boldsymbol{\theta}} + \cos\phi\,\hat{\boldsymbol{\phi}} \\ \hat{\boldsymbol{Z}} = \cos\theta\,\hat{\boldsymbol{r}} - \sin\theta\,\hat{\boldsymbol{\theta}} \end{cases} \tag{2.17}$$

where $\hat{\boldsymbol{r}} = \hat{\boldsymbol{z}}$, $\hat{\boldsymbol{\theta}} = -\hat{\boldsymbol{y}}$, and $\hat{\boldsymbol{\phi}} = \hat{\boldsymbol{x}}$ (see Figure 2.1). For example, the coordinates of the fluid rotation vector $\boldsymbol{\Omega}_f$, which in the $(\hat{\boldsymbol{X}}_p^{'}, \hat{\boldsymbol{Y}}_p^{'}, \hat{\boldsymbol{Z}}_p^{'})$ system is given by $\Omega_f(\sin\theta_f\cos\phi_f, \sin\theta_f\sin\phi_f, \cos\theta_f)$, in the local coordinate system $(\hat{\boldsymbol{x}}, \hat{\boldsymbol{y}}, \hat{\boldsymbol{z}})$ are $(0, \Omega_f\sin\theta, \Omega_f\cos\theta)$. The coordinates of $\boldsymbol{\Omega}_p$ and $\hat{\boldsymbol{R}}\times(\hat{\boldsymbol{k}}_p\times\hat{\boldsymbol{k}}_f)$ are computed in the same way.

Appendix 2.B: Analytical solution

We solve analytically Equation 2.4 in its dimensional form together with the continuity equation:

$$\frac{\partial \boldsymbol{u}}{\partial t} + \boldsymbol{u}\cdot\nabla\boldsymbol{u} = -\frac{1}{\rho}\nabla P + \nu\nabla^2\boldsymbol{u} - 2\boldsymbol{\Omega}_f\times\boldsymbol{u}, \tag{2.18}$$

$$\nabla\cdot\boldsymbol{u} = 0 \tag{2.19}$$

where $\boldsymbol{\Omega}_f = \Omega_f\hat{\boldsymbol{k}}_f$ is the fluid rotation vector and P is the reduced pressure including the centrifugal force. In the local coordinate system, the vector $\hat{\boldsymbol{k}}_f$ is given by $\cos\theta\,\hat{\boldsymbol{z}} + \sin\theta\,\hat{\boldsymbol{y}}$, where θ is the co-latitude. Following Equation 2.3, the boundary conditions require $\boldsymbol{u} = 0$ at $z = -\infty$; at $z = 0$, the velocities are $u_x = U\cos\theta\cos(\Omega_f t + \phi)$, $u_y = -U\sin(\Omega_f t + \phi)$, and $u_z = 0$, where U is the relative velocity of the mantle and ϕ is the longitude. We have to note that the governing equations generally imply a simple rotating fluid with angular velocity $\boldsymbol{\Omega}_f$, this due to the fact that the Poincaré term is neglected in the boundary layer of the precession-driven flow. Yet, precession enters the formulation through the boundary conditions. Nevertheless the following formulation, borrowed from the classic Ekman layer analysis, serves not only to demonstrate the flow but also to validate the result against known solutions in the literature.

Analytical solutions are available to validate our numerical results in the laminar regime. Equation 2.18 can be solved analytically by making some assumptions. First, we assume the system is horizontally uniform, so that the solution must be independent of x and y. From the continuity equation $\nabla\cdot\boldsymbol{u} = 0$, we further have $\partial u_z/\partial z = 0$. Given that no vertical motion is allowed on the top boundary, we end up with $u_z = 0$ everywhere. Equation 2.18 then becomes

$$\frac{\partial u_x}{\partial t} - 2\Omega_f\cos\theta\,u_y = -\frac{1}{\rho}\frac{\partial P}{\partial x} + \nu\frac{\partial^2 u_x}{\partial z^2} \tag{2.20}$$

$$\frac{\partial u_y}{\partial t} + 2\Omega_f\cos\theta\,u_x = -\frac{1}{\rho}\frac{\partial P}{\partial y} + \nu\frac{\partial^2 u_y}{\partial z^2} \tag{2.21}$$

$$2\Omega_f \sin\theta\, u_x = -\frac{1}{\rho}\frac{\partial P}{\partial z} \tag{2.22}$$

At infinity, given $u_x = u_y = 0$, the horizontal pressure gradient should be zero: $\partial P/\partial x = \partial P/\partial y = 0$. Since u_x is independent of x and y, derivative of Equation 2.22 shows that the horizontal pressure gradient is invariant of height. That means the horizontal pressure gradients are not involved in the horizontal force balance.

From the boundary conditions, we assume that the solutions for the oscillatory Ekman layer are in the form

$$u_x = \mathfrak{Re}\left[e^{i(\Omega_f t+\phi)} q_x(z)\right] \tag{2.23}$$

$$u_y = \mathfrak{Re}\left[e^{i(\Omega_f t+\phi)-\frac{i\pi}{2}} q_y(z)\right] \tag{2.24}$$

$$u_z = 0 \tag{2.25}$$

where $q_x(z)$ and $q_y(z)$ are the functions to be solved. Substituting the solutions into Equations 2.20-2.22 and solving for the $q_i(z)$, we end up with

$$q_{x(z)} = C_1 e^{\sigma_+ z} + C_2 e^{\sigma_- z} \tag{2.26}$$

$$q_y(z) = C_1 e^{\sigma_+ z} - C_2 e^{\sigma_- z} \tag{2.27}$$

where $C_1 = U(\cos\theta - 1)/2$, $C_2 = U(\cos\theta + 1)/2$, and $\sigma_\pm = \sqrt{\Omega_f/\nu}\sqrt{(1 \pm 2\cos\theta)i}$. Notice that the sign of the term $(1 \pm 2\cos\theta)$ changes at $\theta = 60°$ and $120°$, so we cannot simply expand $\sigma_\pm$ at this stage. The above expression is easy to implement for numerical computation. To get the physical picture, we expand the solution at the three representative co-latitudes: $\theta = 0$, $90°$, and $60°$. At the north pole ($\theta = 0$), the solution reads

$$u_x = U e^{\frac{z}{\sqrt{2}L_v}} \cos\left(\Omega_f t + \phi - \frac{z}{\sqrt{2}L_v}\right) \tag{2.28}$$

$$u_y = -U e^{\frac{z}{\sqrt{2}L_v}} \sin\left(\Omega_f t + \phi - \frac{z}{\sqrt{2}L_v}\right) \tag{2.29}$$

where $L_\nu = \sqrt{\nu/\Omega_f}$ is the thickness of steady Ekman layer. Given t_0 and ϕ_0, the solution shows an Ekman spiral, which decays exponentially to the depth. On top of that, the spiral is rotating in clockwise direction. At the equator ($\theta = 90°$), the boundary drives the fluid in the direction parallel to the rotation vector: there is no Coriolis force acting on the flow. The type of the boundary flow then reduces to the Stokes boundary layer (e.g. Landau & Lifshitz, 1987):

$$u_x = 0 \tag{2.30}$$

$$u_y = -U e^{\frac{z}{\sqrt{2}L_v}} \sin\left(\Omega_f t + \phi - \frac{z}{\sqrt{2}L_v}\right) \tag{2.31}$$

The depth of penatration is usually defined as $\sqrt{2\nu/\Omega_f} = \sqrt{2}L_\nu$. At critical latitudes where one of $\sigma_\pm$ becomes zero, the velocity profile shows a non-decaying component; here is the case of $\theta = 60°$

$$u_x = U\left[\frac{-1}{4}e^{\frac{z}{L_\nu}}\cos\left(\Omega_f t + \frac{z}{L_v}\right) + \frac{3}{4}\cos\Omega_f t\right] \tag{2.32}$$

$$u_y = U\left[\frac{-1}{4}e^{\frac{z}{L_\nu}}\sin\left(\Omega_f t + \frac{z}{L_v}\right) - \frac{3}{4}\sin\Omega_f t\right] \tag{2.33}$$

That means the flow will penetrate all the way down into the bulk of the fluid and the boundary layer has infinite thickness, which is against the very first assumption of horizontal uniformity – the vertical gradient in velocity is relatively larger than the horizontal ones in the thin boundary layer. This breakdown in the local approximation, already pointed by Bondi and Lyttleton (1953), was shown numerically to spawn internal shear layers which has negligible contribution to the total dissipation (Hollerbach & Kerswell, 1995).

The shear stress can be computed directly from the velocity. The viscous stress tensor is given by $s_{ik} = \mu(\partial_i u_k + \partial_k u_i)$, where μ is the dynamic viscosity (note $\nu = \mu/\rho$ is the kinematic viscosity) (see e.g. Equations 15.2 and 15.8 in Landau & Lifshitz, 1987). On the top boundary $z = 0$, given the normal vector $\hat{\boldsymbol{n}} = \hat{\boldsymbol{z}}$, the surface shear stress exerted on the fluid is $\tau_i = s_{ij}n_j$, i.e., $\tau_x = \mu\partial_z u_x$ and $\tau_y = \mu\partial_z u_y$:

$$\tau_x = \mathfrak{Re}\left[\mu e^{i(\Omega_f t+\phi)}\left(\sigma_+ C_1 + \sigma_- C_2\right)\right] \tag{2.34}$$

$$\tau_y = \mathfrak{Re}\left[\mu e^{i(\Omega_f t+\phi)-\frac{i\pi}{2}}\left(\sigma_+ C_1 - \sigma_- C_2\right)\right] \tag{2.35}$$

in the local Cartesian coordinate system. Similarly, we give the solutions at the pole and the equator. At $\theta = 0$, we have

$$\tau_x = \frac{\mu U}{\sqrt{2}L_v}(\cos\Omega_f t - \sin\Omega_f t) = \frac{\mu U}{L_v}\cos\left(\Omega_f t - 45°\right) \tag{2.36}$$

$$\tau_y = \frac{-\mu U}{\sqrt{2}L_v}(\sin\Omega_f t + \cos\Omega_f t) = \frac{-\mu U}{L_v}\sin\left(\Omega_f t - 45°\right) \tag{2.37}$$

Comparison to the boundary velocity shows that the velocity is leading the stress by 45 degrees. We define the veering angle β as the phase difference between the boundary velocity and the surface shear stress[3]. It determines the magnitude of the viscous power from $\boldsymbol{\tau}$: smaller β means larger power. At $\theta = 90°$, we have

$$\tau_x = 0 \tag{2.38}$$

$$\tau_y = \frac{-\mu U}{\sqrt{2}L_v}(\sin\Omega_f t + \cos\Omega_f t) = \frac{-\mu U}{\sqrt{2}L_v}\sin\left(\Omega_f t + 45°\right) \tag{2.39}$$

[3]One can also consider the velocity and the stress vectors in complex form, e.g., $\underline{\boldsymbol{u}} = u_x + iu_y$, and define the veering angle β as the argument difference between $\underline{\boldsymbol{\tau}}$ and $\underline{\boldsymbol{u}}$, i.e., $\beta = \mathrm{Arg}[\underline{\boldsymbol{\tau}}] - \mathrm{Arg}[\underline{\boldsymbol{u}}]$. However, the definition is only valid at the poles where the vector components have the same magnitude.

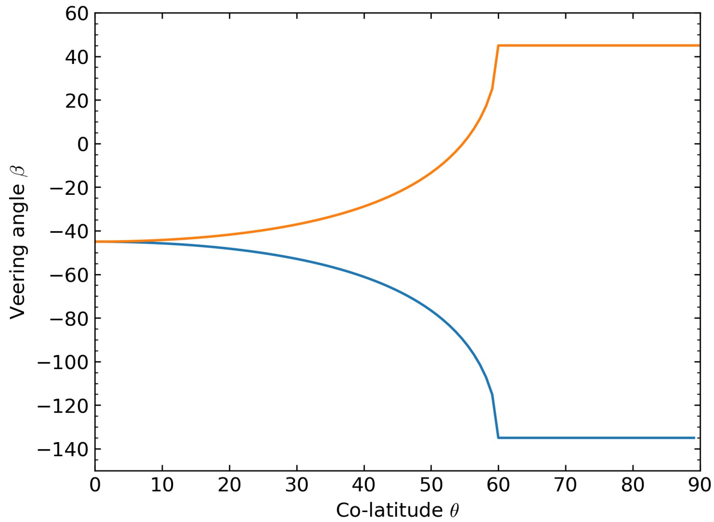

Figure 2.20: Veering angle β as a function of co-latitude θ. Veering angle is defined as the phase difference between the boundary velocity and the surface shear stress. The phase is computed by least square fit. Blue: derived from the x-component; orange: derived from the y-component. At $\theta = 90°$, both the velocity and the stress are zeros, so the phase cannot be defined.

Comparison with the boundary velocity at $\theta = 90°$ shows that the stress is leading the velocity by 45°. We note that the phases derived from the x- and y-components evolve in opposite directions when θ increases from 0° (Figure 2.20). Derived from the y-component, β increases from $-45°$ at the north pole to $+45°$ at the critical latitude and then remains till the equator. The flow shows distinct features in the polar region and equatorial region, the border being $\theta = 60°$.

From this Cartesian model we compute the viscous torque on a spherical surface S of radius R by integrating the local contributions: $\boldsymbol{\Gamma} = \int \boldsymbol{R} \times \boldsymbol{\tau}\, dS$. In a spherical coordinate system, we have $\tau_\theta = -\tau_y$ and $\tau_\phi = \tau_x$, where τ_x and τ_y are local stresses given by Equations 2.34 and 2.35. The local torque is $\boldsymbol{R} \times \boldsymbol{\tau} = -R\tau_\phi \hat{\boldsymbol{\theta}} + R\tau_\theta \hat{\boldsymbol{\phi}}$. Total torque is given by integrating over the whole spherical surface. After changing to a global Cartesian coordinate system $(\hat{\boldsymbol{X}}, \hat{\boldsymbol{Y}}, \hat{\boldsymbol{Z}})$, we have the torque exerted on the core

$$\Gamma_X = \int \left(-\cos\theta \cos\phi \tau_\phi - \sin\phi \tau_\theta\right) R^3 \sin\theta d\theta d\phi \tag{2.40}$$

$$\Gamma_Y = \int \left(-\cos\theta \sin\phi \tau_\phi + \cos\phi \tau_\theta\right) R^3 \sin\theta d\theta d\phi \tag{2.41}$$

$$\Gamma_Z = \int \sin\theta \tau_\phi R^3 \sin\theta d\theta d\phi \tag{2.42}$$

The integrals can be computed numerically. In the end, we have

$$\begin{aligned}\mathbf{\Gamma} = -I\Delta\Omega\frac{\sqrt{\nu\Omega_f}}{R}\Big[&(0.258\sin\Omega_f t + 2.62\cos\Omega_f t)\,\hat{\boldsymbol{X}} \\ &+ (-2.62\sin\Omega_f t + 0.258\cos\Omega_f t)\,\hat{\boldsymbol{Y}}\Big]\end{aligned} \tag{2.43}$$

where $I = (8\pi/15)\rho R^5$ is the moment of inertia of the sphere. In the fluid frame, the torque circulates in clockwise direction. Transformed back to the precessing frame (see Equation 2.16), the torque becomes

$$\mathbf{\Gamma} = -I\Delta\Omega\frac{\sqrt{\nu\Omega_f}}{R}\left(2.62\hat{\boldsymbol{X}}_p + 0.258\hat{\boldsymbol{Y}}_p\right) \tag{2.44}$$

We note that the imposed boundary velocity in our local model implies that the vector of differential rotation is given by $\Delta\boldsymbol{\Omega} = -\Delta\Omega\hat{\boldsymbol{X}}_p$. In this case, Equation 2.43 agrees with the ones derived from previous studies (e.g. Yoder, 1981; Williams et al., 2001; Cébron et al., 2019), where the results are based on the solution for the spin-over mode (Greenspan, 1968). In principle, the boundary velocity can be modified to represent other type of flow (e.g. spin-up) and the above formulation can be applied to derive the corresponding torque (e.g. Noir & Cébron, 2013).

Chapter 3

The effect of turbulent torque on the solution of precession-driven flow

3.1 Introduction

Precession-driven flow, particularly in the zeroth-order approximation as a rigid body rotation, results from a torque balance, which involves viscous, pressure, and precessional torques. Noir et al. (2003) demonstrated that an implicit equation for fluid rotation can be derived by using viscous torque from the spin-over mode. As we will show, this viscous torque holds for laminar boundary layers. However, a key question arises: if the boundary layer becomes turbulent, will the solution remain unchanged?

To address this, we first derive the viscous torque, demonstrating that it can be approximated by the surface shear stress exerted on the boundary. To approximate the boundary layer in precession-driven flow, we can use an oscillatory Ekman layer, whose analytical and numerical solutions are discussed in Chapter 2. Next, we estimate the torque in the turbulent regime, called the turbulent torque, and update the solution for the fluid rotation.

3.2 Theoretical development

3.2.1 Torque balance

Precession-driven flow is resembling, to leading order, a rigid body rotation. The fluid rotation can be determined by considering the torque balance on the core. We follow the convention in literature to formulate the problem in the precessing frame, which is attached to the Earth's precession.

The Navier-Stokes equation in the precessing frame,

$$\frac{\partial \boldsymbol{u}}{\partial t} + \boldsymbol{u} \cdot \nabla \boldsymbol{u} = -\frac{1}{\rho} \nabla P + \nu \nabla^2 \boldsymbol{u} - 2\boldsymbol{\Omega}_p \times \boldsymbol{u}, \tag{3.1}$$

leads to a torque balance equation[1]:

$$\begin{aligned}\int_V \boldsymbol{r} \times \frac{\partial \boldsymbol{u}}{\partial t} dV + \oint_{\partial V} (\boldsymbol{r} \times \boldsymbol{u}) (\boldsymbol{u} \cdot \hat{\boldsymbol{n}}) \, dS = -\frac{1}{\rho} \oint_{\partial V} (\boldsymbol{r} \times \hat{\boldsymbol{n}}) \, P dS \\ + \nu \oint_{\partial V} [\boldsymbol{r} \times (\hat{\boldsymbol{n}} \cdot \nabla) \boldsymbol{u} - \boldsymbol{u} \times \hat{\boldsymbol{n}}] \, dS - \int_V \boldsymbol{r} \times (2\boldsymbol{\Omega}_p \times \boldsymbol{u}) \, dV\end{aligned} \tag{3.2}$$

by applying $\boldsymbol{r}\times$ to Equation 3.1 and integrating over the volume V. Equation 3.2 shows that the change of angular momentum is equal to the torques exerted on the core, including pressure (first term on RHS), viscous (second term on RHS), and precessional (third term on RHS) torques. First of all, without any specific restriction, the non-linear term (second term on LHS) is zero as long as the flow satisfies the no-penetration condition $\boldsymbol{u} \cdot \hat{\boldsymbol{n}}$. On top of that, if the CMB is axisymmetric, then according to Busse (1968), there exists a stationary solution and thus the inertia term is zero. Furthermore, the pressure torque will vanish if the CMB is spherical so that $\boldsymbol{r}$ is parallel to $\hat{\boldsymbol{n}}$.

It is important to note that the non-linear, pressure, and viscous terms have been transformed from volume integrals into surface integrals. I present the surface integral formulations of the three torque components in the following. The derivations demonstrate that the torque balance equation is valid for any incompressible flow, regardless of whether Poincare flow is assumed. These derivations rely on the divergence theorem, also known as Gauss's theorem, which is given by (see e.g. Chapter 3 of Arfken et al., 2011)

$$\int_V \nabla \cdot \boldsymbol{F} \, dV = \oint_{\partial V} \boldsymbol{F} \, \hat{\boldsymbol{n}} \, dS \tag{3.3}$$

where $\boldsymbol{F}$ is a vector and $\hat{\boldsymbol{n}}$ is the unit normal vector to the surface element dS. Two useful alternative expressions can be derived by considering different forms for the vector $\boldsymbol{F}$. First, by setting $\boldsymbol{F}$ to be $\boldsymbol{a} \times \boldsymbol{F}$, where $\boldsymbol{a}$ is a constant vector field, we obtain:

$$\int_V \nabla \times \boldsymbol{F} dV = \oint_{\partial V} \hat{\boldsymbol{n}} \times \boldsymbol{F} dS \tag{3.4}$$

Additionally, by using the identity $\nabla \cdot (\psi \nabla \phi) = \psi \nabla^2 \phi + (\nabla \psi) \cdot (\nabla \phi)$, where ψ and ϕ are scalar functions, we derive:

$$\int_V \psi \nabla^2 \phi \, dV = \oint_{\partial V} \psi \nabla \phi \cdot \hat{\boldsymbol{n}} \, dS - \int_V (\nabla \psi) \cdot (\nabla \phi) \, dV \tag{3.5}$$

These derivations are made clearer by employing index notation, in which a vector $\boldsymbol{u}$ is represented as $u_i \hat{\boldsymbol{e}}_i$, where $\hat{\boldsymbol{e}}_i$ are unit vectors and summation over repeated indices is implied.

Pressure torque

$$-\frac{1}{\rho} \int_V (\boldsymbol{r} \times \nabla P) \, dV = -\frac{1}{\rho} \oint_{\partial V} P \, (\boldsymbol{r} \times \hat{\boldsymbol{n}}) \, dS \tag{3.6}$$

[1] Specifically, it is a *unit density* torque balance equation.

To derive the equation, I rewrite $\boldsymbol{r} \times \nabla P$ as $P(\nabla \times \boldsymbol{r}) - \nabla \times (P\boldsymbol{r})$ by using vector identity. Since $\nabla \times \boldsymbol{r} = 0$, the volume integral now can be converted to a surface integral via Equation 3.4:

$$-\frac{1}{\rho}\int_V \nabla \times (P\boldsymbol{r})\, dV = -\frac{1}{\rho}\oint_{\partial V} P\,(\boldsymbol{r} \times \hat{\boldsymbol{n}})\, dS \tag{3.7}$$

which provides the first term on the RHS of Equation 3.2. It shows that the pressure torque vanishes on a spherical surface, where $\boldsymbol{r}$ is parallel to $\hat{\boldsymbol{n}}$.

Non-linear torque

$$\int_V \boldsymbol{r} \times (\boldsymbol{u} \cdot \nabla \boldsymbol{u})\, dV = \oint_{\partial V} (\boldsymbol{r} \times \boldsymbol{u})\,(\boldsymbol{u} \cdot \hat{\boldsymbol{n}})\, dS \tag{3.8}$$

I start the derivation by expressing $\boldsymbol{r} \times (\boldsymbol{u} \cdot \nabla \boldsymbol{u})$ as $(\boldsymbol{u} \cdot \nabla)(\boldsymbol{r} \times \boldsymbol{u})$, which can be demonstrated via

$$\begin{aligned}(\boldsymbol{u} \cdot \nabla)(\boldsymbol{r} \times \boldsymbol{u}) &= u_t \frac{\partial}{\partial x_t}\left(\epsilon_{ijk} x_i u_j \hat{\boldsymbol{e}}_k\right) \\ &= \epsilon_{ijk} u_t \underbrace{\left(\frac{\partial x_i}{\partial x_t}\right)}_{=\delta_{it}} u_j \hat{\boldsymbol{e}}_k + \epsilon_{ijk} u_t x_i \left(\frac{\partial u_j}{\partial x_t}\right) \hat{\boldsymbol{e}}_k \\ &= \epsilon_{ijk} u_i u_j \hat{\boldsymbol{e}}_k + \epsilon_{ijk} u_t x_i \left(\frac{\partial u_j}{\partial x_t}\right) \hat{\boldsymbol{e}}_k = \boldsymbol{u} \times \boldsymbol{u} + \boldsymbol{r} \times (\boldsymbol{u} \cdot \nabla)\boldsymbol{u}\end{aligned} \tag{3.9}$$

given that $\boldsymbol{u} \times \boldsymbol{u} = 0$ for any $\boldsymbol{u}$. Next, with $\nabla \cdot \boldsymbol{u} = 0$, the term $(\boldsymbol{u} \cdot \nabla)(\boldsymbol{r} \times \boldsymbol{u})$ can be further expressed as $\nabla \cdot [\boldsymbol{u}(\boldsymbol{r} \times \boldsymbol{u})]$:

$$\begin{aligned}&(\boldsymbol{u} \cdot \nabla)(\boldsymbol{r} \times \boldsymbol{u}) + (\nabla \cdot \boldsymbol{u})(\boldsymbol{r} \times \boldsymbol{u}) \\ &= u_t \frac{\partial}{\partial x_t}\left(\epsilon_{ijk} x_i u_j \hat{\boldsymbol{e}}_k\right) + \left(\frac{\partial u_t}{\partial x_t}\right)\left(\epsilon_{ijk} x_i u_j \hat{\boldsymbol{e}}_k\right) \\ &= \frac{\partial}{\partial x_t}\left(u_t \epsilon_{ijk} x_i u_j \hat{\boldsymbol{e}}_k\right) = \nabla \cdot [\boldsymbol{u}(\boldsymbol{r} \times \boldsymbol{u})]\end{aligned} \tag{3.10}$$

where the term in the square bracket is a rank two tensor. Finally, applying the divergence theorem leads to the desired expression (the second term on the LHS of Equation 3.2). The applicability of the divergence theorem to a rank two tensor can be proved by considering the conventional divergence theorem, Equation 3.3 denoted as $\int_V (\partial F_i/\partial x_i) dV = \oint_{\partial V} F_i \hat{n}_i dS$, and an auxiliary constant vector $\boldsymbol{a}$:

$$a_i \int_V \frac{\partial F_{ij}}{\partial x_j} dV = \int_V \frac{\partial}{\partial x_j}(a_i F_{ij}) dV = \oint_{\partial V} (a_i F_{ij}) \hat{n}_j dS = a_i \oint_{\partial V} F_{ij} \hat{n}_j dS \tag{3.11}$$

The overall derivation shows that the torque expressed in the surface integral is valid for any velocity field of an incompressible fluid.

Viscous torque

$$\nu \int_V \boldsymbol{r} \times \nabla^2 \boldsymbol{u}\, dV = \nu \oint_{\partial V} [\boldsymbol{r} \times (\hat{\boldsymbol{n}} \cdot \nabla)\boldsymbol{u} - \boldsymbol{u} \times \hat{\boldsymbol{n}}]\, dS \tag{3.12}$$

The logic behind the derivation is to apply Equation 3.5 to each component of the volume integral:

$$\begin{aligned}
&\nu \int_V \epsilon_{ijk} x_i \frac{\partial^2}{\partial x_t^2}(u_j \hat{\boldsymbol{e}}_k)\, dV \\
&= \nu \int \epsilon_{ijk} x_i \hat{n}_t \frac{\partial}{\partial x_t}(u_j \hat{\boldsymbol{e}}_k)\, dS - \nu \int \epsilon_{ijk} \underbrace{\left(\frac{\partial x_i}{\partial x_t}\right)}_{=\delta_{it}} \left(\frac{\partial u_j}{\partial x_t}\right) \hat{\boldsymbol{e}}_k\, dV \\
&= \nu \oint_{\partial V} \boldsymbol{r} \times (\hat{\boldsymbol{n}} \cdot \nabla)\boldsymbol{u}\, dS - \nu \int_V \nabla \times \boldsymbol{u}\, dV
\end{aligned} \tag{3.13}$$

The last term can be converted to a surface integral according to Equation 3.4, leading to the second term on the RHS of Equation 3.2. Nevertheless, viscous torque can be separated into two parts. The first part is related to the velocity gradient along the normal direction, which is equivalent to the surface shear stress. In the following, I will focus on this part.

3.2.2 Turbulent torque

We consider the viscous torque that is related to the surface shear stress exerted on the boundary and denote it as

$$\boldsymbol{\Gamma}_\nu = \oint_{\partial V} (\boldsymbol{r} \times \boldsymbol{\tau})\, dS \tag{3.14}$$

where $\boldsymbol{\tau} = \mu(\hat{\boldsymbol{n}} \cdot \nabla)\boldsymbol{u}$ is the surface shear stress and $\mu = \rho\nu$ is the dynamic viscosity. To further analyze the viscous torque, we factor out the physical units and evaluate the surface integral numerically using dimensionless variables. We express the surface shear stress as:

$$\boldsymbol{\tau} = \mu L_\nu^{-1} U \boldsymbol{\tau}_0^* \tag{3.15}$$

where $\boldsymbol{\tau}_0^* = (\hat{\boldsymbol{n}} \cdot \nabla^*)\boldsymbol{u}^*$ and the superscript * indicates dimensionless variables or parameters. Note that $\boldsymbol{\tau}_0^*$ is the velocity gradient along the normal vector and serves as a proxy for the surface shear stress. The viscous torque can then be written as

$$\boldsymbol{\Gamma}_\nu = -I\Delta\Omega \frac{\sqrt{\nu\Omega_f}}{R} \boldsymbol{\Gamma}_\nu^* \tag{3.16}$$

where the viscous torque coefficients $\boldsymbol{\Gamma}_\nu^*$ are defined as

$$\boldsymbol{\Gamma}_\nu^* = -\left(\frac{15}{8\pi}\right) \oint_{\partial V} (\hat{\boldsymbol{r}} \times \boldsymbol{\tau}_0^*)\, \sin\theta d\theta d\phi, \tag{3.17}$$

and $\hat{\boldsymbol{r}} = \boldsymbol{r}/R$. The moment of inertia for a uniform sphere, $I = (8\pi/15)\rho R^5$, has been used.

To calculate $\boldsymbol{\Gamma}_\nu^*$ explicitly, we adopt the solution for the surface shear stress of an oscillatory Ekman layer, which was discussed in Chapter 2 both in the laminar and the turbulent regime. It is important to note that the solution is obtained in a local coordinate system with a frame of reference that is attached to the fluid rotation. To adopt the solution, we will apply a series of coordinate transformations between coordinate systems and reference frames, which have been discussed in the previous chapter.

In the laminar regime, we use the analytical solution for the surface shear stress, which is given by (see Appendix 2.B for the detailed derivation)

$$\tau_{0,x}^* = \mathfrak{Re}\left[e^{i(\Omega_f t+\phi)}\left(\sigma_+^* C_1^* + \sigma_-^* C_2^*\right)\right] \tag{3.18}$$

$$\tau_{y,0}^* = \mathfrak{Re}\left[e^{i(\Omega_f t+\phi)-\frac{i\pi}{2}}\left(\sigma_+^* C_1^* - \sigma_-^* C_2^*\right)\right] \tag{3.19}$$

where $C_1^* = (\cos\theta - 1)/2$, $C_2^* = (\cos\theta + 1)/2$, and $\sigma_\pm^* = \sqrt{(1 \pm 2\cos\theta)i}$. Surface integration leads to a time-dependent viscous torque. We then apply the coordinate transformation from the fluid frame to the precession frame using Equation 2.16, resulting in the viscous torque coefficients:

$$\boldsymbol{\Gamma}_\nu^* = 2.62\hat{\boldsymbol{X}}_p + 0.258\hat{\boldsymbol{Y}}_p \tag{3.20}$$

This result is consistent with that obtained from the viscous decay of a spin-over mode (Noir & Cébron, 2013).

To further explore the turbulent regime, we use the surface shear stress obtained from the numerical simulations presented in the previous chapter. Each simulation is used to approximate a single point on the spherical surface. In the numerical model, we select one longitude, say $\phi = 0$, and solve for the time evolution. Due to the azimuthal symmetry observed in the boundary velocity, the solutions at different ϕ are generally identical but different in phase. That means integration in time is equivalent to ϕ-integration. We use the time average to approximate the integration along ϕ and use the trapezoidal method to integrate along θ. Table 3.1 shows the viscous torque coefficients at different Re. Note that at low Re, the result is consistent with the analytical solution obtained in the laminar regime. The small discrepancy is due to the limited number of simulations conducted accross θ, ten in total. The values of $(2.50, 0.245)$ can be reproduced analytically by restricting to the same number of θ used. Nevertheless, the result shows that both the equatorial components increase as Re increases as a result of turbulence.

For extrapolation to higher Re, we use the turbulence model for viscous dissipation (Equation 2.13): $\mathcal{D}_\nu = -2.62\sqrt{2}\chi k I\left|\Delta\boldsymbol{\Omega}\right|^3$ with $\chi = 0.85$. Since the dissipation can also be computed via $\mathcal{D}_\nu = -\boldsymbol{\Gamma}_\nu \cdot \Delta\boldsymbol{\Omega}$, it is possible to recover the torque using this relation. In the fluid system, we define the differential rotation as $\Delta\boldsymbol{\Omega} = -\Delta\Omega\hat{\boldsymbol{X}}_p$. Thus, we obtain:

$$\boldsymbol{\Gamma}_\nu \cdot \hat{\boldsymbol{X}}_p = -I\Delta\Omega\frac{\sqrt{\nu\Omega_f}}{R}\left[2.62\sqrt{2}\,\chi\,k\,Re\right] \tag{3.21}$$

Recall that $k = (u_*/U)^2\cos\beta$, which we can estimate for a given high Re from the similarity theory discussed in Section 2.4.2. Notice that from the

Table 3.1: Viscous torque coefficients $\mathbf{\Gamma}_\nu^*$ calculated based on the box model up to $Re = 700$. The torque is calculated by summing the local contribution (i.e. $\hat{\boldsymbol{r}} \times \boldsymbol{\tau}_0^*$) over a spherical surface. The stresses at $\theta = 60°$ are replaced by the analytical solutions.

Re	$\mathbf{\Gamma}_\nu^* \cdot \hat{\boldsymbol{X}}_p$	$\mathbf{\Gamma}_\nu^* \cdot \hat{\boldsymbol{Y}}_p$	$\mathbf{\Gamma}_\nu^* \cdot \hat{\boldsymbol{Z}}_p$
5	2.50	0.245	0
100	2.50	0.244	0
200	2.53	0.266	0.01
300	3.36	0.300	0.04
400	4.19	0.361	0.07
500	4.84	0.509	0.13
700	6.35	0.642	0.18

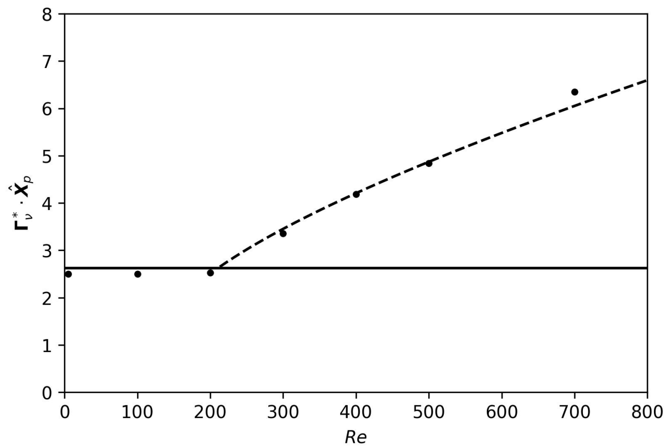

Figure 3.1: Viscous torque coefficient $\mathbf{\Gamma}_\nu^* \cdot \hat{\boldsymbol{X}}_p$ as a function of Re. Solid line: nominal value 2.62. Dashed line: turbulent torque (Equation 3.21). Dots: numerical solutions obtained from the box model presented in Chapter 2.

dissipation alone, we can only infer the $\hat{\boldsymbol{X}}_p$-component. No information on the $\hat{\boldsymbol{Y}}_p$-component is available, as it is not associated with dissipation. Figure 3.1 shows the comparison of the viscous torque coefficient $\mathbf{\Gamma}_\nu \cdot \hat{\boldsymbol{X}}_p$ obtained from the three different approaches: the analytical solution, the numerical solution, and the turbulence model.

3.2.3 Approximate solution

The viscous torque derived by Noir et al. (2003) is equivalent to the one presented above. Their approach to derive viscous torque relies on the solution of Greenspan (1968) for the viscous decay of the spin-over mode in a rotating fluid. They showed that the torque balance equation can lead to an implicit equation for the fluid rotation, which is identical to the one first derived by Busse (1968).

Following the present formulation, we express the implicit equation as

$$\frac{\boldsymbol{\Omega}_f}{\Omega_f^2} = \hat{\boldsymbol{Z}} + \frac{\mathcal{A}}{\mathcal{A}^2 + \mathcal{B}^2} \hat{\boldsymbol{Z}} \times (Po\, \hat{\boldsymbol{k}}_p \times \hat{\boldsymbol{Z}}) + \frac{\mathcal{B}}{\mathcal{A}^2 + \mathcal{B}^2} \hat{\boldsymbol{Z}} \times Po\, \hat{\boldsymbol{k}}_p \tag{3.22}$$

where

$$\mathcal{A} = \left(\boldsymbol{\Gamma}_\nu^* \cdot \hat{\boldsymbol{Y}}_p \right) \sqrt{\frac{E}{\Omega_f}} + \epsilon_f\, \Omega_f^2 + Po \cos\alpha \tag{3.23}$$

and

$$\mathcal{B} = \left(\boldsymbol{\Gamma}_\nu^* \cdot \hat{\boldsymbol{X}}_p \right) \sqrt{E\, \Omega_f} \tag{3.24}$$

The vector $\hat{\boldsymbol{Z}}$ represents the mantle rotation as $\boldsymbol{\Omega}_m = \Omega_m \hat{\boldsymbol{Z}}$ and the coefficient ϵ_f stands for the polar flattening of the fluid core. For a given Re, we assign the corresponding viscous torque coefficients $\boldsymbol{\Gamma}_\nu^*$ and then solve for $\boldsymbol{\Omega}_f$.

We check the sensitivity of the coefficients $\boldsymbol{\Gamma}_\nu^* \cdot \hat{\boldsymbol{X}}_p$ on the solution for $\boldsymbol{\Omega}_f$, which is represented by its angular coordinates θ_f and ϕ_f. We consider a case with $Po = 10^{-3}$ and $\alpha = 30°$. Figures 3.2 and 3.3 show θ_f and ϕ_f as a function of $\boldsymbol{\Gamma}_\nu^* \cdot \hat{\boldsymbol{X}}_p$, with E ranging from 10^{-4} to 10^{-12}. Either for high or low E (e.g. 10^{-4} or 10^{-12}), the changes in θ_f and ϕ_f are relatively small. On the other hand, for intermediate E (e.g. 10^{6} to 10^{-10}), the variation could be large. We may conclude that the turbulent torque can only significantly alter the solution of $\boldsymbol{\Omega}_f$ when conditions are right. For a given set of Po and ϵ_f, there is only a certain range of E that the variation of $\boldsymbol{\Omega}_f$ is large. For the Earth and the Moon, they are not in this range, so the turbulence effect on the solution of $\boldsymbol{\Omega}_f$ is small.

3.3 Implications

We consider three cases—the Earth, the Moon, and a laboratory experiment—where the Reynolds numbers suggest that the boundary layers may be turbulent. We then apply the corresponding viscous torque coefficients and calculate the updated Reynolds numbers. This iterative process is repeated until the results converge.

3.3.1 Earth and Moon

The relevant parameters for the Earth's and the Moon's precession are presented in Table 1.1. For the Earth, the initial Reynolds number is 481. By applying linear interpolation to the viscous torque coefficients, $\boldsymbol{\Gamma}_\nu^*$, obtained from numerical simulations, we determine values of 4.72 and 0.482 for the two equatorial components, respectively. The updated Reynolds number differs from the initial value by only -0.0003%. For the Moon, with an initial Reynolds number of 1.58×10^4, our turbulence model (Equation 3.21) predicts $\boldsymbol{\Gamma}_\nu^* \cdot \hat{\boldsymbol{X}}_p = 51.48$, resulting in an updated Reynolds number that differs from the initial value by -0.02%.

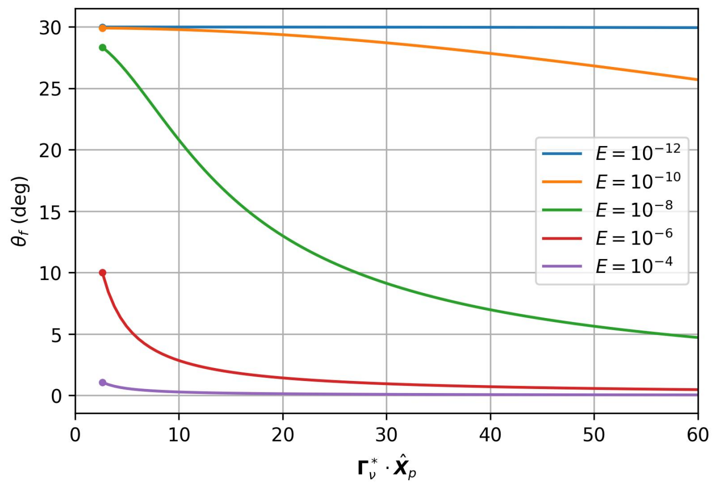

Figure 3.2: The solutions of θ_f as a function of $\mathbf{\Gamma}^*_\nu \cdot \hat{\boldsymbol{X}}_p$ with different E (different colors; see the legend). The dot on the left represents the solution obtained at the laminar value of 2.62. We fix $\mathbf{\Gamma}^*_\nu \cdot \hat{\boldsymbol{Y}}_p = 0.259$.

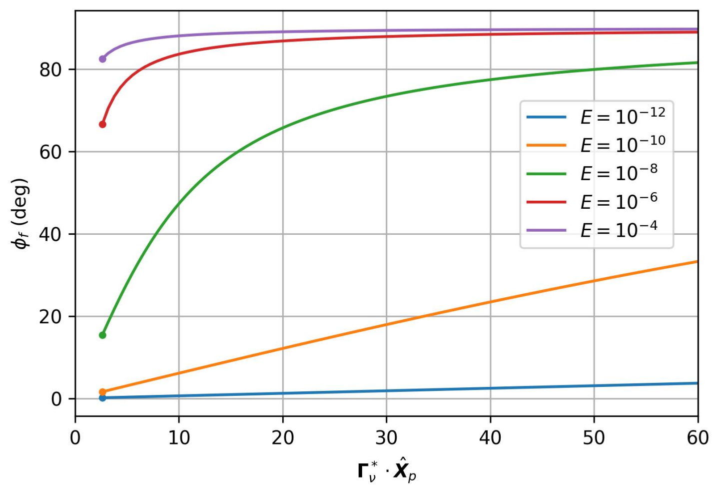

Figure 3.3: The solutions of ϕ_f as a function of $\mathbf{\Gamma}^*_\nu \cdot \hat{\boldsymbol{X}}_p$ with different E (different colors; see the legend). The dots on the left represent the solutions obtained at the laminar value of 2.62. We fix $\mathbf{\Gamma}^*_\nu \cdot \hat{\boldsymbol{Y}}_p = 0.259$.

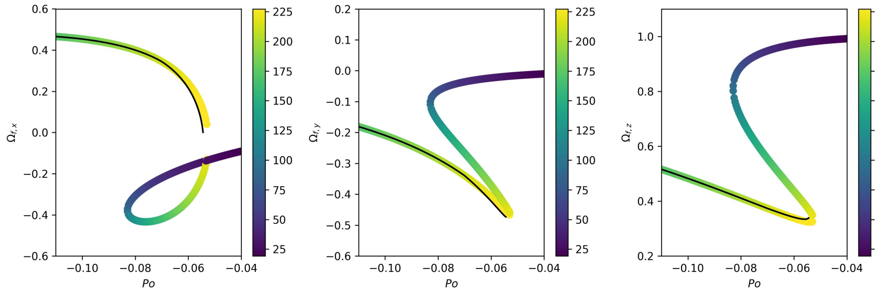

Figure 3.4: Components of the solution $\mathbf{\Omega}_f$ as a function of Po for the case with Ekman number $E = 2.3 \times 10^{-5}$, precession angle $\alpha = 15°$, and flattening $\epsilon_f = 0.15$. The colorbar represents the Reynolds number Re. Black line is the updated solution.

3.3.2 Laboratory experiment

Nobili et al. (2021) showed that it is likely that the boundary layer of a precessing spheroid with a moderate precession angle becomes turbulent based on their experiment setup. Here, we use the present formulation to estimate the effect of turbulence on the fluid rotation. The experiment setup has Ekman number $E = 2.3 \times 10^{-5}$, precession angle $\alpha = 15°$, and flattening $\epsilon_f = 0.15$. First, we use Busse's implicit equation together with the laminar viscous torque coefficients and solve for $\mathbf{\Omega}_f$. We also calculate the corresponding Re for each solution. Figure 3.4 shows the maximum Re is about 225, which according to our numerical result is at the margin of becoming turbulent. Nevertheless, we calculate the updated $\mathbf{\Omega}_f$ by using the corresponding $\mathbf{\Gamma}^*_\nu$. The result shows that the turbulence effect is small and the difference of $\Omega_{f,y}$ between the updated solution to the original solution is within 5%.

3.4 Discussion and conclusions

The procedure to convert the volume integrals of the torques to the surface integrals involves various tricks from vector analysis and alternative forms for the divergence theorem. I try to present a detailed and self-consistent derivation with the vector notations that are common to recent physics textbooks, hoping that the derivation itself helps readers to better understand the nature of those torques. Specifically, regarding the non-linear torque, I was motivated by Rochester (1962) who derived the surface integral form of the electromagnetic torque, which was not discussed in the present study but could also couple the core and the mantle of the Earth, by using the Maxwell stress representation. The derivation presented in this chapter should be able to complement the discussion on electromagnetic torque made in the literature (e.g. Greff-Lefftz & Legros, 1995; Roberts & Aurnou, 2012; Kuang et al., 2017).

The impact of turbulent torque on the fluid rotation solution can be significant under certain combinations of relevant parameters. However, this is not the case for the Earth, the Moon, or the experimental setup discussed earlier, where viscosity plays a minor role in the overall torque balance. Although turbulence in the boundary layer increases viscous coupling, it remains insufficient to affect the final solution. For the Earth, this result is expected as the Reynolds number is near the critical value so that the turbulence effect itself is small. Besides, the Earth's core-mantle boundary flattening is large enough so that the pressure torque dominates the viscous torque. As argued by Buffett (2021), viscosity can be considered as a correction to the solution of the fluid rotation, ensuring the no-slip boundary condition, because the flattening is much larger than the Poincaré number.

For the Moon, even though the above two restrictions for the Earth are relaxed, the turbulence effect remains negligible. First, the Reynolds number for the Moon's boundary layer is at least one order larger than that of the Earth, and thus the viscous torque coefficients are correspondingly larger, implying a stronger turbulent effect. Second, the Moon's core-mantle boundary flattening is also smaller given its slower rotation. We even tested a scenario for the Moon which has a spherical boundary, and the difference between the initial and the updated solutions remained negligible. Indeed, the Moon's shape also constitutes a component of a triaxial ellipsoid due to the tidal force. Noir and Cébron (2013) showed that for such non-axisymmetric geometries, forced flow is unsteady and periodic. While this added complexity affects flow characteristics, it should not change our conclusion that the effect of turbulence is negligible.

Appendix 3.A: Viscous torque derived from spin-over mode

In this paragraph alone, the convention is based on Noir and Cébron (2013) and the equation number refers to therein. The time scale is Ω_0^{-1}, where Ω_0 is the rotation of the cavity in the precessing frame. The coordinate system is precessing and the z-axis is aligned with the mantle rotation vector; I shall call it the mantle coordinate system in the precessing frame. In this coordinate system, the mantle rotation vector is given by $\hat{\boldsymbol{k}} = (0, 0, 1)$, while the fluid rotation vector is $\boldsymbol{\Omega} = (\Omega_x, \Omega_y, \Omega_z)$, which is dimensionless. I used the python package `sympy` to derive the analytical expression. The viscous torque (Equation A13) is obtained by taking time derivative of the time evolution of the spin-over mode (Equation A7) and spin-up/spin-down of the fluid (Equation A9). I noticed that, in order to derive Equation A13, the exponential term in Equation A9, $(\lambda^*_{sup} E_f t_f)$, should be replaced by $(\lambda^*_{sup} E_f^{1/2} t_f)$. Besides, the coefficient in Eq. (A11) should be $\lambda_{sup}\sqrt{E\Omega}$. The credibility of Equation A13 is higher than others because it also appeared in Cébron (2015) and the manuscript from personal communication. Based on my calculation, the viscous torque is

$$\mathcal{L}\boldsymbol{\Gamma}_\nu = \sqrt{E\Omega}\left[\frac{\lambda^r_{so}}{\Omega^2}\begin{pmatrix}\Omega_x\Omega_z\\ \Omega_y\Omega_z\\ \Omega_z^2-\Omega^2\end{pmatrix} + \frac{\lambda^i_{so}}{\Omega}\begin{pmatrix}\Omega_y\\ -\Omega_x\\ 0\end{pmatrix} + \lambda_{sup}\frac{\Omega_z-\Omega^2}{\Omega^2}\begin{pmatrix}\Omega_x\\ \Omega_y\\ \Omega_z\end{pmatrix}\right] \tag{3.25}$$

where $\mathcal{L}$ is a 3×3 matrix related to inertia, $E = \nu/(\Omega_0 R^2)$ is the Ekman number, and $(\lambda^r_{so}, \lambda^i_{so}, \lambda_{sup})$ are coefficients associated with the spin-over and the spin-up.

In order to follow the analysis made in this chapter, I replace the coordinates of the two rotation vectors with: $\boldsymbol{\Omega}_m = (0, 0, \Omega_m)$ and $\boldsymbol{\Omega}_f = (\Omega_{f,x}, \Omega_{f,y}, \Omega_{f,z})$. Besides, the torque is multiplied by $\rho R^5 \Omega_m^2$ to recover physical units. Finally, the no spin-up condition is considered: $\boldsymbol{\Omega}_m \cdot \boldsymbol{\Omega}_f - |\boldsymbol{\Omega}_f|^2 = 0$, which is equivalent to $\Omega_m/\Omega_f^2 = 1/\Omega_{f,z}$. Following the same approach, the torque now reads

$$\boldsymbol{\Gamma}_\nu = \mathcal{I}\frac{\sqrt{\nu\Omega_f}}{R}\left[\lambda^r_{so}\begin{pmatrix}\Omega_{f,x}\\ \Omega_{f,y}\\ \Omega_{f,z}-\Omega_m\end{pmatrix} + \lambda^i_{so}\frac{\Omega_f}{\Omega_{f,z}}\begin{pmatrix}\Omega_{f,y}\\ -\Omega_{f,x}\\ 0\end{pmatrix}\right] \tag{3.26}$$

where $\mathcal{I} = \mathcal{L}^{-1}\rho R^5$ is the inertia tensor. For a sphere, we have $\mathcal{I} = \frac{8\pi}{15}\rho R^5 \delta_{ij}$ and $(\lambda^r_{so}, \lambda^i_{so}) = (-2.62, 0.258)$. Finally, we get

$$\boldsymbol{\Gamma}_\nu = -I\frac{\sqrt{\nu\Omega_f}}{R}\left[2.62\begin{pmatrix}\Omega_{f,x}\\ \Omega_{f,y}\\ \Omega_{f,z}-\Omega_m\end{pmatrix} + 0.258\begin{pmatrix}-\Omega_{f,y}/\cos\theta_f\\ \Omega_{f,x}/\cos\theta_f\\ 0\end{pmatrix}\right] \tag{3.27}$$

where $I = \frac{8\pi}{15}\rho R^5$ and $\theta_f = \cos^{-1}(\boldsymbol{\Omega_m}\cdot\boldsymbol{\Omega}_f)$. Further simplification made by Cébron et al. (2019) to obtain tractable analytical solutions assumes that the fluid rotates at the same rate as the boundary, i.e. $\Omega_f = \Omega_m$, which implies $\theta_f = 0$ under no spin-up condition, thus leading to their Equation A10.

The expression for the torque can be further simplified by changing the coordinate system. Suppose the coordinate system is defined such that the

z-axis is aligned with $\mathbf{\Omega}_f$. I shall call this coordinate system the fluid system. Recall that in the mantle system, the co-latitude of $\mathbf{\Omega}_f$ is θ_f and the longitude is ϕ_f. We substitute the coordinates $(\Omega_{f,x}, \Omega_{f,y}, \Omega_{f,z})$ by functions of (θ_f, ϕ_f) to facilitate coordinate transformation. The relations are given by $\Omega_{f,x} = \Delta\Omega\cos\theta_f\cos\phi_f$, $\Omega_{f,y} = \Delta\Omega\cos\theta_f\sin\phi_f$, and $\Omega_{f,z} = \Omega_m - \Delta\Omega\sin\theta_f$. After the substitution, the torque reads

$$\mathbf{\Gamma}_\nu = -I\Delta\Omega\frac{\sqrt{\nu\Omega_f}}{R}\left[2.62\begin{pmatrix}\cos\theta_f\cos\phi_f\\ \cos\theta_f\sin\phi_f\\ -\sin\theta_f\end{pmatrix} + 0.258\begin{pmatrix}-\sin\phi_f\\ \cos\phi_f\\ 0\end{pmatrix}\right] \tag{3.28}$$

After the transformation to the fluid system, the torque will be equivalent to the one given in Equation 3.20. The fluid rotation vector is given by $\mathbf{\Omega}_f = (0, 0, \Omega_f)$ and the mantle rotation vector is given by $\mathbf{\Omega}_m = \Omega_m(-\sin\theta_f, 0, \cos\theta_f)$, which is lying on the negative x-axis.

Chapter 4

The effect of roughness on the boundary layer of precession-driven flow

4.1 Introduction

Precession drives the fluid motion in the core. To leading order, the motion is a rigid body rotation. A viscous boundary layer develops in order to satisfy the no-slip boundary condition. Energy dissipates mainly in the boundary layer due to viscous force. The viscous dissipation depends on whether the flow is turbulent or not (Shih et al., 2023). In the case of turbulence, it might as well be affected if roughness appears on the core-mantle boundary (CMB). A quantitative assessment of the roughness effect (Buffett & Christensen, 2007) often relies on dimensional arguments or laboratory experiments (Sleath, 1987), involving a turbulent oscillatory flow over a rough surface.

Dimensional arguments for the roughness effect on viscous dissipation rely on the concept of eddy viscosity, which can be approximated as $\nu_e \approx v\, l$ where v and l are the velocity and the size of the eddies. The eddy velocity can be approximated by the large-scale velocity, while the eddy size can be approximated by the length scale of the roughness if present. For the Earth's precession-driven flow, the velocity is about $4.1 \times 10^{-3}\,\mathrm{m\,s^{-1}}$. In order to obtain eddy viscosity larger than the conventional value for the outer liquid core of $\nu = 10^{-6}\,\mathrm{m\,s^{-1}}$, the required length scale should be $> O(10^{-3})\,\mathrm{m}$. This simple dimensional argument suggests that boundary roughness with millimeter scale could already affect the eddy viscosity. However, whether such small amplitude roughness can generate turbulence and the associated eddies remains to be further studied.

In this chapter, I study the effect of roughness on the boundary layer of precession-driven flow. The term *roughness* refers to small-scale undulations of the CMB. The length scale is at the order of a few centimeters, compatible with the boundary layer thickness. Large-scale topographies, which have wavelengths and heights of a few kilometers or larger, are not considered here; addressing such topographies requires a different approach. For instance, Puica et al. (2023) used spherical harmonics to parameterize CMB topography and study its impact on tidally driven length-of-day variations. Precession-driven flow, on the other hand, is a central focus of this study, as the flow is characterized by the largest velocity amplitude in the boundary layer compared to other rotationally driven flows like nutations.

In Section 4.2, I first determine the rotation of the fluid core based on the model for an axisymmetric spheroid and then describe the governing equations. In Section 4.3, I present the details of a local box model used to study boundary roughness, with a focus on the derivation of forces and the implementation of roughness. Finally, the results are presented in Section 4.4.2, followed by a discussion and conclusions in Section 4.5.

4.2 Mathematical description of the problem

Let's begin with Earth's precession. The Earth's rotation axis $\boldsymbol{\Omega}_m = \Omega_m \hat{\boldsymbol{k}}_m$ precesses around the axis $\boldsymbol{\Omega}_p = \Omega_p \hat{\boldsymbol{k}}_p$ at angle α. This precession drives the fluid motion within the Earth's core. To the zeroth order, the fluid motion resembles a rigid body rotation $\boldsymbol{\Omega}_f = \Omega_f \hat{\boldsymbol{k}}_f$. Note that $\hat{\boldsymbol{k}}_i$, where $i = m, p, f$, are unit vectors. Roughness on the CMB can interact with this flow through the boundary layer. To study the interaction, I formulate the problem in a reference frame which is attached to $\boldsymbol{\Omega}_f$, hereafter referred to as the fluid frame. In this frame, the bulk of the fluid core is at rest while the mantle rotates with $\Delta\boldsymbol{\Omega} = \boldsymbol{\Omega}_m - \boldsymbol{\Omega}_f$.

The rotation of the fluid core is a crucial component of this formulation. To determine $\boldsymbol{\Omega}_f$, I rely on Busse's solution, which is applicable to axisymmetric spheroids (Busse, 1968). For this study, I consider the Earth as an axisymmetric spheroid, leading to a stationary solution for $\boldsymbol{\Omega}_f$ obtained in the precessing frame, which is attached to $\boldsymbol{\Omega}_p$. Finally, the relation between the two reference frames and the corresponding coordinate systems will also be introduced in the following section.

4.2.1 Precession-driven flow

In the precessing frame, I define the coordinate system $(\hat{\boldsymbol{X}}'_p, \hat{\boldsymbol{Y}}'_p, \hat{\boldsymbol{Z}}'_p)$ such that $\hat{\boldsymbol{Z}}'_p$ is aligned with $\boldsymbol{\Omega}_m$ and $\hat{\boldsymbol{X}}'_p$ is in the direction of $\boldsymbol{\Omega}_p$ (see Figure 4.1). Note that $\boldsymbol{\Omega}_m$ and $\boldsymbol{\Omega}_p$ point towards opposite hemispheres because the Earth's precession is in the retrograde direction. I adopt negative Ω_p so that the angle between $\hat{\boldsymbol{Z}}'_p$ and $\hat{\boldsymbol{k}}_p$ is α. The vector $\boldsymbol{\Omega}_f$ has co-latitude θ_f and longitude ϕ_f.

The Earth rotates with an angular velocity of $\Omega_m = 7.292 \times 10^{-5}\,\mathrm{rad\,s^{-1}}$, while simultaneously precessing around the ecliptic normal at an angle of $\alpha = 23.5°$ with $\Omega_p = -7.726 \times 10^{-12}\,\mathrm{rad\,s^{-1}}$. The rotation of the fluid core, with a viscosity of $\nu = 10^{-6}\,\mathrm{m^2\,s^{-1}}$, is coupled to the rotating mantle primarily through the pressure torque exerted at the flattened core-mantle boundary (CMB), which has a dynamical flattening $\epsilon_f = 2.6 \times 10^{-3}$.

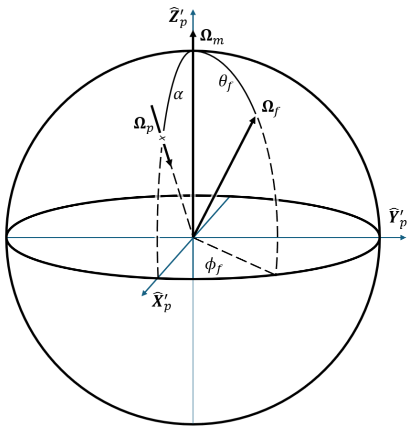

Figure 4.1: The coordinate system $(\hat{\boldsymbol{X}}'_p, \hat{\boldsymbol{Y}}'_p, \hat{\boldsymbol{Z}}'_p)$ in the precessing frame. The angles θ_f and ϕ_f are not to the scale for the case of the Earth.

Based on the implicit equation of Busse (1968), I obtain the solution of $\boldsymbol{\Omega}_f$ which has the angles $\theta_f = 1.62 \times 10^{-5}\,\mathrm{rad}$ and $\phi_f = \pi + 3.38 \times 10^{-5}\,\mathrm{rad}$ with respect to $\boldsymbol{\Omega}_m$. Boundary layer develops at the CMB. The boundary layer is expected to have a thickness of $L_\nu = \sqrt{\nu/\Omega_f} = 0.1\,\mathrm{m}$ if the flow is laminar and away from the location where the boundary layer breaks down. Under the no spin-up condition, the differential rotation is given by $\Delta\Omega = \Omega_m \sin\theta_f$. The differential velocity at the CMB, with $R = 3480\,\mathrm{km}$, is $U = \Delta\Omega R = 4.1 \times 10^{-3}\,\mathrm{m\,s^{-1}}$. With the boundary layer thickness and the differential velocity, the Reynolds number $Re = UL_\nu/\nu$ is approximately 500.

The solution of $\boldsymbol{\Omega}_f$ is calculated using Brent's method, a root-finding algorithm. This method is employed to find the root of the implicit equation for $\boldsymbol{\Omega}_f$ derived by Busse (1968). The value of θ_f obtained from this calculation aligns with similar results found in the literature. For instance, Tilgner (2015) provides a detailed calculation procedure for determining θ_f, while Buffett (2021) cites the value directly. These parameters, including θ_f and ϕ_f, are necessary for calculating the relevant forces that are implemented in the local box model.

4.2.2 Governing equations in fluid frame

In the fluid frame, I define two sets of coordinate system: One global $(\hat{\boldsymbol{X}}, \hat{\boldsymbol{Y}}, \hat{\boldsymbol{Z}})$ and the other is local $(\hat{\boldsymbol{x}}, \hat{\boldsymbol{y}}, \hat{\boldsymbol{z}})$ (see Figure 4.2). The origin of the global system is at the center of the Earth, while the one of the local system is on the CMB at $\boldsymbol{R}$. These coordinate systems not only connect the solution obtained in the precessing frame but also serve as the basis for the subsequent analysis.

For the global coordinate system, the origin is at the center of the outer core, with $\hat{\boldsymbol{Z}}$ aligned with $\boldsymbol{\Omega}_f$. The $\hat{\boldsymbol{X}}$ axis can be chosen arbitrarily; however, I choose it such that $\boldsymbol{\Omega}_m$ tilts toward negative $\hat{\boldsymbol{X}}$ at $t = 0$, with the tilt angle being θ_f. The local coordinate system is on the CMB with co-latitude θ and longitude ϕ. In this system, the $\hat{\boldsymbol{x}}$ axis is eastward, the $\hat{\boldsymbol{y}}$ axis is north-

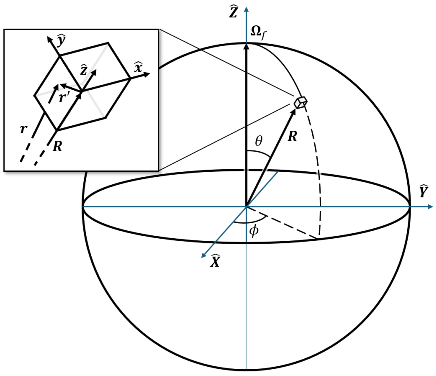

Figure 4.2: The coordinate system $(\hat{\boldsymbol{x}}, \hat{\boldsymbol{y}}, \hat{\boldsymbol{z}})$ in the fluid frame.

ward, and the $\hat{\boldsymbol{z}}$ axis is in radial outward direction. In order to bring the laminar solution into the local coordinate system, a series of coordinate transformations is needed, incorporating the Euler angles θ_f and ϕ_f. I will present the explicit expressions for these transformations in the following sections (see Section 4.3.1).

In the fluid frame, the governing equation for the fluid motion $\boldsymbol{u}$ is given by

$$\frac{\partial \boldsymbol{u}}{\partial t} + \boldsymbol{u} \cdot \nabla \boldsymbol{u} = -\frac{1}{\rho}\nabla P + \nu \nabla^2 \boldsymbol{u} - 2\left(\boldsymbol{\Omega}_f + \boldsymbol{\Omega}_p\right) \times \boldsymbol{u} - \left(\boldsymbol{\Omega}_p \times \boldsymbol{\Omega}_f\right) \times \boldsymbol{r} \tag{4.1}$$

where ρ is the fluid density. Since the reference frame is not fixed in the inertial space, there are noninertial terms appeared in the equation, such as the centrifugal, Coriolis, and Euler forces. The centrifugal force is absorbed in the pressure term. The third term on the right hand side is the Coriolis force and the last term is the Euler force, which is due to the angular acceleration of the reference frame. The vector $\boldsymbol{r}$ in general describes the position of any fluid in the core. For the fluid motion near the CMB, I divide $\boldsymbol{r}$ into two parts, $\boldsymbol{R} + \boldsymbol{r}'$, where $\boldsymbol{r}'$ is the position vector originating from the local coordinate system. Given that $\boldsymbol{r}' \ll \boldsymbol{R}$, the Euler force is dominated by $-\left(\boldsymbol{\Omega}_p \times \boldsymbol{\Omega}_f\right) \times \boldsymbol{R}$.

Moreover, in the fluid frame, the differential rotation of the mantle $\Delta\boldsymbol{\Omega}$ drives the fluid motion. The boundary velocity $\boldsymbol{u}_{\mathrm{B}} = \Delta\boldsymbol{\Omega} \times \boldsymbol{R}$ in the local coordinate system is given by

$$u_{\mathrm{B},x} = U \cos\theta \cos(\Omega_f t + \phi) \tag{4.2a}$$

$$u_{\mathrm{B},y} = -U \sin(\Omega_f t + \phi) \tag{4.2b}$$

$$u_{\mathrm{B},z} = 0 \tag{4.2c}$$

The longitude ϕ can be interpreted as a phase shift in time. For the sake of brevity in the following discussion, we set $\phi = 0$.

4.3 Local box model

I modify the local box model developed in Chapter 2 (see Page 20 for more details) to study boundary roughness. Here I summarize the primary features of such model and highlight several aspects relevant to the following discussion on roughness. The box model was designed to study the boundary layer of precession-driven flow, allowing the simulation to reach parameter regimes relevant to the Earth. Originally, the solid-liquid boundary was flat, but in this chapter I introduce a method to incorporate roughness on the boundary and study its effects on the flow.

It is important to note that the design of the box model places limitations on the roughness that can be studied. First, the length scale of the roughness, both in amplitude and wavelength, needs to be of the same order of magnitude as the boundary layer thickness since the box model is defined in the unit of the thickness. Furthermore, the model requires periodic boundary conditions to be applied to the four lateral boundaries, which limits the geometry of the roughness since it has to be similarly periodic. The velocity assigned at the top boundary to mimic precession-driven flow further complicates the implementation of roughness, as will be elaborated upon in the following sections.

The box model is defined in the local coordinate system $(\hat{\boldsymbol{x}}, \hat{\boldsymbol{y}}, \hat{\boldsymbol{z}})$, located at $\boldsymbol{R}$ on the core-mantle boundary. Here, $\hat{\boldsymbol{z}}$ corresponds to the wall-normal (vertical) direction, while $\hat{\boldsymbol{x}}$ and $\hat{\boldsymbol{y}}$ correspond to the wall-parallel (horizontal) directions. The governing equation is non-dimensionalized using the differential velocity U, the boundary layer thickness L_ν, and the corresponding time scale $T = L_\nu/U$. Consequently, Equation 4.1 becomes:

$$\frac{\partial \boldsymbol{u}^*}{\partial t^*} + \boldsymbol{u}^* \cdot \nabla^* \boldsymbol{u}^* = -\nabla^* P^* + \frac{1}{Re} \nabla^{*2} \boldsymbol{u}^* + \boldsymbol{f}^*_{\text{Coriolis}} + \boldsymbol{f}^*_{\text{Euler}} \tag{4.3a}$$

where

$$\boldsymbol{f}^*_{\text{Coriolis}} = -\frac{2}{Re} \left[\hat{\boldsymbol{k}}_f + Po \left(\frac{\Omega_m}{\Omega_f} \right) \hat{\boldsymbol{k}}_p \right] \times \boldsymbol{u}^* \tag{4.3b}$$

and

$$\boldsymbol{f}^*_{\text{Euler}} = -\left(\frac{L_\nu}{R} \right) \left(\frac{\Omega_m}{\Delta\Omega} \right)^2 Po \left(\frac{\Omega_f}{\Omega_m} \right) \left(\hat{\boldsymbol{k}}_p \times \hat{\boldsymbol{k}}_f \right) \times \left[\left(\frac{L_\nu}{R} \right) \boldsymbol{r}'^* + \hat{\boldsymbol{R}} \right] \tag{4.3c}$$

Note that $Re = UL_\nu/\nu$ is the Reynolds number, and $Po = \Omega_p/\Omega_m$ is the Poincaré number. A superscript $(^*)$ denotes dimensionless variables in the units of U, L_ν, and T. Additionally, $\hat{\boldsymbol{R}} = \boldsymbol{R}/R$ is a unit vector.

The coefficients of both $\boldsymbol{f}^*_{\text{Coriolis}}$ and $\boldsymbol{f}^*_{\text{Euler}}$ for the Earth can be found in Table 1.1 and Table 1.1, or they can be evaluated from the parameters therein. The ratio Ω_m/Ω_f can be expressed as $1/\cos\theta_f$ under the no spin-up condition. Given the smallness of θ_f, the ratio is close to unity, differing by approximately $O(10^{-10})$. Therefore, the ratio is set to one. The coefficient of $\boldsymbol{f}^*_{\text{Euler}}$ is approximately 1.36×10^{-5}. Given that $L_\nu/R \approx O(10^{-8})$, the Euler force is dominated by the term proportional to $(\hat{\boldsymbol{k}}_p \times \hat{\boldsymbol{k}}_f) \times \hat{\boldsymbol{R}}$. In this study, except for the term associated with $\boldsymbol{r}'^*$, the Coriolis and the Euler forces are implemented with the aforementioned coefficients.

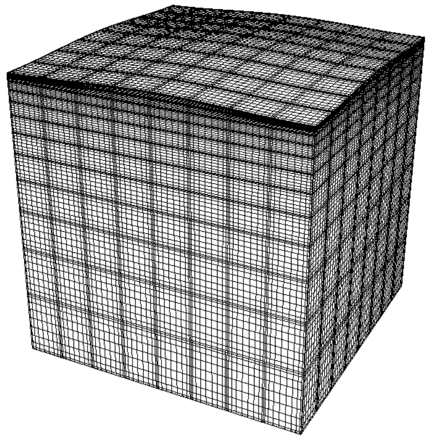

Figure 4.3: Local box model with roughness. In the unit of L_ν, the domain size is $30 \times 30 \times 30$ and the roughness height is $H^* = 0.5$.

The governing equation is solved using Nek5000[1], an open-source computational fluid dynamic code based on the spectral element method. This method combines the advantages of spectral methods, giving us the accuracy that we require, and finite element methods, giving us the flexibility to model the complex shape of the boundary (Patera, 1984). In a spectral element method, the computation domain is divided into E deformable hexahedral elements, within which data are represented using Nth-order tensor-product polynomials. For this study, I use a rectangular domain of size $30 \times 30 \times 30$ in units of L_ν. The domain consists of $E = 768$ elements, with $N = 9$. To increase spatial resolution near the top boundary, where relevant flow dynamics in the boundary layer take place, the heights of the elements are smaller. The top boundary is solid (representing the CMB), with its velocity specified as to mimic the precessing mantle as seen from the fluid frame (see Equation 4.2). The four side boundaries are periodic. The bottom boundary is stress-free (i.e. no tangential stress) and the normal velocity is zero.

I use sinusoidal functions to approximate boundary roughness. Roughness height h is defined with respect to the $z = 0$ plane. The roughness profile is given by:

$$h^*(x^*, y^*) = -\frac{H^*}{2}\left(\cos k^* x^* + \cos k^* y^*\right) \tag{4.4}$$

where H^* is the maximum height and $k^* = 2\pi/\lambda^*$ is the wavenumber, with λ^* being the wavelength. In the context of the local box model, the wavelength is chosen to match the domain size, ensuring that the periodic boundary conditions are satisfied. The minus sign ensures that, within the range $[0, \lambda^*]$ for both x^* and y^*, the height h^* reaches its maximum at the center of the domain (see Figure 4.3).

[1]NEK5000 Version 20.0-dev. Argonne National Laboratory, Illinois. Available: https://nek5000.mcs.anl.gov.

4.3.1 Explicit expression for the precession vector

In this subsection, I derive the explicit expression of the precession vector $\hat{\boldsymbol{k}}_p$, which is necessary in the local box model to calculate the Coriolis and the Euler forces (refer to the governing equation of the model presented in Equation 4.3). The derivation begins with the conventional expression of $\hat{\boldsymbol{k}}_p$ in the precessing frame (e.g. Busse, 1968), followed by a series of coordinate transformations to obtain the expression required for the local model.

Coordinate transformations

In the precessing frame, the global coordinate system $(\hat{\boldsymbol{X}}'_p, \hat{\boldsymbol{Y}}'_p, \hat{\boldsymbol{Z}}'_p)$ is defined such that $\hat{\boldsymbol{k}}_m = \hat{\boldsymbol{Z}}'_p$ and $\hat{\boldsymbol{k}}_p = (\sin\alpha\,\hat{\boldsymbol{X}}'_p + \cos\alpha\,\hat{\boldsymbol{Z}}'_p)$. The subscript p denotes precession for both the rotation vector and the unit vectors of the coordinate system. The fluid rotation vector $\hat{\boldsymbol{k}}_f$ is described by two angles θ_f and ϕ_f with respect to $\hat{\boldsymbol{k}}_m$ (see Figure 4.4).

The local coordinate system $(\hat{\boldsymbol{x}}, \hat{\boldsymbol{y}}, \hat{\boldsymbol{z}})$ used for the box model is defined with respect to an intermediate coordinate system $(\hat{\boldsymbol{X}}, \hat{\boldsymbol{Y}}, \hat{\boldsymbol{Z}})$. This intermediate system is defined in the fluid frame, with $\hat{\boldsymbol{Z}}$ aligned with $\hat{\boldsymbol{k}}_f$. Note that the orientation of this intermediate system differs from $(\hat{\boldsymbol{X}}'_p, \hat{\boldsymbol{Y}}'_p, \hat{\boldsymbol{Z}}'_p)$, necessitating a series of rotations to align the system.

A two-step rotation is applied to align $\hat{\boldsymbol{Z}}'_p$ with $\hat{\boldsymbol{k}}_f$: (1) a counterclockwise rotation about $\hat{\boldsymbol{Z}}'_p$ by ϕ_f, and (2) a counterclockwise rotation about the intermediate axis $\hat{\boldsymbol{Y}}''_p$ by θ_f. The rotation matrices are given by (see e.g. Thornton & Marion, 2003):

$$\lambda_1 = \begin{pmatrix} \cos\phi_f & \sin\phi_f & 0 \\ -\sin\phi_f & \cos\phi_f & 0 \\ 0 & 0 & 1 \end{pmatrix} \tag{4.5}$$

and

$$\lambda_2 = \begin{pmatrix} \cos\theta_f & 0 & -\sin\theta_f \\ 0 & 1 & 0 \\ \sin\theta_f & 0 & \cos\theta_f \end{pmatrix} \tag{4.6}$$

Coordinate of a vector $\boldsymbol{x}$ in the new coordinate system $(\hat{\boldsymbol{X}}_p, \hat{\boldsymbol{Y}}_p, \hat{\boldsymbol{Z}}_p)$ is given by $[\boldsymbol{x}]_p = \lambda_2\lambda_1[\boldsymbol{x}]'_p$. The rotations are chosen so that $\hat{\boldsymbol{k}}_m$ lies in the $\hat{\boldsymbol{X}}_p$-$\hat{\boldsymbol{Z}}_p$ plane, leaning towards the negative $\hat{\boldsymbol{X}}_p$ with co-latitude θ_f.

Next, a transformation from the precessing frame to the fluid frame is given by (see e.g. Noir & Cébron, 2013)

$$\lambda_3 = \begin{pmatrix} \cos\Omega_f t & \sin\Omega_f t & 0 \\ -\sin\Omega_f t & \cos\Omega_f t & 0 \\ 0 & 0 & 1 \end{pmatrix} \tag{4.7}$$

After this transformation, the new coordinate system is denoted as $(\hat{\boldsymbol{X}}, \hat{\boldsymbol{Y}}, \hat{\boldsymbol{Z}})$. This matrix indicates that any vector (except the one aligned with $\hat{\boldsymbol{Z}}$) which is fixed in the precessing frame traces a circular path around $\hat{\boldsymbol{k}}_f$ in the retrograde direction in the fluid frame.

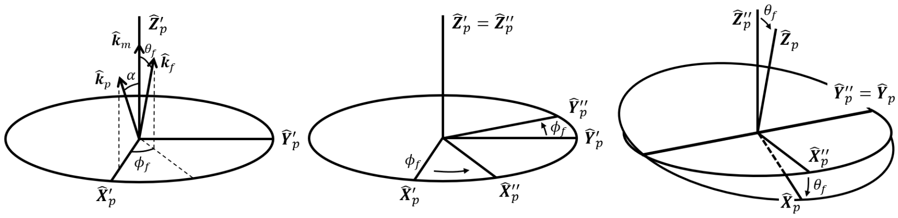

Figure 4.4: Two-step rotation to align $\hat{\boldsymbol{Z}}_p'$ with $\boldsymbol{\Omega}_f$.

Finally, the relation between the global coordinate system and the local coordinate system $(\hat{\boldsymbol{x}}, \hat{\boldsymbol{y}}, \hat{\boldsymbol{z}})$ is given by

$$\begin{cases} \hat{\boldsymbol{X}} = \sin\theta\cos\phi\,\hat{\boldsymbol{r}} + \cos\theta\cos\phi\,\hat{\boldsymbol{\theta}} - \sin\phi\,\hat{\boldsymbol{\phi}} \\ \hat{\boldsymbol{Y}} = \sin\theta\sin\phi\,\hat{\boldsymbol{r}} + \cos\theta\sin\phi\,\hat{\boldsymbol{\theta}} + \cos\phi\,\hat{\boldsymbol{\phi}} \\ \hat{\boldsymbol{Z}} = \cos\theta\,\hat{\boldsymbol{r}} - \sin\theta\,\hat{\boldsymbol{\theta}} \end{cases} \tag{4.8}$$

where $\hat{\boldsymbol{r}} = \hat{\boldsymbol{z}}$, $\hat{\boldsymbol{\theta}} = -\hat{\boldsymbol{y}}$, and $\hat{\boldsymbol{\phi}} = \hat{\boldsymbol{x}}$. The co-latitude θ and longitude ϕ are defined with respect to $(\hat{\boldsymbol{X}}, \hat{\boldsymbol{Y}}, \hat{\boldsymbol{Z}})$. A straightforward test can be done by checking if the fluid rotation vector $\hat{\boldsymbol{k}}_f$ is aligned with $\hat{\boldsymbol{Z}}$, as required. The coordinates of $\hat{\boldsymbol{k}}_f$ in the $(\hat{\boldsymbol{X}}_p', \hat{\boldsymbol{Y}}_p', \hat{\boldsymbol{Z}}_p')$ system are given by

$$\hat{\boldsymbol{k}}_f = \left(\sin\theta_f\cos\phi_f\,\hat{\boldsymbol{X}}_p' + \sin\theta_f\sin\phi_f\,\hat{\boldsymbol{Y}}_p' + \cos\theta_f\,\hat{\boldsymbol{Z}}_p'\right), \tag{4.9}$$

while in the local coordinate system $(\hat{\boldsymbol{x}}, \hat{\boldsymbol{y}}, \hat{\boldsymbol{z}})$ are

$$\hat{\boldsymbol{k}}_f = (\sin\theta\,\hat{\boldsymbol{y}} + \cos\theta\,\hat{\boldsymbol{z}})\,. \tag{4.10}$$

Precession vector

In order to obtain the coordinates of $\hat{\boldsymbol{k}}_p$ in the $(\hat{\boldsymbol{X}}, \hat{\boldsymbol{Y}}, \hat{\boldsymbol{Z}})$ system, I first write the coordinates of $\hat{\boldsymbol{k}}_p$ in the $(\hat{\boldsymbol{X}}_p', \hat{\boldsymbol{Y}}_p', \hat{\boldsymbol{Z}}_p')$ system as a column matrix, and then apply the transformation matrices λ_1, λ_2, and λ_3 in sequence. Finally, I apply the relation given in Equation 4.8 to transform the coordinates to the local coordinate system $(\hat{\boldsymbol{x}}, \hat{\boldsymbol{y}}, \hat{\boldsymbol{z}})$. The final result is given by:

$$\begin{aligned} \hat{\boldsymbol{k}}_p \cdot \hat{\boldsymbol{x}} \equiv k_{p,x} = \Big[& -\sin(\alpha)\sin(\phi_f)\cos(\Omega_f t + \phi) \\ & -\sin(\alpha)\sin(\Omega_f t + \phi)\cos(\phi_f)\cos(\theta_f) \\ & +\sin(\theta_f)\sin(\Omega_f t + \phi)\cos(\alpha)\Big] \end{aligned} \tag{4.11a}$$

$$\begin{aligned} \hat{\boldsymbol{k}}_p \cdot \hat{\boldsymbol{y}} \equiv k_{p,y} = \Big[& \sin(\alpha)\sin(\phi_f)\sin(\Omega_f t + \phi)\cos(\theta) \\ & +\sin(\alpha)\sin(\theta)\sin(\theta_f)\cos(\phi_f) \\ & -\sin(\alpha)\cos(\phi_f)\cos(\theta)\cos(\theta_f)\cos(\Omega_f t + \phi) \\ & +\sin(\theta)\cos(\alpha)\cos(\theta_f) \\ & +\sin(\theta_f)\cos(\alpha)\cos(\theta)\cos(\Omega_f t + \phi)\Big] \end{aligned} \tag{4.11b}$$

$$\hat{\boldsymbol{k}}_p \cdot \hat{\boldsymbol{z}} \equiv k_{p,z} = \Big[-\sin(\alpha)\sin(\phi_f)\sin(\theta)\sin(\Omega_f t+\phi) \\ +\sin(\alpha)\sin(\theta)\cos(\phi_f)\cos(\theta_f)\cos(\Omega_f t+\phi) \\ +\sin(\alpha)\sin(\theta_f)\cos(\phi_f)\cos(\theta) \\ -\sin(\theta)\sin(\theta_f)\cos(\alpha)\cos(\Omega_f t+\phi) \\ +\cos(\alpha)\cos(\theta)\cos(\theta_f)\Big] \tag{4.11c}$$

It can be checked that $\hat{\boldsymbol{k}}_p$ is a unit vector by $(k_{p,x})^2 + (k_{p,y})^2 + (k_{p,z})^2 = 1$. Substitute the parameters $(\alpha, \theta_f, \phi_f)$ for the Earth, Equation 4.11 becomes

$$k_{p,x} = -0.40\sin(\Omega_f t+\phi) - 1.35\times10^{-5}\cos(\Omega_f t+\phi) \tag{4.12a}$$

$$k_{p,y} = 0.92\sin(\theta) + 1.35\times10^{-5}\sin(\Omega_f t+\phi)\cos(\theta) \\ -0.40\cos(\theta)\cos(\Omega_f t+\phi) \tag{4.12b}$$

$$k_{p,z} = -1.35\times10^{-5}\sin(\theta)\sin(\Omega_f t+\phi) \\ +0.40\sin(\theta)\cos(\Omega_f t+\phi) + 0.92\cos(\theta) \tag{4.12c}$$

Note that the coefficients of $\hat{\boldsymbol{k}}_p$ depend on the position of the local coordinate system. For example, at $\theta = 0$, the vector traces a circular cone around $\hat{\boldsymbol{z}}$ with an angle of approximately 23.5° to $\hat{\boldsymbol{z}}$. Conversely, at $\theta = 90°$, the revolving axis shifts to $\hat{\boldsymbol{y}}$. Equation 4.12 is used to calculate $\boldsymbol{f}^*_{\text{Coriolis}}$ and $\boldsymbol{f}^*_{\text{Euler}}$ in the local box model for the Earth.

4.3.2 Implementation of roughness

To conform to the roughness profile (Equation 4.4), I generate the mesh of the model by first creating a square rectangular cube and then deforming the coordinates of certain grid points. The coordinates along $\hat{\boldsymbol{z}}$ axis of the grid points in the cube are z_{old}. The original grid points with z_{old} are assigned to new coordinates given by $z_{\text{new}} = z_{\text{old}} + dz$. The displacement is defined as $dz = (z_{\text{old}} + 1)h$ for $z_{\text{old}} \geq -1$. For example, at the grid points on the top boundary where $z_{\text{old}} = 0$, the displacement equals the height given by Equation 4.4, resulting in $z_{\text{new}} = h(x, y)$ as a function of x and y. The displacement decreases with increasing depth and reaches zero at $z = -1$. The grid points below remain at their original positions. The depth of zero displacement is chosen to ensure that the roughness within the boundary layer is accurately modeled while maintaining the regular structure of the grid points below.

The assigned velocity at the top boundary implies that the boundary roughness changes in time (see the boundary velocity given in Equation 4.2). In order to model this moving roughness, we first derive the temporal evolution of the roughness profile and then assign the time-varying mesh deformation to the model during simulation. To derive the temporal evolution of the roughness profile, we begin by determining the trajectory of a given point (x, y) on the boundary. Using the boundary velocity, the trajectory is obtained through time integration:

$$x(t) = \frac{U}{\Omega_f}\cos\theta\sin(\Omega_f t) + x_0 \tag{4.13a}$$

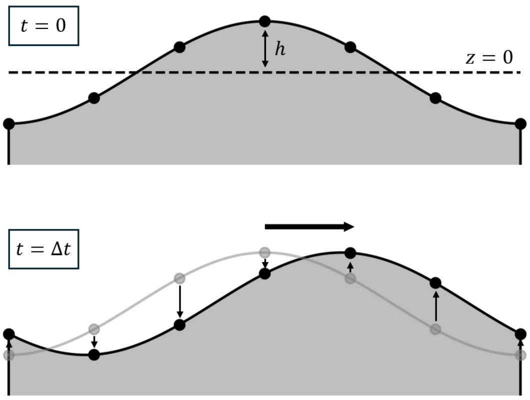

Figure 4.5: Schematic diagrams of the moving roughness. Upper panel: initial profile at $t = 0$. Lower panel: profile after a time interval Δt. The shaded region represents the fluid. The horizontal shift of the profile corresponds to the vertical movements of individual grid points on the boundary.

$$y(t) = \frac{U}{\Omega_f}\left[\cos(\Omega_f t) - 1\right] + y_0 \tag{4.13b}$$

where (x_0, y_0) are the coordinates at $t = 0$. Substitute (x, y) in Equation 4.4, which represents the initial profile at $t = 0$, with (x_0, y_0). We obtain the temporal evolution of the roughness profile:

$$\begin{aligned} h(x,y,t) = -\frac{H}{2}\Bigg[&\cos\left(kx - k\frac{U}{\Omega_f}\cos\theta\sin(\Omega_f t)\right) \\ &+ \cos\left(ky - k\frac{U}{\Omega_f}\left[\cos(\Omega_f t) - 1\right]\right)\Bigg] \end{aligned} \tag{4.14}$$

The time-dependent terms can be interpreted as the phase shift, causing the entire topography to shift horizontally. Alternatively, considering the height of a specific point, the variation will oscillate over time.

Figure 4.5 presents schematic diagrams of the moving roughness. The upper panel shows the initial profile at $t = 0$, described by a cosine function with a single wavelength. The height is defined with respect to the $z = 0$ plane. The shaded region represents the fluid. After a time interval Δt (lower panel), the profile shifts horizontally, resulting in vertical movements of individual grid points on the boundary.

In Nek5000, mesh deformation can be specified through a mesh velocity. For our case, the mesh velocity corresponding to the moving roughness is derived from the temporal evolution of the roughness profile given in Equation 4.14. The mesh velocity in the vertical direction is equal to the time derivative of the roughness profile:

$$\frac{\partial h}{\partial t} = -\frac{H}{2}\Bigg[k\,U\cos\theta\cos\left(\Omega_f t\right)\sin\left(kx - k\frac{U}{\Omega_f}\cos\theta\sin(\Omega_f t)\right) \\ - k\,U\sin\left(\Omega_f t\right)\sin\left(ky - k\frac{U}{\Omega_f}\Big[\cos(\Omega_f t) - 1\Big]\right)\Bigg] \tag{4.15}$$

Steady streaming

In this subsection, I compare qualitatively my result with a previous one in the literature to make sure that the method works as expected. To facilitate this comparison, certain modifications were made to the model. These modifications are only relevant to the results presented in this subsection or as explicitly stated elsewhere. One aspect that remains unchanged is the implementation of the moving roughness, which is achieved by deforming the mesh during simulation through the assignment of mesh velocity.

First, let's consider a simplified version of the system discussed in the main text, excluding Coriolis and Euler forces. The flow is governed by inertial force, pressure, and viscous force, with the boundary executing a simple harmonic oscillation in its own plane. This scenario, with a flat boundary, is a classic example found in fluid mechanics textbooks (see, for example, Section 24 of Landau & Lifshitz, 1987). The boundary layer formed in this case is also known as the Stokes boundary layer.

Suppose that that the solid-liquid boundary is not flat but features roughness or topography. Relevant studies in the literature discuss wave ripples (or sand ripples) found at the bottom of sea waves in shallow waters. These wave ripples typically manifest as periodic ridges perpendicular to the wave propagation direction. Experimental and theoretical studies have shown that the formation of wave ripples is related to the oscillatory motion of the bottom fluid (e.g. Sleath, 1976; Kaneko & Honji, 1979). According to the theory presented by Blondeaux (1990), an oscillatory flow interacting with a small-amplitude wavy bottom generates circulating cells (also known as steady streaming), which under certain circumstances, facilitate ripple formation. Figure 4.6 shows an example of steady streaming where the flow near the perturbed boundary is directed from the troughs towards the crests of the perturbation. It is important to note that the figure illustrates the steady part of the velocity field, while the time-dependent part oscillates accordingly.

The governing equation is modified for a simple oscillatory flow without precession nor rotation, described by

$$\frac{\partial \boldsymbol{u}}{\partial t} + \boldsymbol{u}\cdot\nabla\boldsymbol{u} = -\nabla P + \nu\,\nabla^2\boldsymbol{u} \tag{4.16}$$

The boundary velocity is given by:

$$u_{\mathrm{B},y} = -U\sin(\omega t) \tag{4.17}$$

where U is the maximum velocity amplitude and ω is the oscillation frequency. The other velocity components are zero. The Stokes-layer thickness is defined as $L_\delta = \sqrt{2\nu/\omega}$. Using the velocity scale U and the length scale L_δ, the Reynolds number is defined as $Re_\delta = UL_\delta/\nu$. To avoid confusion with the non-dimensional variables introduced in the main text, variables in this subsection will be presented with explicit expressions, such as y/L_δ.

The initial roughness profile is given by:

$$h(x, y) = -H\cos(ky) \tag{4.18}$$

where H is the maximum amplitude and $k = 2\pi/\lambda$ is the wavenumber, with λ being the wavelength. The y-coordinate of a point on the moving boundary is obtained by integrating Equation 4.17 in time:

$$y(t) = \frac{U}{\omega}\Big[\cos(\omega t) - 1\Big] + y_0 \tag{4.19}$$

where y_0 is the coordinate at $t = 0$. By substituting y in Equation 4.18 by y_0, the temporal evolution of the roughness profile is obtained:

$$h(x, y, t) = -H\cos\left(ky - k\frac{U}{\omega}\Big[\cos(\omega t) - 1\Big]\right) \tag{4.20}$$

Mesh deformation is specified through mesh velocity, which is equal to $\partial h/\partial t$.

Simulation begins with $\boldsymbol{u} = 0$ everywhere in the domain. To allow the solution to reach a steady state, the simulation runs for 25 oscillation cycles. Data are collected during the last cycle, with 20 snapshots of the velocity field stored for post-processing. To obtain the pattern of steady streaming, I choose a vertical plane parallel to the oscillation direction at the center of the domain. The roughness profile at $t = 0$ serves as the basis for averaging. At each time step, the solution is transformed so that the roughness profile matches that at $t = 0$. The solutions from individual snapshots are then interpolated onto the same grid points, and the time-averaged values are computed at each point. Finally, to reduce the influence of initial conditions, the result is further subtracted from the one with the same setup but without roughness (i.e. a flat boundary).

Figure 4.7 shows the result obtained from the local box model with the parameters $Re_\delta = 0.1$, $\lambda/L_\delta = 15.7$, and $H/L_\delta = 0.1$. Two circulating cells are observed, with their centers located between $z/L_\delta = -2$ and -3. The flow direction near the rough boundary is from trough to crest. Although the roughness profile is barely visible in the stream plot due to the small amplitude, it can be referred to in the upper panel of Figure 4.5 for clarity. Note that although a vertical plane at the center of the domain ($x = 7.85$) is chosen for the plot, similar results can be found at different x (not shown) due to the homogeneity along the x-direction. The qualitative agreement with the result presented in the literature (see Figure 4.6) supports the validity of the method, particularly the implementation of boundary roughness.

The mesh velocity assigned to represent the roughness movement is crucial in reproducing the correct pattern of steady streaming. For comparison, the result based on the same setup ($Re_\delta = 0.1$, $\lambda/L_\delta = 15.7$, and $H/L_\delta = 0.1$) but without assigning mesh velocity exhibits a different pattern (not shown

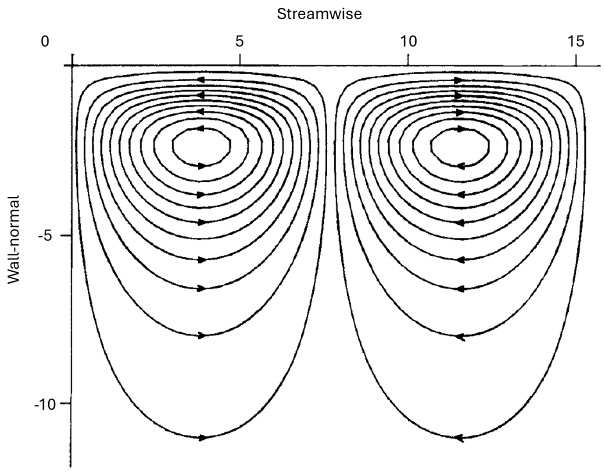

Figure 4.6: Steady streaming of the viscous oscillatory flow over a wavy wall ($Re_\delta = 0.1$ and $\lambda/L_\delta = 15.7$). The length unit is the Stokes-layer thickness L_δ. Figure adapted from Blondeaux (1990). Permission is granted at no cost for use of content in a Master's Thesis and/or Doctoral Dissertation.

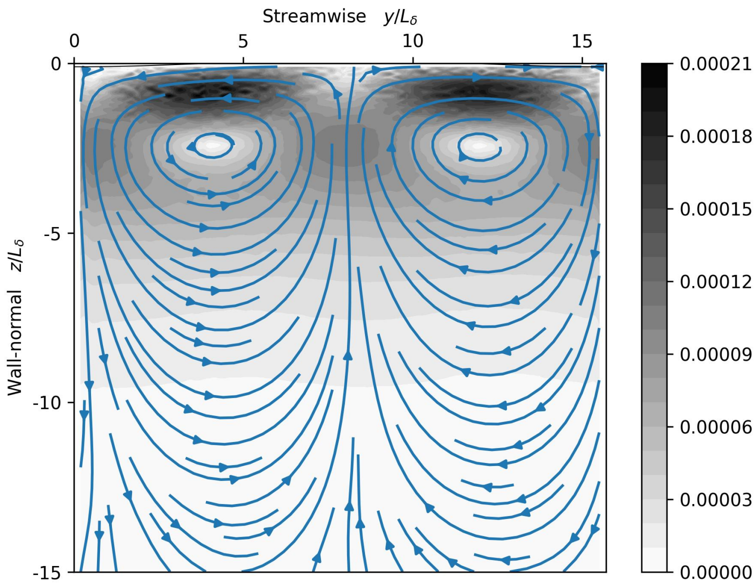

Figure 4.7: The time-averaged velocity field of the viscous oscillatory flow over a rough surface ($Re_\delta = 0.1$, $\lambda/L_\delta = 15.7$, and $H/L_\delta = 0.1$). Both the streamline and the amplitude (see the colorbar) are based on the velocity components u_y and u_z parallel to the shown plane.

here). In this case, the mesh was deformed before the simulation began and then remained unchanged. The steady part of the velocity field exhibits two circulating cells, but the direction near the roughness is from crest to trough. Although in this case the horizontal displacement of the roughness is small compared to the wavelength (i.e. the mesh deformation is barely visible), this comparison highlights the importance of mesh velocity. The horizontal displacement, U/ω (see Equation 4.19), in the unit of L_δ can be expressed as $U/(\omega L_\delta) = Re_\delta$, where the definitions of L_δ and Re_δ have been used.

The amplitude of roughness height does not significantly affects the pattern of steady streaming, although it does influence the velocity amplitude. A simulation with a similar setup ($Re_\delta = 0.1$ and $\lambda/L_\delta = 15.7$), but with a reduced roughness height of $H/L_\delta = 0.01$, exhibits a steady streaming pattern (not shown here) similar to that in Figure 4.7. However, the amplitude of vertical velocity component u_z/U is approximately one order of magnitude smaller than in the previous case where $H/L_\delta = 0.1$. This observation indicates that the roughness height primarily scales the intensity of the flow without significantly affecting the overall pattern.

4.3.3 Brief summary

In this study, I perform simulations with $Re = 500$ and $\theta = 0$, varying the roughness height H^* from 0.1 to 0.5. I set the wavelength of the roughness to $\lambda^* = 30$. Other wavelengths could be chosen, provided that the horizontal domain size is a multiple of λ^*. The boundary velocity $\boldsymbol{u}_\mathrm{B}$ is a critical factor in driving the fluid motion, so the oscillation cycles will be represented by $\Omega_f t$ in the discussion of temporal evolution. All simulations start with a perturbed velocity field which has root-mean-square amplitude of about 10^{-2} throughout the domain.

I conduct a spatial resolution test for the case with $H^* = 0.5$ by increasing the number of elements in the domain to $N = 1400$, nearly doubling the original resolution. The results show no significant changes, confirming that the initial resolution is sufficient.

4.4 Results

4.4.1 Force balance

Estimating the magnitude of each forcing term in the governing equation (Equation 4.3) provides insights into the force balance within the fluid. I calculate these terms using relevant quantities output from the solver, such as velocity and spatial derivatives at a given grid point. The temporal derivative of $\boldsymbol{u}^*$ is calculated using a second-order central difference:

$$\frac{\partial u_i^*}{\partial t^*} = \frac{u_i^*(t_{j+1}^*) - u_i^*(t_{j-1}^*)}{t_{j+1}^* - t_{j-1}^*} \tag{4.21}$$

where $i = x, y, z$ refers to the three velocity components and t_j^* represents the individual time steps. To distinguish the nonlinear term, I refer to $\partial \boldsymbol{u}^*/\partial t^*$ as

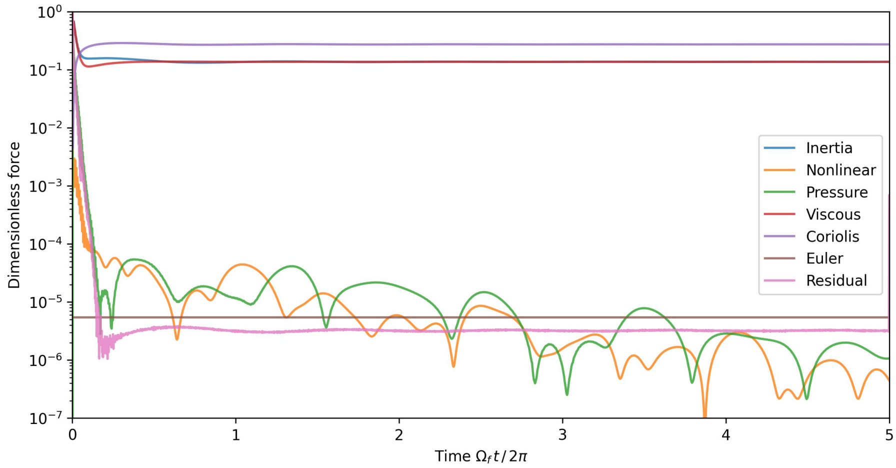

Figure 4.8: Dimensionless forces amplitude as a function of time at a single point $(x^*, y^*, z^*) = (15, 15, 0.5)$ for the case with $Re = 5$, $\theta = 0$, and $H^* = 0.0$. Inertia: $|\partial \boldsymbol{u}^*/\partial t^*|$, nonlinear: $|\boldsymbol{u}^* \cdot \nabla^* \boldsymbol{u}^*|$, pressure: $|\nabla^* P^*|$, viscous force: $|\frac{1}{Re}\nabla^{*2}\boldsymbol{u}^*|$, Coriolis force: $|\boldsymbol{F}^*_{\text{Coriolis}}|$, and Euler force: $|\boldsymbol{F}^*_{\text{Euler}}|$.

the inertial term. Figure 4.8 illustrates the magnitudes of the dimensionless forces as a function of time at a single point $(x^*, y^*, z^*) = (15, 15, 0.5)$ for the case with $Re = 5$, $\theta = 0$, and $H^* = 0.0$. In the laminar regime, the dominant forces are inertia, viscous, and Coriolis forces. The Euler force is at least four orders of magnitude smaller than the other terms. Note that the amplitude of the Euler force remains constant since it does not depend on the flow.

4.4.2 Effect of roughness

Let's first look at the thickness of boundary layer. Figure 4.9 presents the velocity profiles on the y-z plane at $x^* = 15$ for the case with $Re = 500$, $\theta = 0$, and $H^* = 0.5$. I choose the case for demonstration as the flow patterns are representative of the other cases with different H^* as well. The flow is mainly confined to the region above $z^* \approx -15$, although some flow persists below this level. Based on dimensional argument, the boundary layer thickness is supposed to be proportional to (e.g. Csanady, 1967)

$$\frac{u_\tau}{f} \tag{4.22}$$

where u_τ is friction velocity and f is the Coriolis parameter. In this study, I substitute f with $2\Omega_f \cos\theta$. The definition of friction velocity is $u_\tau = \sqrt{|\boldsymbol{\tau}_{\text{B}}|/\rho}$, where $|\boldsymbol{\tau}_{\text{B}}|$ is the magnitude of the shear stress on the boundary surface.

Shear stress on the boundary surface is defined as $\tau_{\text{B},i} = s_{ij}n_j$, where $s_{ij} = \mu(\partial_i u_j + \partial_j u_i)$ is the stress tensor and n_j (or in vector form $\hat{\boldsymbol{n}}$) is the unit normal vector on the surface. Expressed in the dimensionless form, the shear stress can be written as

$$\tau_{\text{B},i} = \rho U^2 \tau^*_{\text{B},i} \tag{4.23}$$

where

$$\tau^*_{\mathrm{B},i} = \left(\frac{1}{Re}\right)(\partial^*_i u^*_j + \partial^*_j u^*_i)n_j \tag{4.24}$$

Then, friction velocity can be derived directly from the numerical result via $u_\tau = U\sqrt{|\boldsymbol{\tau}^*_{\mathrm{B}}|}$.

Figure 4.10 shows the shear stress $\boldsymbol{\tau}^*_{\mathrm{B}}$ per unit area on the boundary surface. The horizontal components, $\tau^*_{\mathrm{B},x}$ and $\tau^*_{\mathrm{B},y}$, exhibit sinusoidal oscillations over time, with a frequency matching that of the boundary velocity. A phase difference of approximately $\pi/2$ exists between these components, suggesting that the amplitude of $[(\tau^*_{\mathrm{B},x})^2 + (\tau^*_{\mathrm{B},x})^2]^{1/2}$ should remain constant. The mean value within the interval $\Omega_f t/2\pi = [1.0, 5.0]$, where the solution reaches a statistically steady state, is $(3.33 \pm 0.13) \times 10^{-3}$. Table 4.1 summarizes the mean values for other cases of H^* within the same interval.

For laminar flow, the analytical expression for friction velocity is $u^{\mathrm{lam}}_\tau = Re^{-1/2}\,U$ (see e.g. Buffett & Christensen, 2007; Shih et al., 2023). Figure 4.11 shows the normalized friction velocity $u_\tau/u^{\mathrm{lam}}_\tau$ as a function of time for $Re = 500$ and $\theta = 0$ with roughness height H^* ranging from 0 to 0.5. The results indicate that roughness height does not significantly influence the magnitude of u_τ. For the case with $H^* = 0.5$, the mean value of $u_\tau/u^{\mathrm{lam}}_\tau$ between the interval $\Omega_f t/2\pi = [1.0, 5.0]$, where the solution reaches a statistically steady state, is 1.29 ± 0.03 (one standard deviation). The mean values for the other cases fall within the same range. Based on Equation 4.22, the boundary layer thickness for $Re = 500$ and $\theta = 0$ is about $14L_\nu$, consistent with the observation of the velocity profile on the y-z plane. In summary, the results suggest that roughness height does not significantly influence the shear stress on the boundary surface and the turbulent boundary layer thickness.

In the study by Buffett (2021), the reported value for $u_\tau/u^{\mathrm{lam}}_\tau$ is 1.2, without explicitly mentioning fluctuations in amplitude. An inspection of his time series plot for $u_\tau/u^{\mathrm{lam}}_\tau$ reveals variations in amplitude, with an estimated maximum of approximately 1.42 and a minimum of about 1.17 after the onset of turbulence. Averaging these extremes yields a value consistent with the range obtained in the present study. While this method of estimation is not precise, it provides a reasonable comparison, confirming that the results are in agreement.

Horizontal pressure drag arises when the boundary surface is not flat. Figure 4.12 shows the pressure field at $\Omega_f t/2\pi = 5.00$. On the top boundary, the pressure distribution aligns roughly along the y-axis, perpendicular to the corresponding boundary velocity, which at the given time points toward positive x-axis (see the fourth row of Figure 4.9). To calculate the pressure drag on the top boundary, I sum the local contributions, $P^*\hat{\boldsymbol{n}}$, and divide by the total area. Figure 4.13 displays the three components of the pressure drag per unit area, denoted as $(P^*_{\mathrm{B},x}, P^*_{\mathrm{B,y}}, P^*_{\mathrm{B,z}})$. For the vertical component, $P^*_{\mathrm{B},z}$ reaches a steady state, with a mean value of $(1.40 \pm 0.18) \times 10^{-3}$ within the interval $\Omega_f t/2\pi = [1.0, 5.0]$. The horizontal components, $P^*_{\mathrm{B},x}$ and $P^*_{\mathrm{B},y}$, exhibit similar temporal oscillations as the corresponding shear stress components, resulting in a mean value of $[(P^*_{\mathrm{B},x})^2 + (P^*_{\mathrm{B},y})^2]^{1/2}$ equal to $(1.65 \pm 0.39) \times 10^{-4}$. Table 4.1 summarizes the mean values for the other cases of H^*. The vertical component remains consistent across different values of H^*, while the horizontal compo-

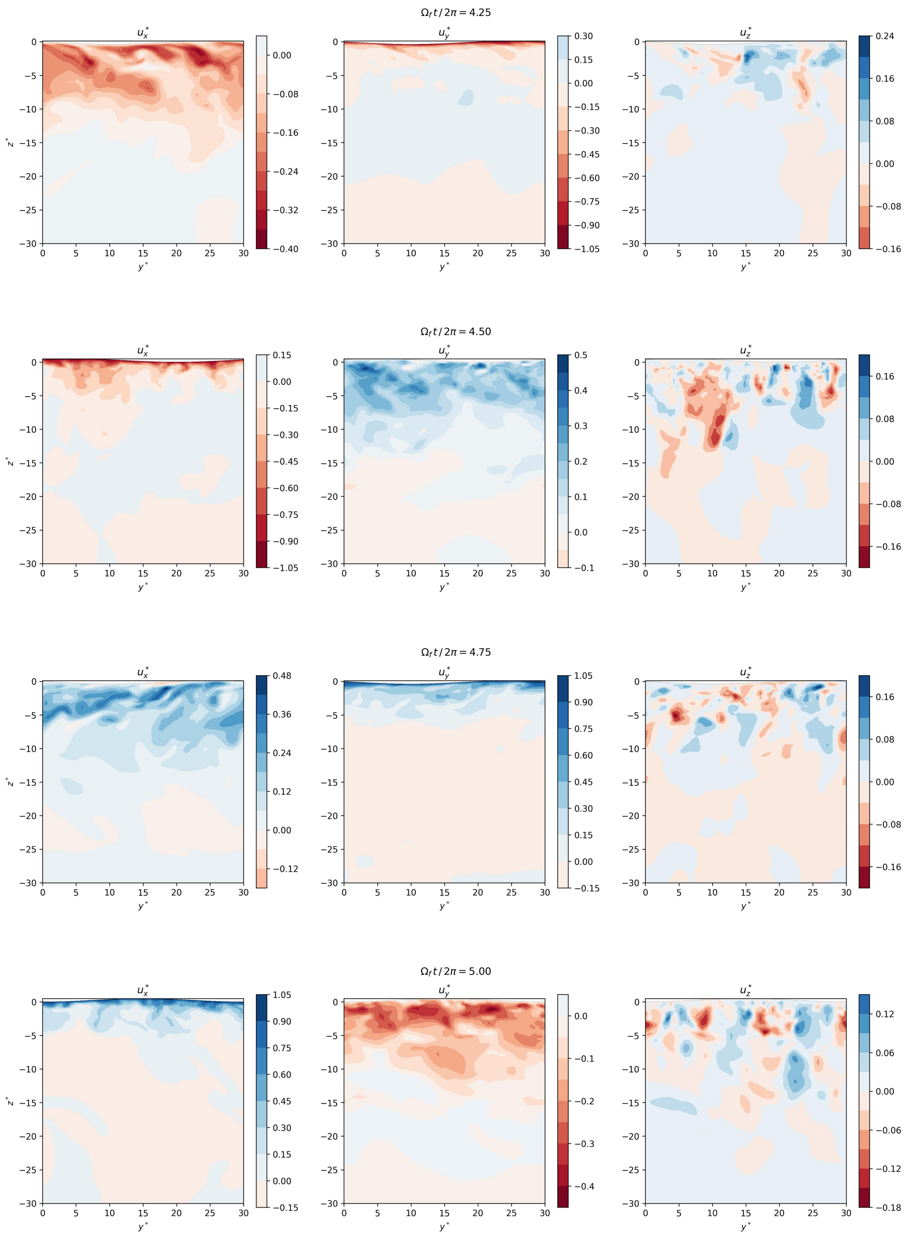

Figure 4.9: Velocity profiles at $x^* = 15$ for $Re = 500$, $\theta = 0$, and $H^* = 0.5$ at four different phases.

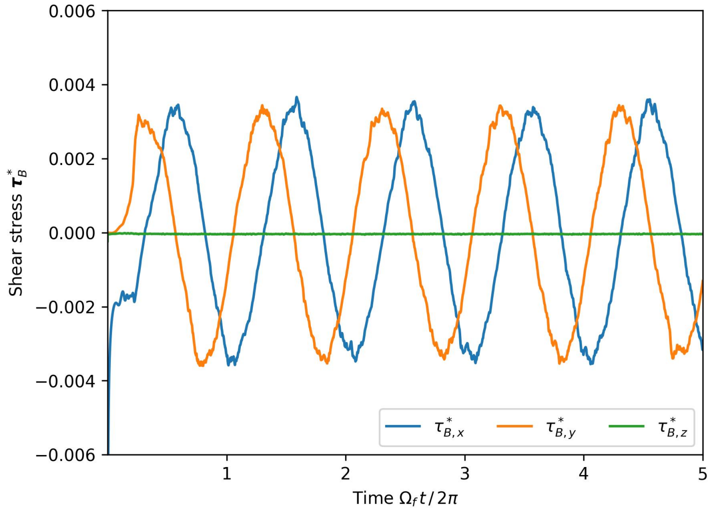

Figure 4.10: Shear stress $\boldsymbol{\tau}_{\mathrm{B}}^*$ per unit area on the boundary surface as a function of time for $Re = 500$, $\theta = 0$, and $H^* = 0.5$. A phase difference of approximately $\pi/2$ exists between $\tau_{\mathrm{B},x}^*$ and $\tau_{\mathrm{B},y}^*$. The mean value of $[(\tau_{\mathrm{B},x}^*)^2+(\tau_{\mathrm{B},x}^*)^2]^{1/2}$ within the interval $\Omega_f t/2\pi = [1.0, 5.0]$ is $(3.33 \pm 0.13) \times 10^{-3}$.

nents increase with H^*, showing a tenfold difference between $H^* = 0.1$ and 0.5.

In literature, shear stress is usually expressed in term of dimensionless coefficient (e.g. Sleath, 1987; Buffett & Christensen, 2007). Following the convention, I define the friction coefficient as

$$C_f = \frac{\sqrt{(\tau_{\mathrm{B},x})^2 + (\tau_{\mathrm{B},x})^2}}{\frac{1}{2}\rho U^2} \tag{4.25}$$

and similarly the drag coefficient as

$$C_d = \frac{\sqrt{(P_{\mathrm{B},x})^2 + (P_{\mathrm{B},y})^2}}{\frac{1}{2}\rho U^2} \tag{4.26}$$

where U is the far-field velocity relative to the boundary. Note that ρU^2 is the unit of non-dimensionalized shear stress and the pressure in the present study, so both coefficients are simply two times the corresponding values presented in Table 4.1. Figure 4.14 shows C_f and C_d as a function of H^*.

4.5 Discussion and Conclusions

In this study, I implement boundary roughness on a moving boundary. The implementation relies on the time-dependent deforming mesh. Validation of this method was examined by reproducing a well-studied case of oscillatory

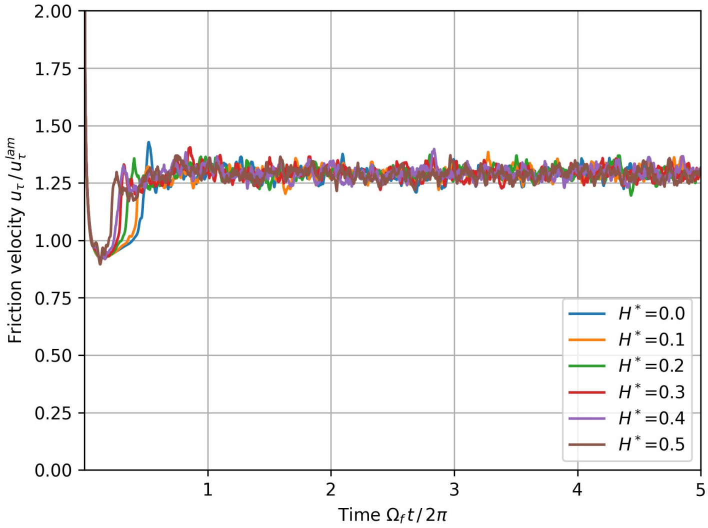

Figure 4.11: Friction velocity $u_\tau/u_\tau^{\text{lam}}$ as a function of time for $Re = 500$ and $\theta = 0$ with roughness height h^* from 0 to 0.5.

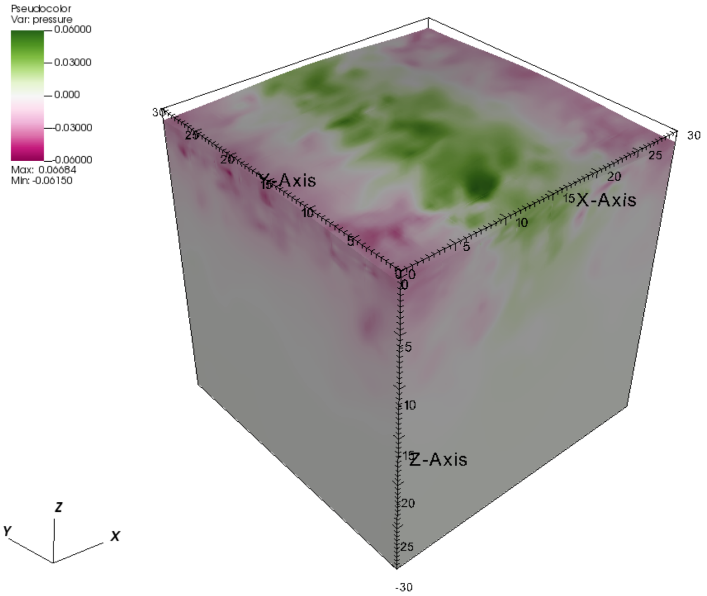

Figure 4.12: Pressure field P^* at $\Omega_f t/2\pi = 5.00$ for $Re = 500$, $\theta = 0$, and $H^* = 0.5$

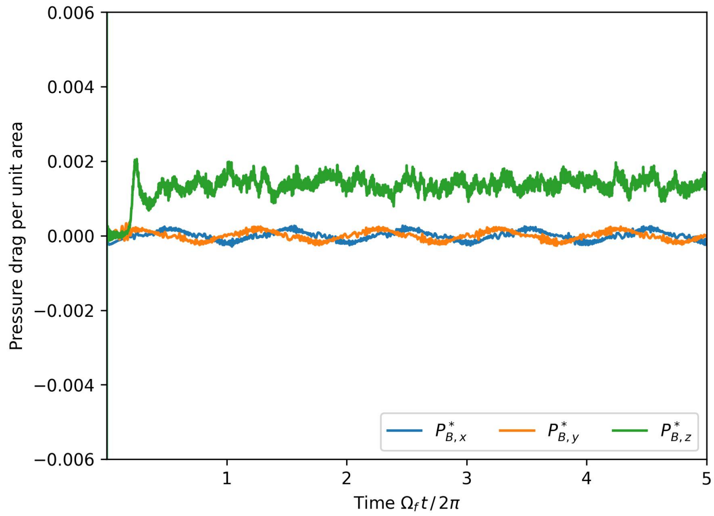

Figure 4.13: Pressure drag per unit area ($P^*_{\mathrm{B},x}, P^*_{\mathrm{B,y}}, P^*_{\mathrm{B},z}$) on the boundary surface as a function of time for $Re = 500$, $\theta = 0$, and $H^* = 0.5$.

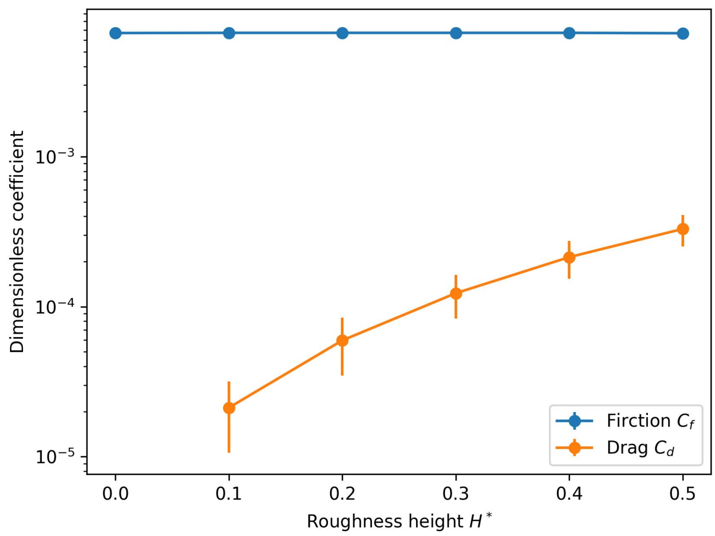

Figure 4.14: Friction coefficient C_f and drag coefficient C_d as a function of roughness height H^*. Note that $C_d = 0$ at $H^* = 0$ is not shown on the plot.

Table 4.1: Shear stress $\boldsymbol{\tau}_{\mathrm{B}}$ and pressure P^* on the boundary surface within the interval $\Omega_f t/2\pi = [1.0, 5.0]$.

h^*	$[(\tau^*_{\mathrm{B},x})^2 + (\tau^*_{\mathrm{B},x})^2]^{1/2}$	$\tau_{\mathrm{B},z}$	$[(P^*_x)^2 + (P^*_y)^2]^{1/2}$	P^*_z
0.0	$(3.34 \pm 0.14) \times 10^{-3}$	$(-1.25 \pm 1.31) \times 10^{-7}$	0	$(1.30 \pm 0.15) \times 10^{-3}$
0.1	$(3.35 \pm 0.14) \times 10^{-3}$	$(-1.68 \pm 0.86) \times 10^{-6}$	$(1.06 \pm 0.53) \times 10^{-5}$	$(1.34 \pm 0.17) \times 10^{-3}$
0.2	$(3.35 \pm 0.13) \times 10^{-3}$	$(-6.16 \pm 1.75) \times 10^{-6}$	$(2.98 \pm 1.24) \times 10^{-5}$	$(1.34 \pm 0.18) \times 10^{-3}$
0.3	$(3.35 \pm 0.14) \times 10^{-3}$	$(-1.39 \pm 0.26) \times 10^{-5}$	$(6.15 \pm 1.98) \times 10^{-5}$	$(1.35 \pm 0.18) \times 10^{-3}$
0.4	$(3.35 \pm 0.14) \times 10^{-3}$	$(-2.44 \pm 0.35) \times 10^{-5}$	$(1.07 \pm 0.30) \times 10^{-4}$	$(1.38 \pm 0.20) \times 10^{-3}$
0.5	$(3.33 \pm 0.13) \times 10^{-3}$	$(-3.77 \pm 0.46) \times 10^{-5}$	$(1.65 \pm 0.39) \times 10^{-4}$	$(1.40 \pm 0.18) \times 10^{-3}$

flow over a wavy surface. Nevertheless, concerning the roughness effect on the boundary layer of the oscillatory Ekman layer, the result shows that, for small-amplitude roughness, the horizontal components of the surface shear stress remain while those of the pressure exerted on the surface increase with roughness height. The roughness heights considered in this study are smaller than the boundary layer thickness expected in the laminar regime. Depending on the roughness height, three roughness regimes are defined: hydraulically smooth, transitionally rough, and fully rough (see e.g. the review by Kadivar et al., 2021). The distinction among the three regimes is related to the drag on the rough surface. In the hydraulically smooth regime, the drag is not modified. In the transitionally rough regime, the drag is influenced by both the Reynolds number and the roughness, while in the fully rough regime the drag becomes independent of the viscous effect (Reynolds number). The critical roughness height depends on the roughness type.

Another focus of the present study is the Euler force considered in the oscillatory Ekman layer. I derive the explicit expression for the Euler force by considering the precession vector within the local coordinate system in the fluid frame. I choose to formulate the problem in the fluid frame in order to focus on the fluid motion near the boundary. This formulation preserves the Euler force in the governing equations. In contrast, the formulation by Buffett (2021) is based on the mantle frame, where the precession-driven flow is initially solved under the assumption of an inviscid fluid core. Viscosity is later introduced as a correction for the boundary layer, which results in the Euler force being omitted from the governing equations. Nevertheless, based on the magnitude estimation, the Euler force is at least two orders smaller than the other forces, suggesting the resemblance between the two formulations under the conditions related to Earth's precession.

In literature, oscillatory flow can also be simulated by introducing a body force to drive the oscillation while keeping the boundary steady (e.g. Önder & Yuan, 2019). Although this alternative method offers a different numerical implementation, its consistency with the overall formulation requires careful assessment. Another issue with the fluid-driving scheme concerns the Coriolis force. Preliminary simulations indicate that, within the bulk of the fluid, the oscillation frequency matches that imposed by the body force. However, a secondary peak appears in the frequency domain, approximately at $2\Omega_f \cos\theta$, where θ is the angle between $\boldsymbol{\Omega}_f$ and the boundary normal vector $\hat{\boldsymbol{n}}$. This relationship resembles the dispersion relation for inertial waves. For an unbounded fluid rotating at $\boldsymbol{\Omega}_f$, solutions in the form of plane waves $e^{i(\boldsymbol{k}\cdot\boldsymbol{r}-\omega t)}$ exist, with the dispersion relation given by (Tilgner, 2015)

$$\omega = \pm 2\hat{\boldsymbol{k}} \cdot \boldsymbol{\Omega}_f \tag{4.27}$$

If the secondary peak observed in my simulations is indeed associated with inertial waves, this suggests that the fluid-driving scheme offers a potential opportunity to study inertial waves within the boundary layer.

Chapter 5

Conclusions

Core-mantle coupling in terrestrial planets and moons involves various mechanisms, such as pressure, viscous, and electromagnetic interactions. Our understanding of these mechanisms remains uncertain, either due to poorly constrained interior properties or to gaps in our theoretical knowledge of the processes involved. Specifically, the uncertainty related to viscous coupling is related to boundary layer **turbulence** and **roughness**, both of which have been discussed in the literature, but quantitative analysis remains scarce. To investigate these effects, we use a local Cartesian model for studying the oscillatory Ekman layer, which proves to be a valid proxy for the boundary layer of precession-driven flow. This local model enables us not only to explore the turbulent regime but also to study the effect of surface roughness on the flow.

Turbulence

The effect of boundary layer turbulence on Earth's core dynamics may be marginal. Our numerical results show that turbulent dissipation in the boundary layer of precession-driven flow, with a Reynolds number of $Re = 500$, is 1.86 times larger than the laminar prediction, corresponding to an increase in effective viscosity by a factor of 3.5 (Chapter 2). However, this increase is too small to explain the discrepancy seen in nutation observations if only turbulence is considered, as these observations require at least a two-order-of-magnitude increase in viscosity. If viscosity is considered as the only mechanism to explain the differences between the nutation theory and the observation, our result thus suggests that other mechanisms, such as electromagnetic coupling, likely play a significant role in dissipation, pointing to the presence of a strong magnetic field at the core-mantle boundary (CMB) or a highly conductive layer in the lowermost mantle. A recent study by Sikdar and Dumberry (2023) indicates that the Reynolds number at the CMB may be smaller when mantle compliance is taken into account. Their analysis, which calculates the precession of the fluid core based on an elastically deforming Earth, estimates a Reynolds number of $Re = 247$. This suggests an even smaller turbulence effect compared to the aforementioned estimate at $Re = 500$.

The critical Reynolds number for boundary layer turbulence, which we identified as approximately $Re = 290$ for the onset of turbulence in an oscillatory Ekman layer at the pole, could be influenced by other factors. Buffett (2021) demonstrated that stratification in the boundary layer may suppress turbulence, with the degree of suppression depending on the strength of the stratification. Similarly, Desjardins et al. (2001) found that the critical Reynolds number could increase by up to a factor of three when accounting for the presence of a magnetic field at the CMB. Nevertheless, given that stratification tends to dampen turbulence and the influence of electromagnetic forces appears to be marginal, our inferred critical value of $Re \approx 290$ remains a reasonable approximation for Earth.

The behavior of the boundary layer varies with latitude (or co-latitude θ). For instance, while the boundary layer becomes turbulent at most latitudes when $Re = 500$, the flow remains laminar at $\theta = 60°$ and $90°$. Caution is needed when interpreting results at $\theta = 60°$, as the Ekman layer breaks down there. The flow is not fully confined to the boundary layer but extends throughout the entire domain. At $\theta = 90°$, the flow clearly shows no signs of turbulence—though this might change with the introduction of surface roughness. What remains clear is that any inference about turbulence must account for latitudinal variations. Ignoring this can lead to overestimating or underestimating the turbulent effect, depending on the approach.

Dissipation in the lunar core has been estimated to range from 58 to 84 MW (Williams et al., 2001, 2014; Williams & Boggs, 2015). Our turbulence model predicts a turbulent dissipation of approximately 72 MW. Surface roughness can further amplify the effect of turbulence, but since our estimation—based on a smooth surface—falls within the observed range, it suggests one possibility that the effect of topography is minimal. This further implies that, from a hydraulic perspective, the core-mantle boundary of the Moon may be relatively smooth, or that the surface roughness on the scale of the boundary layer is much smaller than the boundary layer itself.

We also examine the self-consistency of the current formulation by recalculating the solution for fluid core rotation using turbulent torque under relevant conditions (Chapter 3). The original solution, based on the theory of Busse and models from previous studies, typically relies on the viscous torque that is valid in the laminar regime. By incorporating turbulent torque into the recalculation, we found that for certain parameter combinations, the solution exhibits significant changes. However, for the Earth, the Moon, and the experimental setup we discussed, the impact of turbulence on the final solution remains minimal.

Roughness

We observed that surface roughness generates pressure drag, which increases with greater roughness height (Chapter 4). This suggests that surface roughness can exert a pressure torque on fluid rotation. In the literature, pressure torque is typically discussed in the context of large-scale CMB topographies, often expressed in terms of spherical harmonics (e.g. Wu & Wahr, 1997; Puica et al., 2023). These topographies have wavelengths on the order of thousands of kilometers (around degree 20), much larger than the boundary layer thickness.

Our results show that local models can offer a useful approach for evaluating the influence of smaller-scale surface roughness on pressure drag.

Another intriguing subject is the generation mechanisms of surface roughness. In fact, there are relatively few studies that address surface roughness in detail. From a seismological perspective, the length scales involved are too small to be resolved for such deep interior structures. Two notable studies have discussed the implications of surface roughness for boundary layer dissipation (Le Mouël et al., 2006) and its correlation with gravity and magnetic fields (Mandea et al., 2015). Both studies reference the work of Narteau et al. (2001), which used a 2D cellular automata model to simulate physical processes such as dissolution, crystallization, and diffusion. In their model, element transport in the fluid is parameterized by a diffusion coefficient that represents the likelihood of an element moving between neighboring points without accounting for density gradients. The transition intensities are the same in both horizontal directions, implying that flow in the boundary layer is not explicitly modeled—at most, it is implicitly included in the diffusion coefficient.

However, studies of offshore tidal bedforms reveal that the interaction between oscillatory flow and a cohesionless material surface can generate periodic patterns on the surface (Vittori & Blondeaux, 2022). This raises the question of whether similar mechanisms occur in the boundary layer of precession-driven flow, which is also oscillatory in nature. Using our local Cartesian model, we have been able to reproduce flow patterns related to the formation of wave ripples. This offers insights into how surface roughness on the CMB might be generated and how it interacts with fluid flow.

Final words

Since nature is far too complex to simulate in its entirety, we must rely on models that approximate reality by simplifying certain aspects of the problem at hand. The local Cartesian model we employ simulates a rotating fluid in an infinite space subjected to an oscillating boundary, which leads to the formation of an oscillatory Ekman layer. We then use the calculated viscous dissipation and shear stress from this model to approximate conditions at a single point within the boundary layer of precession-driven flow. Although this approach limits our focus on the boundary layer alone, it provides a way to proceed in the parameter regime that is close to reality.

Technology is advancing at an extraordinary pace, and it is conceivable that one day a supercomputer will be capable of simulating nature with remarkable accuracy. However, we cannot predict when that will become a reality. For now, we must continue using models to approximate natural phenomena, allowing us to explore and appreciate the intricacies of the physical world.

Bibliography

Arfken, G. B., Weber, H. J., & Harris, F. E. (2011). *Mathematical methods for physicists: A comprehensive guide*. Academic press.

Blondeaux, P. (1990). Sand ripples under sea waves part 1. ripple formation. *Journal of Fluid Mechanics*, *218*, 1–17.

Bondi, H., & Lyttleton, R. (1953). On the dynamical theory of the rotation of the earth. ii. the effect of precession on the motion of the liquid core. *Mathematical Proceedings of the Cambridge Philosophical Society*, *49*, 498–515.

Bradley, J. (1747). I. a letter to the right honourable george earl of macclesfield concerning an apparent motion observed in some of the fixed stars; by james bradley ddfr s. *Philosophical Transactions of the Royal Society of London*, *45*(485), 1–41.

Braun, L., Younis, B. A., & Weigand, B. (2020). A turbulence closure study of the flow and thermal fields in the ekman layer. *Boundary-Layer Meteorology*, *175*(1), 25–55.

Breuer, D., Spohn, T., Van Hoolst, T., van Westrenen, W., Stanley, S., & Rambaux, N. (2022). Interiors of earth-like planets and satellites of the solar system. *Surveys in Geophysics*, *43*(1), 177–226.

Buffett, B. A. (1992). Constraints on magnetic energy and mantle conductivity from the forced nutations of the earth. *Journal of Geophysical Research: Solid Earth*, *97*(B13), 19581–19597.

Buffett, B. A. (2021). Conditions for turbulent ekman layers in precessionally driven flow. *Geophysical Journal International*, *226*(1), 56–65.

Buffett, B. A., & Christensen, U. R. (2007). Magnetic and viscous coupling at the core—mantle boundary: Inferences from observations of the earth's nutations. *Geophysical Journal International*, *171*(1), 145–152.

Buffett, B. A., Mathews, P. M., & Herring, T. (2002). Modeling of nutation and precession: Effects of electromagnetic coupling. *Journal of Geophysical Research: Solid Earth*, *107*(B4), ETG–5.

Busse, F. H. (1968). Steady fluid flow in a precessing spheroidal shell. *Journal of Fluid Mechanics*, *33*(4), 739–751.

Caldwell, D., Van Atta, C., & Helland, K. (1972). A laboratory study of the turbulent ekman layer. *Geophysical Fluid Dynamics*, *3*(2), 125–160.

Cébron, D. (2015). Bistable flows in precessing spheroids. *Fluid Dynamics Research*, *47*(2), 025504.

Cébron, D., Laguerre, R., Noir, J., & Schaeffer, N. (2019). Precessing spherical shells: Flows, dissipation, dynamo and the lunar core. *Geophysical Journal International*, *219*(Supplement_1), S34–S57.

Coleman, G. N. (1999). Similarity statistics from a direct numerical simulation of the neutrally stratified planetary boundary layer. *Journal of the Atmospheric Sciences*, *56*(6), 891–900.

Coleman, G. N., Ferziger, J., & Spalart, P. (1990). A numerical study of the turbulent ekman layer. *Journal of Fluid Mechanics*, *213*, 313–348.

Csanady, G. (1967). On the "resistance law" of a turbulent ekman layer. *Journal of the Atmospheric Sciences*, *24*(5), 467–471.

Dehant, V., & Mathews, P. M. (2015). *Precession, nutation and wobble of the earth*. Cambridge University Press.

Deleplace, B., & Cardin, P. (2006). Viscomagnetic torque at the core mantle boundary. *Geophysical Journal International*, *167*(2), 557–566.

Deschamps, F., Rogister, Y., & Tackley, P. J. (2018). Constraints on core–mantle boundary topography from models of thermal and thermochemical convection. *Geophysical Journal International*, *212*(1), 164–188.

Desjardins, B., Dormy, E., & Grenier, E. (2001). Instability of ekman–hartmann boundary layers, with application to the fluid flow near the core–mantle boundary. *Physics of the Earth and Planetary Interiors*, *124*(3-4), 283–294.

Deusebio, E., Brethouwer, G., Schlatter, P., & Lindborg, E. (2014). A numerical study of the unstratified and stratified ekman layer. *Journal of fluid mechanics*, *755*, 672–704.

Dumberry, M., & Mandea, M. (2022). Gravity variations and ground deformations resulting from core dynamics. *Surveys in Geophysics*, 1–35.

Ekman, M. (1993). A concise history of the theories of tides, precession-nutation and polar motion (from antiquity to 1950). *Surveys in Geophysics*, *14*(6), 585–617.

Fischer, P. F., Loth, F., Lee, S. E., Lee, S.-W., Smith, D. S., & Bassiouny, H. S. (2007). Simulation of high-reynolds number vascular flows. *Computer methods in applied mechanics and engineering*, *196*(31-32), 3049–3060.

Forte, A. M., & Peltier, W. R. (1989). Core-mantle boundary topography and whole-mantle convection. *Geophysical Research Letters*, *16*(7), 621–624.

Forte, A. M., & Peltier, W. R. (1991). Mantle convection and core-mantle boundary topography: Explanations and implications. *Tectonophysics*, *187*(1-3), 91–116.

Goldreich, P. (1967). Precession of the moon's core. *Journal of Geophysical Research*, *72*(12), 3135–3137.

Greenspan, H. P. (1968). *The theory of rotating fluids* (tech. rep.). Massachusetts Inst of Tech Cambridge Dept of Mathematics.

Greff-Lefftz, M., & Legros, H. (1995). Core-mantle coupling and polar motion. *Physics of the Earth and Planetary Interiors*, *91*(4), 273–283.

Gwinn, C. R., Herring, T. A., & Shapiro, I. I. (1986). Geodesy by radio interferometry: Studies of the forced nutations of the earth: 2. interpretation. *Journal of Geophysical Research: Solid Earth*, *91*(B5), 4755–4765.

Herring, T., Gwinn, C., & Shapiro, I. (1986). Geodesy by radio interferometry: Studies of the forced nutations of the earth: 1. data analysis. *Journal of Geophysical Research: Solid Earth*, *91*(B5), 4745–4754.

Hollerbach, R., & Kerswell, R. (1995). Oscillatory internal shear layers in rotating and precessing flows. *Journal of Fluid Mechanics*, *298*, 327–339.

Ichikawa, H., & Tsuchiya, T. (2015). Atomic transport property of fe–o liquid alloys in the earth's outer core p, t condition. *Physics of the Earth and Planetary Interiors*, *247*, 27–35.

Kadivar, M., Tormey, D., & McGranaghan, G. (2021). A review on turbulent flow over rough surfaces: Fundamentals and theories. *International Journal of Thermofluids*, *10*, 100077.

Kaneko, A., & Honji, H. (1979). Double structures of steady streaming in the oscillatory viscous flow over a wavy wall. *Journal of Fluid Mechanics*, *93*(4), 727–736.

Knittle, E., & Jeanloz, R. (1989). Simulating the core-mantle boundary: An experimental study of high-pressure reactions between silicates and liquid iron. *Geophysical Research Letters*, *16*(7), 609–612.

Koelemeijer, P. (2021). Toward consistent seismological models of the core–mantle boundary landscape. *Mantle convection and surface expressions*, 229–255.

Koot, L., Dumberry, M., Rivoldini, A., De Viron, O., & Dehant, V. (2010). Constraints on the coupling at the core–mantle and inner core boundaries inferred from nutation observations. *Geophysical Journal International*, *182*(3), 1279–1294.

Koot, L., & Dumberry, M. (2013). The role of the magnetic field morphology on the electromagnetic coupling for nutations. *Geophysical Journal International*, *195*(1), 200–210.

Kuang, W., Chao, B., & Chen, J. (2017). Decadal polar motion of the earth excited by the convective outer core from geodynamo simulations. *Journal of Geophysical Research: Solid Earth*, *122*(10), 8459–8473.

Landau, L. D., & Lifshitz, E. M. (1987). *Fluid mechanics* (Vol. 6). Pergamon Press.

Le Mouël, J.-L., Narteau, C., Greff-Lefftz, M., & Holschneider, M. (2006). Dissipation at the core-mantle boundary on a small-scale topography. *Journal of Geophysical Research: Solid Earth*, *111*(B4).

Lorenzani, S., & Tilgner, A. (2001). Fluid instabilities in precessing spheroidal cavities. *Journal of Fluid Mechanics*, *447*, 111–128.

Lums, L. I., & Aldridge, K. D. (1991). On viscosity estimates for the earth's fluid outer core and core-mantle coupling. *Journal of geomagnetism and geoelectricity*, *43*(2), 93–110.

Malkus, W. (1968). Precession of the earth as the cause of geomagnetism: Experiments lend support to the proposal that precessional torques drive the earth's dynamo. *Science*, *160*(3825), 259–264.

Mandea, M., Narteau, C., Panet, I., & Le Mouël, J.-L. (2015). Gravimetric and magnetic anomalies produced by dissolution-crystallization at the core-mantle boundary. *Journal of Geophysical Research: Solid Earth*, *120*(9), 5983–6000.

Marlatt, S., Waggy, S., & Biringen, S. (2012). Direct numerical simulation of the turbulent ekman layer: Evaluation of closure models. *Journal of the atmospheric sciences*, *69*(3), 1106–1117.

Mathews, P. M., & Guo, J. (2005). Viscoelectromagnetic coupling in precession-nutation theory. *Journal of Geophysical Research: Solid Earth*, *110*(B2).

Mathews, P. M., Herring, T. A., & Buffett, B. A. (2002). Modeling of nutation and precession: New nutation series for nonrigid earth and insights into the earth's interior. *Journal of Geophysical Research: Solid Earth*, *107*(B4), ETG–3.

Narteau, C., Le Mouël, J., Poirier, J., Sepúlveda, E., & Shnirman, M. (2001). On a small-scale roughness of the core–mantle boundary. *Earth and Planetary Science Letters*, *191*(1-2), 49–60.

Newton, I., & Chittenden, N. (1850). *Newton's principia: The mathematical principles of natural philosophy*. Geo. P. Putnam.

Nobili, C., Meunier, P., Favier, B., & Le Bars, M. (2021). Hysteresis and instabilities in a spheroid in precession near the resonance with the tilt-over mode. *Journal of Fluid Mechanics*, *909*, A17.

Noir, J., Cardin, P., Jault, D., & Masson, J.-P. (2003). Experimental evidence of non-linear resonance effects between retrograde precession and the tilt-over mode within a spheroid. *Geophysical Journal International*, *154*(2), 407–416.

Noir, J., & Cébron, D. (2013). Precession-driven flows in non-axisymmetric ellipsoids. *Journal of Fluid Mechanics*, *737*, 412–439.

Önder, A., & Yuan, J. (2019). Turbulent dynamics of sinusoidal oscillatory flow over a wavy bottom. *Journal of Fluid Mechanics*, *858*, 264–314.

Ozdemir, C. E., Hsu, T.-J., & Balachandar, S. (2014). Direct numerical simulations of transition and turbulence in smooth-walled stokes boundary layer. *Physics of Fluids*, *26*(4), 045108.

Patera, A. T. (1984). A spectral element method for fluid dynamics: Laminar flow in a channel expansion. *Journal of computational Physics*, *54*(3), 468–488.

Pizzi, F., Giesecke, A., & Stefani, F. (2021). Ekman boundary layers in a fluid filled precessing cylinder. *AIP Advances*, *11*(3), 035023.

Pozzo, M., Davies, C., Gubbins, D., & Alfe, D. (2013). Transport properties for liquid silicon-oxygen-iron mixtures at earth's core conditions. *Physical Review B*, *87*(1), 014110.

Puica, M., Dehant, V., Folgueira, M., Van Hoolst, T., & Rekier, J. (2023). Analytical computation of total topographic torque at the core–mantle boundary and its impact on tidally driven length-of-day variations. *Geophysical Journal International*, *234*(1), 585–596.

Rekier, J., Triana, S. A., Trinh, A., & Dehant, V. (2020). Inertial modes of a freely rotating ellipsoidal planet and their relation to nutations. *The Planetary Science Journal*, *1*(1), 20.

Roberts, P. H., & Aurnou, J. M. (2012). On the theory of core-mantle coupling. *Geophysical & Astrophysical Fluid Dynamics*, *106*(2), 157–230.

Rochester, M. (1962). Geomagnetic core-mantle coupling. *Journal of Geophysical Research*, *67*(12), 4833–4836.

Sasao, T., Okubo, S., & Saito, M. (1980). A simple theory on the dynamical effects of a stratified fluid core upon nutational motion of the earth. *Symposium-International Astronomical Union*, *78*, 165–183.

Shih, S.-A., Triana, S. A., Rekier, J., & Dehant, V. (2023). Turbulent dissipation in the boundary layer of precession-driven flow in a sphere. *AIP Advances*, *13*(7).

Shingai, K., & Kawamura, H. (2004). A study of turbulence structure and large-scale motion in the ekman layer through direct numerical simulations. *Journal of Turbulence*, *5*(1), 013.

Sikdar, B., & Dumberry, M. (2023). The differential precession of earth's fluid and solid cores. *Physics of the Earth and Planetary Interiors*, *339*, 107022.

Sleath, J. F. (1976). On rolling-grain ripples. *Journal of Hydraulic Research*, *14*(1), 69–81.

Sleath, J. F. (1987). Turbulent oscillatory flow over rough beds. *Journal of Fluid Mechanics*, *182*, 369–409.

Soldati, G., Boschi, L., & Forte, A. M. (2012). Tomography of core–mantle boundary and lowermost mantle coupled by geodynamics. *Geophysical Journal International*, *189*(2), 730–746.

Sous, D., Sommeria, J., & Boyer, D. (2013). Friction law and turbulent properties in a laboratory ekman boundary layer. *Physics of Fluids*, *25*(4), 046602.

Spalart, P. R. (1989). Theoretical and numerical study of a three-dimensional turbulent boundary layer. *Journal of Fluid Mechanics*, *205*, 319–340.

Stacey, F. D., & Davis, P. M. (2008). *Physics of the earth*. Cambridge University Press.

Stys, C., & Dumberry, M. (2020). A past lunar dynamo thermally driven by the precession of its inner core. *Journal of Geophysical Research: Planets*, *125*(7), e2020JE006396.

Tennekes, H., Lumley, J. L., Lumley, J. L., et al. (1972). *A first course in turbulence*. MIT press.

Thornton, S. T., & Marion, J. B. (2003). *Classical dynamics of particles and systems*. Cengage Learning.

Tilgner, A. (2015). Rotational dynamics of the core. In G. Schubert (Ed.), *Treatise on geophysics* (pp. 183–212). Elsevier.

Toomer, G. (1996). Ptolemy and his greek predecessors. *Astronomy before the Telescope*, 68–91.

Triana, S. A., Trinh, A., Rekier, J., Zhu, P., & Dehant, V. (2021). The viscous and ohmic damping of the earth's free core nutation. *Journal of Geophysical Research: Solid Earth*, *126*(4), e2020JB021042.

Vanyo, J., Wilde, P., Cardin, P., & Olson, P. (1995). Experiments on precessing flows in the earth's liquid core. *Geophysical Journal International*, *121*(1), 136–142.

Vincze, M., Fenyvesi, N., Klein, M., Sommeria, J., Viboud, S., & Ashkenazy, Y. (2019). Evidence for wind-induced ekman layer resonance based on rotating tank experiments. *EPL (Europhysics Letters)*, *125*(4), 44001.

Viswanathan, V., Rambaux, N., Fienga, A., Laskar, J., & Gastineau, M. (2019). Observational constraint on the radius and oblateness of the lunar core-mantle boundary. *Geophysical Research Letters*, *46*(13), 7295–7303.

Vittori, G., & Blondeaux, P. (2022). Predicting offshore tidal bedforms using stability methods. *Earth-Science Reviews*, *235*, 104234.

Wahr, J. M. (1981). The forced nutations of an elliptical, rotating, elastic and oceanless earth. *Geophysical Journal International*, *64*(3), 705–727.

Williams, J. G., & Boggs, D. H. (2015). Tides on the moon: Theory and determination of dissipation. *Journal of Geophysical Research: Planets*, *120*(4), 689–724.

Williams, J. G., Boggs, D. H., Yoder, C. F., Ratcliff, J. T., & Dickey, J. O. (2001). Lunar rotational dissipation in solid body and molten core. *Journal of Geophysical Research: Planets*, *106*(E11), 27933–27968.

Williams, J. G., Konopliv, A. S., Boggs, D. H., Park, R. S., Yuan, D.-N., Lemoine, F. G., Goossens, S., Mazarico, E., Nimmo, F., Weber, R. C., et al. (2014). Lunar interior properties from the grail mission. *Journal of Geophysical Research: Planets*, *119*(7), 1546–1578.

Wu, X., & Wahr, J. M. (1997). Effects of non-hydrostatic core-mantle boundary topography and core dynamics on earth rotation. *Geophysical Journal International*, *128*(1), 18–42.

Yoder, C. F. (1981). The free librations of a dissipative moon. *Philosophical Transactions of the Royal Society of London. Series A, Mathematical and Physical Sciences*, *303*(1477), 327–338.

Zhang, J., & Dumberry, M. (2021). Viscous dissipation in the fluid core of the moon. *Journal of Geophysical Research: Planets*, *126*(11), e2021JE006966.